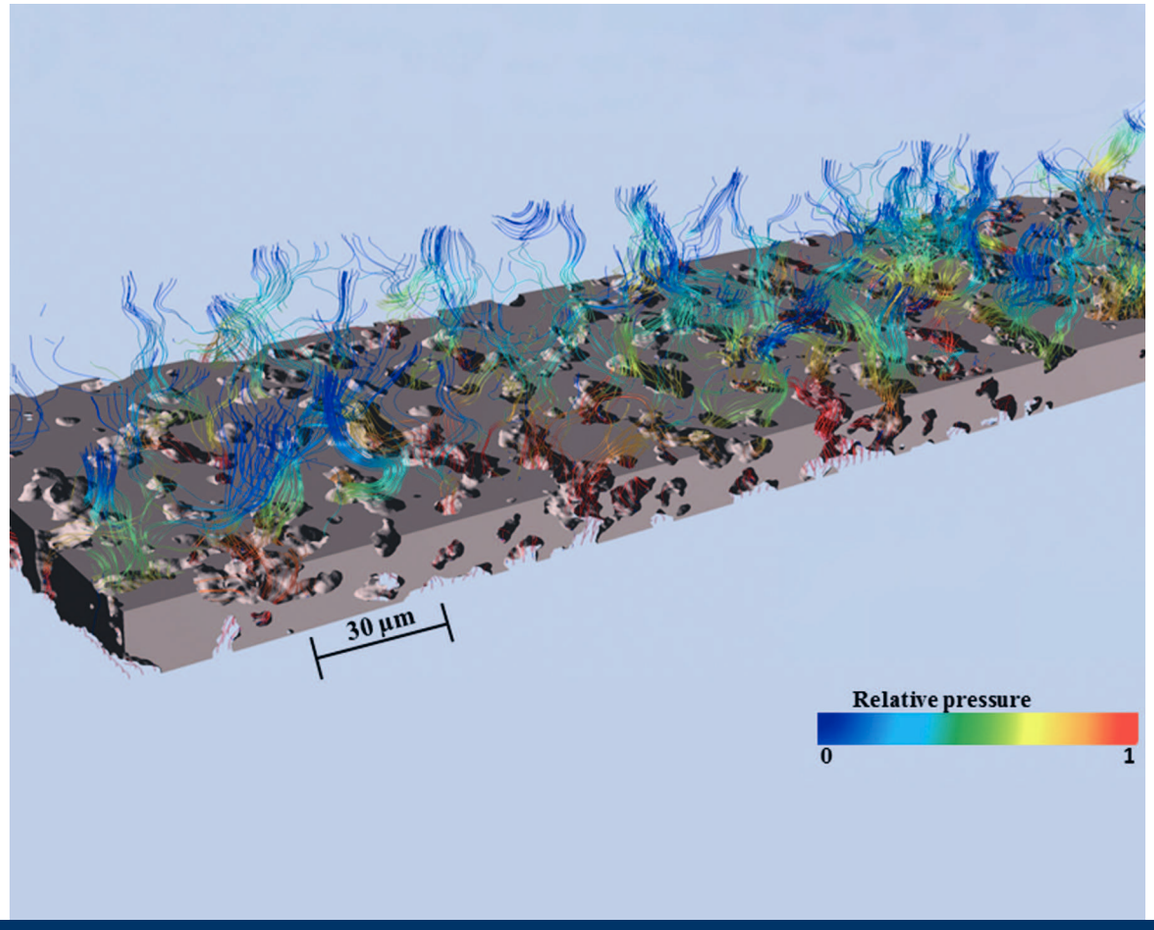

Simulation of Transport Processes through an Asymmetric Gas Separation Membrane

Unoaku Victoria Unije

Energie & Umwelt / Energy & Environment
Band / Volume 463
ISBN 978-3-95806-403-4

Mitglied der Helmholtz-Gemeinschaft

JÜLICH
Forschungszentrum

Schriften des Forschungszentrums Jülich
Reihe Energie & Umwelt / Energy & Environment Band / Volume 463

Forschungszentrum Jülich GmbH
Institut für Energie- und Klimaforschung
Werkstoffsynthese und Herstellungsverfahren (IEK-1)

Simulation of Transport Processes through an Asymmetric Gas Separation Membrane

Unoaku Victoria Unije

Schriften des Forschungszentrums Jülich
Reihe Energie & Umwelt / Energy & Environment Band / Volume 463

ISSN 1866-1793 ISBN 978-3-95806-403-4

Bibliografische Information der Deutschen Nationalbibliothek.
Die Deutsche Nationalbibliothek verzeichnet diese Publikation in der Deutschen Nationalbibliografie; detaillierte Bibliografische Daten sind im Internet über http://dnb.d-nb.de abrufbar.

Herausgeber und Vertrieb: Forschungszentrum Jülich GmbH
Zentralbibliothek, Verlag
52425 Jülich
Tel.: +49 2461 61-5368
Fax: +49 2461 61-6103
zb-publikation@fz-juelich.de
www.fz-juelich.de/zb

Umschlaggestaltung: Grafische Medien, Forschungszentrum Jülich GmbH

Druck: Grafische Medien, Forschungszentrum Jülich GmbH

Schriften des Forschungszentrums Jülich
Reihe Energie & Umwelt / Energy & Environment, Band / Volume 463

D 82 (Diss., RWTH Aachen University, 2019)

ISSN 1866-1793
ISBN 978-3-95806-403-4

Vollständig frei verfügbar über das Publikationsportal des Forschungszentrums Jülich (JuSER) unter www.fz-juelich.de/zb/openaccess.

Abstract

Oxygen gas separation membranes with mixed ionic and electronic conductivity (MIEC) have found great prospects in membrane technology for oxygen separation from gas mixtures (e.g. air) under a partial pressure gradient as the driving force. The separation of oxygen using membranes is more energy efficient than traditional processes such as the cryogenic Linde process or pressure swing adsorption (PSA). The inverse relationship between the membrane thickness and flux underscores the need for a very thin membrane. Consequently, the low mechanical stability of free-standing thin membranes motivated the processing of asymmetric membranes, where the thin membranes are supported by a porous structure. Asymmetric membranes provide a low ionic resistance of the functional separation layer together with a high mechanical stability. However, the microstructure of the porous support in the membrane assembly affects the overall flux significantly. Therefore, a porous support that provides the required mechanical stability needed for the dense membrane, with little or no limiting effect on the overall flux is desired.

The gas flow through porous media including that of multiple species is often described by the Binary Friction Model (BFM) considering the binary diffusion, Knudsen diffusion, and viscous flow. Therefore, the transport through an asymmetric membrane was studied by applying the BFM for the support together with a modified Wagner equation for the dense membrane in one dimension. In addition, transport relevant parameters obtained from micro computed tomography data of asymmetric membranes manufactured from different processing routes were used. The effects of the geometrical parameters of the support's microstructures on the overall flux through an asymmetric membrane were compared for different feed gases (oxygen and air) and flow configurations (3-end and 4-end mode, assembly orientations). The rate-limiting effect of the support with large pore diameters (> 35µm) for the 3-end mode transport process using oxygen as feed gas was less than 10% with respect to the flux of the isolated thin membrane. This was not the case for the 4-end mode irrespective of the feed gas, and for the 3-end mode with the support at the feed side using air as feed gas. This was attributed to the binary diffusion term in the BFM which is not affected by the change in pore size. Thin small-pored supports yield the same flux as thick large-pored supports considering a non-linear relationship between thickness and pore size. This can be used for the optimization of the support's microstructure with regards to mechanical strength and permeability. Elongated pores in the flow direction will be ideal for membrane reactors because of the mixed gas transport in the porous supports, whereas single gas transport through the porous support is significantly less influenced by the tortuosity. Computational fluid dynamics simulations were used to investigate the effect of pore geometry on viscous flow. The pore morphology (size, shape and orientation) and not just the pore opening diameter affects the in-pore velocity. Furthermore, a two-layer support system was designed for the optimization of the porous support with respect to mechanical strength and permeability. Comparable fluxes were obtained for the two-layer support system with respect to 90% membrane performance for single support layer system.

Finally, two simplifications of the pressure profiles within the porous support (constant pressure according to the pressure at the free surface and the average at the surface and the interface) were compared to the exact numerical solution of the BFM, given that the exact numeri-

cal solution of the binary friction model is complicated and requires high computational efforts (most especially for implementations in three dimensional simulations). The simplification using a constant pressure equal to the gas pressure outside the support deviated from the exact solution under certain operating condition is ~ 3 times more than the average constant pressure simplification. The average constant configuration using still a constant pressure averaged between the outside of the support and the support/membrane interface had no significant deviation with the exact solution. Therefore, this is a useful measure to reduce computational efforts when implementing the Binary Friction Model in computational fluid dynamics simulation.

Kurzfassung

Mischleitende Sauerstoffgastrennmembrane weisen ein großes Potential in der Anwendung der Sauerstoffabtrennung aus Gasgemischen wie Luft auf, weil die Abscheidung von Gasen mittels Membranen energieeffizienter als herkömmliche Verfahren wie das kryogene Linde-Verfahren oder die Druckwechseladsorption (PSA) ist. Die reziproke Beziehung zwischen Membrandicke und resultierendem Fluss unterstreicht die Notwendigkeit einer sehr dünnen Membran. Die geringe mechanische Stabilität von freistehenden dünnen Membranen führte zur Entwicklung von asymmetrischen Membranen bei welchen die dünnen Membranen von einer porösen Struktur getragen werden, um so gleichzeitig einen geringen Ionenwiderstand der funktionellen Trennschicht als auch eine hohe mechanische Stabilität zu erreichen. Die Mikrostruktur des porösen Trägers in der Membran Anordnung beeinflusst jedoch den Gesamtfluss signifikant. Daher ist ein poröser Träger erwünscht, der neben der erforderlichen mechanischen Stabilität einen möglichst geringe Strömungswiderstand aufweist.

Die Gasströmung einschließlich derjenigen von mehreren Spezies, durch poröse Medien, wird häufig durch das *Binary Friction Model* (BFM) beschrieben, das die binäre Diffusion, die Knudsen-Diffusion und die viskose Strömung berücksichtigt. Daher wurde der Transport durch eine asymmetrische Membran untersucht, in dem das eindimensionale BFM für den Träger zusammen mit einer modifizierten Wagner-Gleichung für die dichte Membran angewendet wurde. Die transportbestimmenden Parameter (Permeanz, Tortuosität, Porengröße) für das poröse Substrat wurden mit Hilfe von Simulationsrechnungen aus Mikro-Computer-Tomographie-Daten ermittelt. Die Einflüsse der geometrischen Parameter des Trägergefüges wurden für verschiedene Einsatzgase (Sauerstoff und Luft) und Strömungskonfigurationen (3-End, 4-End, Einbaurichtung) verglichen. Bei großen Substratporen (> 35 µm) konnte für den 3-End-Modus unter Verwendung von O_2 als Einsatzgas ein Gesamtfluss von mehr als 90% bezogen auf die isolierte Membranschicht erreicht werden. Dies war nicht der Fall für den 4-End-Modus unabhängig von dem Speisegas und für den 3-End-Modus mit Luft als Speisegas. Genau bei diesen Modi tritt im Substrat eine binäre Diffusion auf, die durch die Veränderung der Porengröße nicht beeinflusst wird. Dünne kleinporige Träger ergeben den gleichen Fluss wie dicke großporige Träger unter Berücksichtigung einer nichtlinearen Beziehung zwischen Dicke und Porengröße. Dies kann zur Optimierung der Mikrostruktur des Trägers in Bezug auf mechanische Festigkeit und Permeabilität verwendet werden. Langgestreckte Poren in Strömungsrichtung sind aufgrund des Mischgastransports in den porösen Trägern ideal für Membranreaktoren (4-End), während für der Gastransport eines reinen Gases (3-End) durch den porösen Träger nur geringfügig von der Tortuosität beeinflusst wird. *Computational Fluid Dynamics*-Simulationen wurden verwendet, um den Effekt der Porengeometrie auf die viskose Strömung in Bezug auf den Transport-Prozess zu untersuchen. Aufbauend auf den Ergebnissen einlagiger Träger wurde ein doppellagiges, gradiertes Trägersystem konzipiert, welches eine hohe Permeabilität bei einer gleichzeitig ausreichenden Substratdicken aufweist.

Abschließend wurden zwei Vereinfachungen der Druckprofile innerhalb des porösen Trägers (konstanter O_2-Partialdruck entsprechend des Drucks an der freien Oberfläche und des Mittelwerts an der Oberfläche und Grenzfläche) mit der genauen numerischen Lösung des BFM ver-

glichen, angesichts der Tatsache, dass die exakte numerische Lösung des BFM kompliziert ist und einen hohen Rechenaufwand erfordert (insbesondere für Implementierungen in dreidimensionalen Simulationen). Die Vereinfachung unter Verwendung eines konstanten Partialdrucks gleich dem Druck an der freien Oberfläche des Trägers, der von der exakten Lösung unter bestimmten Betriebsbedingungen abweicht, ist ~3-mal mehr als die durchschnittliche konstante Druckvereinfachung. Die Vereinfachung unter Verwendung eines immer noch konstanten Partialdrucks, der zwischen der Außenseite des Trägers und der Träger / Membran-Grenzfläche gemittelt wurde, wies keine signifikante Abweichung von der exakten Lösung auf. Daher ist dies eine nützliche Maßnahme, um den Rechenaufwand bei der Implementierung des binären Reibungsmodells in der numerischen Strömungssimulation zu reduzieren.

Table of content

Table of content

Nomenclature

Symbols

A = Cross-sectional area
B_o = Permeability (m^2)
C = total molar density
C_i = Molar density of species *i*
c_o / c_v = Concentration of oxygen anions / vacancy
d = Pore diameter (µm)
j_{O_2} = Oxygen flux (mol/s m^2)
D_{AB} = Binary diffusion coefficient (cm^2/s)
D_V = Diffusion coefficient of oxygen vacancies (cm^2/s)
D_g^K = Knudsen diffusion
F_i = External body force
j = Flux (mol/s m^2)
j_{ex}^0 = Surface exchange rate (mol O_2 $cm^{-2}s^{-1}$)
j_s = Entropy flux relative to mass average velocity
k_o = Surface exchange coefficient (cm s^{-1})
k_f = Forward reaction
k_r = Reverse reaction
k_s = Surface exchange coefficient
L_A = Thick layer substrate (Layer A)
L_B = Thin layer substrate (Layer B)
L = Length (m)
L_c = Characteristic thickness (m)
M = Molecular weight of species *i* (mol O_2 $cm^{-2}s^{-1}$)
L_e = Pore length (m)
N_i = Flux (mol/s m^2)
p_{O_2} = Partial pressure of oxygen (mbar)
P_t = Total pressure (mbar)
P_i = Partial pressure of species *i* (mbar)
Q = Flow rate (m^3/s)
r_{im} = Friction term
$\hat{S}$ = Entropy per unit mass
T = Temperature in °C or K
t_i = Transference number of charged species *i* (*i* = electrons, or ions)
u_i = Velocity of diffusion of species *i*
x_i = Mole fraction of specie *i*.
z_k = Charge number

Nomenclature

Greek symbols

ε = Porosity
η = viscosity (Kg/m s)
κ = Tortuosity factor
v = mass average mixture velocity
σ = Volumetric rate of entropy production
σ_{amb} = Ambipolar conductivity (S/m)
σ_{el} = Electronic conductivity (S/m)
σ_{ion} = Ionic conductivity (S/m)
σ_k = Conductivity of charge carriers (S/m)
ζ = Interaction parameter
τ = Tortuosity
μ_k = Electrochemical potential of charge carriers (J/mol)
σ_k = Conductivity of charge carriers (S/m)
ϕ_k = Electronic potential (volt)
λ = Molecular mean free path
ω_i = Volume fraction of species *i*
$\nabla_{T,p}\ \mu_i$ = Isothermal-isobaric gradient of the molar chemical potential

Constants

R	= Gas constant (J /K mol)	8.3144598
F	= Faraday's constant (C/mol)	96 485.3329
K_b	= Boltzmann constant (J/K)	$1.38064852 \times 10^{-23}$

Abbreviations

MIEC	= Mixed ionic and electronic conducting membrane
OTM	= Oxygen transport membrane
BFM	= Binary Friction Model
μCT	= Micro computed tomography
CFD	= Computational fluid dynamic
SF	= Support on the feed side
SP	= Support on the permeate side
PSA	= Pressure swing adsorption
BSCF	= $Ba_{0.5}Sr_{0.5}Co_{0.8}Fe_{0.2}O_{3-\delta}$
BSCF3Zr	= $Ba_{0.5}Sr_{0.5}(Co_{0.8}Fe_{0.2})_{0.97}Zr_{0.03}O_{3-\delta}$
TC	= Tape cast
FC	= Freeze cast

List of Figures

List of Figures

List of Figures

List of Tables

1. Introduction

1.1 Overview

Dense ceramic oxygen transport membranes (OTM) have found great prospects in membrane technology for the supply of oxygen through air separation [1-4]. OTM have been developed and tested for the production of ultra clean fuels [5] and they also offer high potential for oxy-combustion and syngas applications [6]. They are also considered to be key components for low-pollutant combustion power plants, energy efficient oxygen generators, the synthesis of higher hydrocarbons [7, 8], novel types of membrane reactors [9, 10], in health care, and in various industrial sectors (such as steel, iron, cement, and glass plants).

The separation of oxygen from air using membranes is more energy efficient than traditional processes such as the cryogenic Linde process and, the pressure swing adsorption (PSA) [11, 12]. Perovskites with the chemical formula $ABO_{3-\delta}$ are widely used for manufacturing oxygen transport membranes. These perovskites, in particular $Ba_{0.5}Sr_{0.5}Co_{0.8}Fe_{0.2}O_{3-\delta}$ (BSCF) which was first reported by Shao *et al*. [13] exhibit high oxygen permeability at elevated temperatures [14, 15]. This high permeability originates from a pronounced mixed ionic and electronic conductivity (MIEC) [13, 16], which is attributed to the crystal lattice arrangement of the perovskite structure. These MIEC membranes allow only the permeation of oxygen, and a perm-selectivity of 100% can be achieved if the membrane is gas tight [17].

Over the years, research studies have investigated ways to improve the overall flux through the dense membrane. Studies have found that the thinner the MIEC membranes are the higher the flux becomes, but this reduces their mechanical stability owing to the application of these membranes. This motivated the state-of-the-art processing of an asymmetric membrane (the thin dense membrane supported by a porous structure) that provide a low ionic resistance of the functional separation layer together with a high mechanical stability.

Notwithstanding, the flux observed from asymmetric membranes is not commensurate to the expected flux with regards to the thickness of the thin dense membrane considering the Wagner equation [16-19]. The Wagner equation which is a solid-state diffusion equation shows that the flux has an inverse relationship with the dense membrane thickness. As a result, the oxygen flux through thin supported membranes is expected to increase with respect to the thickness of the dense membrane. Research studies have found that the porous support does not only provide the mechanical stability needed, but it affects the overall observed flux [20, 21]. Li *et al.* [20] showed through permeation experiment for both H_2 and CO_2 that the flux observed for thin supported membranes when compared to thick dense membranes was not as high as expected. Owing to the fact that an inadequate support microstructure becomes rate limiting for the gas transfer, further improvements are needed. Lately, the optimization of this sort of asymmetric microstructures have been under investigations by using novel fabrication methods like freeze-casting [22-27] and phase inverse casting [28, 29]. Using different mem-

brane materials, these asymmetric membranes have demonstrated an improvement on permeation rate [14, 30, 31], as the porosity, the tortuosity factor, pore opening diameter and the morphology of the pores are tailored and controlled based on the processing route. The architectures resulting from these fabrication routes offer various advantages like improving flux, reducing concentration polarization, etc., when compared to bulk membranes.

During permeation through an asymmetric membrane, different sets of very complex transport mechanisms are encountered. Each of which are possibly rate limiting and can be interpreted as a series of resistances for the transport. This comprises the gas phase diffusion, surface exchange reaction, bulk diffusion, and concentration polarization within the pores and in the gas phase. Each of these individual mechanisms has been investigated and studied. Combination of all these mechanisms in a single model for simulating the overall transport through an asymmetric membrane is needed. The need to understand to what extent the geometrical parameters of the support microstructure would be rate limiting and ways to optimize it motivated this work.

1.2 Objectives of this work

In this work, the simulation of the transport processes through an asymmetric gas (Oxygen) separation membrane is to be considered. According to research studies, the porous support significantly hinders the overall flux through an asymmetric membrane. As a result, it is essential to understand and simulate the extent or the support limitations on flux. The membrane-support interface pressure cannot be measured from permeation measurements. Therefore, there is a need to evaluate the membrane support interface pressure and the dependence of this pressure on the support microstructure with respect to observed flux. In addition, the simulation of the effect of the support geometry on the overall flux through an asymmetric membrane should show how much the porous support is rate limiting and will further aid the optimization of the porous support.

For these investigations, a one-dimensional analytical model combining the Wagner equation and the binary friction model was used for the description of the transport through the dense membrane and the porous support, respectively. The effect of the porous support geometry on flux taking into consideration the different transport modes (the 4-end mode and the 3-end mode) and the orientations of the asymmetric membrane encountered in application were evaluated. In addition, different simplification of the partial pressure profiles through the support of an asymmetric membrane using the binary friction model according to Kerkhoff [32] would be used to investigate the pressure effect.

Comparison of the obtained simulated results to experimental observation would validate the model and the process steps employed. Finally, the question of how to manufacture a porous support for an asymmetric membrane which offers the mechanical stability needed but with little or no limitations on the observed flux will be answered.

2. Fundamentals and state of the art

2.1 Inorganic Oxygen transport membranes

Inorganic gas separation membranes can be simply described as a discrete interface or a barrier which differentially allows or moderates the permeation of certain constituent of a gas mixture through it (Figure 2.1).

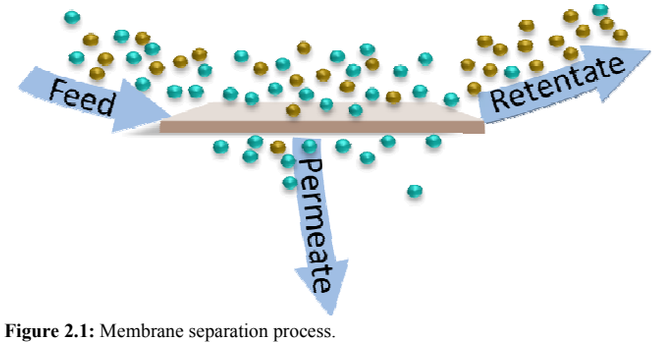

Figure 2.1: Membrane separation process.

The use of these membranes for separation process is a dynamic and rapidly growing field and would be advantageous with respect to low energy use and capital investments. They can be used for O_2 separation, H_2 separation and CO_2 separation. Inorganic gas separation membranes are considered key components for chemical reactors as well as low emission power plants with high efficiency.

Oxygen is one of the most widely used chemicals in the world [17]. In industry it has found application in manufacturing industry, food industry, chemical industry, combustion processes of higher hydrocarbon, etc. It is also used in health care for patients with chronic lung disease or who cannot breathe on their own. Yearly, several million tons of oxygen are produced [33], and may increase over the years with the advancement of large-scale clean energy technologies [34]. These technologies will require pure oxygen as feed gas for combustion in order to combat e.g. NO_x emissions. In the recent past, the production of oxygen is mainly realized by conventional techniques; cryogenic distillation of air and pressure swing adsorption (PSA) [9, 12]. As a result of the high cost and high energy demands of these conventional techniques, development of an energy efficient oxygen production technology is of great economical interest. The separation of oxygen from air using inorganic (ceramic) gas separation membranes for oxygen production offer substantial advantages to the conventional techniques. As the sectors where combustion is the primary source for heat are major contributors of greenhouse gas emission [35], ceramic oxygen transport membranes are planned to be employed to reduce the emissions.

2.1. Inorganic Oxygen transport membranes

In pre-combustion process, the oxygen transport membrane (OTM) is to be used to separate oxygen from air, to produce pure oxygen for the partial oxidation of the fossil fuel to syngas (a mixture of H_2 and CO). Adding steam to the mixture in a shift reactor, a water-gas-shift reaction occurs. This generates H_2 and CO_2, and the hydrogen is either combusted to produce power or used for different application, while the CO_2 is collected for further utilization [36] or stored. Similarly, production of NO_x in oxy-fuel combustion process can be prevented because pure oxygen generated from oxygen transport membranes is used for combusting the fuel. As a result, the flue gas produced contains mainly a mixture of CO_2 and steam which can be easily separated by a condensation process. As a result, production of NO_x can be prevented. The generation of oxygen or hydrogen, might not only be generated only from simple gas mixtures such as air or syngas, but also from the decomposition of industrial waste (CO_2, H_2O, NO_x, H_2S, etc. [37]) stream from gasification plants. Studies [36-39] have shown that ion (O-, H-) conducting inorganic gas separation membranes can be used in membrane reactors [7, 40, 41] for the synthesis of various chemicals [41].

Oxygen transport membranes have been widely investigated for integration into membrane reactors [35, 42-55] for reforming and partial oxidation of hydrocarbons to produce syngas and also the utilization of CO_2. In addition, waste heat from combustion processes will be used in these reactors and it also improves efficiency as well as sustainability. The synthesis of useful products from these gases that are in some cases hazardous is more valuable and stirs the chemical industry in a sustainable direction.

2.1.1 Ceramic membrane material

Much effort is being exerted to understand the phenomena involved during gas transport through membranes as well as to synthesize novel materials with better separation properties. Although the concept of permeating oxygen using mixed ionic-electronic conductor was introduced by Cales and Baumard [56], the current industrial interest in membrane separators was proposed by Teraoka *et al.* [57]. They observed an oxygen flux of 3.2 mL/cm² min on the investigated 1mm thick perovskite type oxide ($SrCo_{0.8}Fe_{0.2}O_{3-\delta}$) at a temperature of 850°C. There has been a rapid growth of both scientific and industrial interest in the use of these membranes for the separation of oxygen since then.

2.1.1.1 Requirements of ceramic OTM membrane material

The core requirements of a good ceramic membrane for the transport of both ions and electrons are as schematically shown in Figure 2.2 They should be stable at high operating temperatures, easy to clean and easy to be catalytically activated. In addition, it should be able to resist harsh environments and high pressure drops during operation compared to organic membranes. However, not all OTM have the ability to resist harsh operating environments.

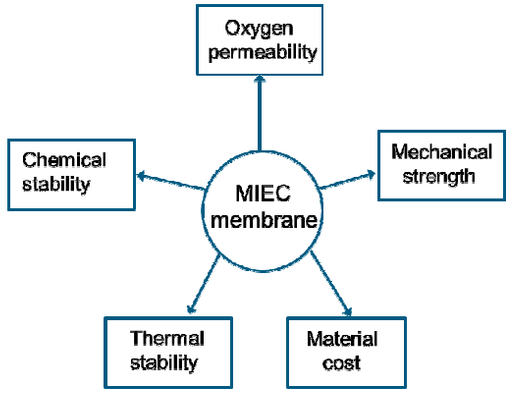

Figure 2.2: Showing the core requirements of a good MIEC membrane for oxygen transport.

Notwithstanding their enormous advantages, they are limited as a result of their brittle nature, high capital cost, and in some cases do not always have good chemical stability. Fluorite or perovskite type material, pyrochlore, brownmillerite, Ruddlesden-Popper series [58-64] are some materials that have been found promising for manufacturing OTM. Compound exhibiting fluorite and perovskite type crystal are best in terms of oxygen permeation, but the perovskites are most attractive because they exhibit higher oxygen permeability at elevated temperatures.

2.1.1.2 Perovskites

Perovskites is the name of structural family described by the general formula ABO_3 shown schematically in Figure 2.3 as well as the name of a mineral compounds that occur naturally with the chemical formula $CaTiO_3$ [65].

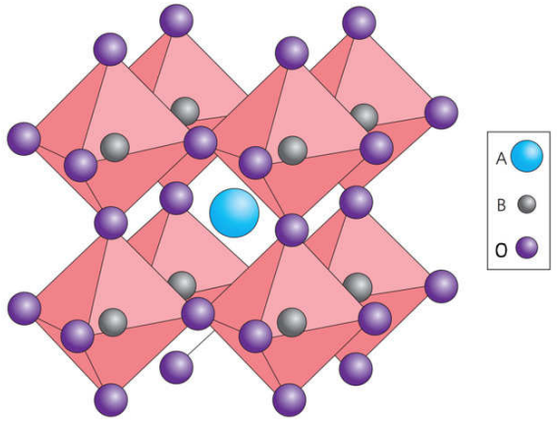

Figure 2.3: The perovskite structure ABO_3 [61]

The chemical compound ($CaTiO_3$) in its natural state have been synthesized for the manufacturing of oxygen transport membrane [66] and it also finds application as electronic or optical material [66]. However, the ideal perovskite is not typified by $CaTiO_3$ rather by $SrTiO_3$ which is a cubic closed packed structure [65]. The arrangement of atoms within the perovskite crystal structure has found great prospects in membrane technology for the production of OTM. The perovskite type compounds are crystalline ceramics with different symmetry at room temperature, but can transform to cubic [17] symmetry at high temperatures [67, 68].

The A and B are cations with different sizes occupying the cube corners and body centered positions respectively, and the oxygen (an anion bonding A and B) occupying the face centered position. The A and B sites are occupied by an alkaline earth ion or rare earth ion and a transition metal cation, respectively. The A-site ion exits at the interstitial of the BO_6 octahedral. Therefore, because A cations are generally larger than the B cations, it distorts the BO_6 octahedral. With respect to the geometric considerations, the Goldschmidt tolerance factor, *t*, [17, 69] is used to define the tolerance limit of the cationic radii in the A and B sites according to Eq. 2.1

$$t = \frac{r_A + r_B}{\sqrt{2}\left(r_B + r_O\right)} \tag{2.1}$$

where r_A, r_B, and r_O are the radii of the A, B cations, and the oxygen ion, respectively. The perovskite structure is stable for a tolerance factor in the range of 0.75 – 1.0. An ideal perovskite lattice exists when *t* is close to one and becomes distorted to less symmetric structures as the magnitude of *t* decreases.

Doping the A and B sites with multivalent cations can lead to the occurrence of a material or a compound with mixed ionic and electronic conductivity property [13, 21, 52, 57, 70]. Depending on the atoms doped at the A and B site, the properties like conductivity, magnetism, and thermal expansion of the material are significantly influenced [17]. For example, transition metal with multiple oxidation states tend to take a lower oxidation state, thereby effectively freeing up electrons to pass current when doped at the A and B sites. Furthermore, doping some of the B site (transition metal) with an aliovalent transition metal will also yield an increase in electronic conductivity. Aliovalency simply means when the oxidation states of the dopant in the lattice differs from the cation ion. Also increasing the intrinsic oxygen vacancy concentration during doping will increase the available hopping sites, thereby increasing the ionic conductivity [31, 71]. Oxygen vacancies in the crystal lattice of perovskite type OTM facilitate the oxygen transport. As such, the rate of vacancy diffusion within the membrane and the interfacial oxygen exchange on either side of the membrane control the flux. Several materials belonging to the perovskite class; $(X,Y)MO_3$ (X = rare earth, Y = Ca, Sr, Ba, M = Fe, Co, Cu, Zn) have been shown to provide fast oxygen transport [12, 17, 58-60, 62, 64].

2.1.2 Dense Mixed Ionic and Electronic Conducting membranes

Dense ceramic OTM comprises different metal oxides that are not stoichiometric at room or at elevated temperature and some unoccupied oxygen sites (vacancies) in its crystal structure.

The material composition, initial lattice structure, ambient gas composition and temperature affect the number of oxygen vacancies. With sufficient thermal energy to overcome the energy barrier, the lattice oxygen around these vacancies can hop randomly from their original site to these vacancies. These hops of oxygen ions can have a statistical direction under a partial pressure gradient of oxygen across the membrane (driving force) from the high P_{O_2} (feed side) to the low P_{O_2} side (permeate side), respectively. The oxygen ions and electrons flow counter current to each other through the membrane.

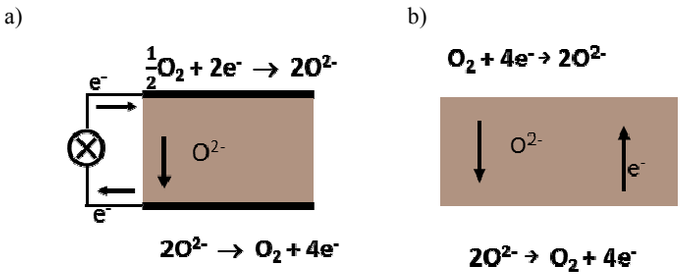

Figure 2.4: The transport mechanism for (a) the pure ionic and (b) MIEC oxygen transport membrane.

There are pure ionic OTMs (Figure 2.4.a) and mixed ionic and electronic conducting OTMs (Figure 2.4.b). The pure ion conducting membranes as the name goes, allow on the transport of oxygen ion. To maintain charge neutrality in a pure ion conducting membrane, a counter-transport of electronic charge carrier is necessary and has to be introduced by applying an external circuit. This is not the case for mixed ionic and electronic conducting (MIEC) oxygen transport membranes.

The MIEC membranes have a simpler design and reduced energy requirements in comparison to the pure ion conducting membranes. These membranes exhibiting mixed oxygen ionic and electronic conductivity [34] provide a new way for oxygen production. Across the MIEC OTM, there is relatively fast and sustainable transport of oxygen ions and electron holes under appropriate operating conditions, resulting in oxygen conduction [3, 64, 72-74]. This is as a result of their ability to support oxygen vacancies and lattice disorder. Studies have shown that the flux of oxygen through the membrane is dominated by the membrane material composition, the operating temperature, and oxygen gradient [12, 57, 75-77].

2.1.3 Transport mechanism in dense membrane

The transport mechanism of oxygen through MIEC OTM and the corresponding resistances is as depicted in Figure 2.5. At the zone 1, the oxygen molecule is transported from the gas phase to the membrane surface by gas to gas diffusion. The transported oxygen molecule adsorbs to the membrane surface (zone 2) and dissociates into two oxygen ions by receiving electrons from the membrane surface according to the equation on the top side of Figure 2.4.b, and is incorporated in the crystal lattice. At this membrane surface, the oxygen partial pressure is high-

er than it is at the membrane surface at zone 4. The oxygen ion transport (bulk diffusion) occurs in the zone 3. After the incorporation of oxygen ions in the crystal lattice of the surface layer, the oxygen ion diffuses across the membrane under an oxygen partial pressure as the driving force through the oxygen vacancies in the crystal lattice. The transported oxygen ion recombines on the membrane surface (zone 4) with the lower oxygen partial pressure to form molecular oxygen. This recombination is as shown at the bottom side equation of Figure 2.4.b. Finally, the recombined oxygen molecule desorbs from the membrane surface into the gas phase (zone 5) and is transported by gas diffusion.

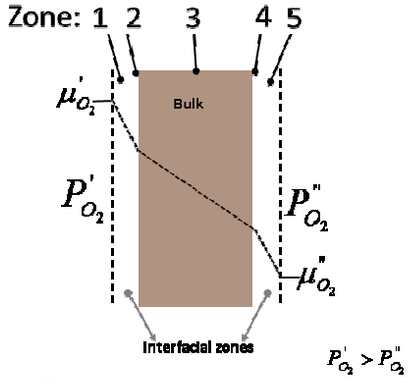

Zone 1 and 5: Gas phase transport
Zone 3: Bulk diffusion
Zone 2 and 4: Surface exchange reaction

Figure 2.5: The dense membrane showing the corresponding transport resistances and the drop of chemical potential (μ' and μ'') across the bulk and interfacial zones of a membrane under a partial pressure gradient. P'_{O_2} and P''_{O_2} are the partial pressures on the high oxygen content surface (feed side) and the low oxygen content surface (permeate side), respectively.

The oxygen fluxes at the membrane surfaces (zone 2 and 4) are controlled by the kinetics of the surface exchange reactions during dissociation/association. Similarly, the oxygen flux through the membrane is controlled by the bulk diffusion. The flux observed from bulk diffusion has an inverse relationship with the thickness of the membrane according to Wagner equation [17, 18]. Either of these two resistances (surface kinetics or bulk diffusion) affects the oxygen flux through the entire membrane. Therefore, depending on which of the above-mentioned resistances is rate limiting for the MIEC membrane, appropriate modification measures can be employed to improve flux.

2.1.3.1 Bulk transport – Wagner equation

The transport through the dense membrane is described by solid state diffusion whereby, the oxygen ions hop through the vacancies in the crystal lattice under a gradient in chemical potential as the driving force. The basic assumption is that this lattice diffusion determines the overall permeation rate [17]. This can be attributed to the fact that the resistance to electronic transport in perovskites is so small that they can move freely and faster relative to the oxygen vacancies.

The interaction between the oxide lattice and O_2 molecule can be represented using the Kröger-Vink [78] notation as

$$\frac{1}{2}O_2 + V_{\ddot{O}} + 2e' = O_0^x \tag{2.2}$$

With the assumption that oxygen vacancies are the mobile ionic defects and neglecting surface exchange reaction, and cross terms between fluxes, the flux, j_k, of a single charge carrier, k, can be represented as [17, 79],

$$j_k = -\frac{\sigma_k}{z_k^2 F^2}\nabla\hat{\mu}_k, \tag{2.3}$$

$$\text{where } \nabla\hat{\mu}_k = \nabla\mu_k + z_k F\nabla\phi \tag{2.4}$$

σ_k = conductivity of charge carries
z_k = charge number
F = Faraday constant
$\nabla\mu_k$ = gradient of electrochemical potential
$\nabla\phi$ = gradient in electrical potential

The flux for oxygen ions as charge carriers is

$$j_{O^{2-}} = -\frac{\sigma_{O^{2-}}}{z_{O^{2-}}^2 F^2}\nabla\hat{\mu}_{O^{2-}} \tag{2.5}$$

$z_{O^{2-}}$ = charge number = -2

Whereas the flux for electrons as charge carriers is

$$j_e = -\frac{\sigma_e}{z_e^2 F^2}\nabla\hat{\mu}_e \tag{2.6}$$

z_e = charge number = -1

The dissociation of half an oxygen molecule and subsequent incorporation of the oxygen ions into the crystal lattice requires two oxygen vacancies and two free negatively charged electrons. The fast diffusion of the charge carriers causes a gradient in the electrical potential. If the transport of charges through the lattice does not affect the internal defect chemistry, the chemical potential gradients of the individual charged species are equal to the chemical potential of the gaseous oxygen. At local chemical equilibrium,

$$\frac{1}{2}\nabla\mu_{O_2} + \nabla\hat{\mu}_{V_{\ddot{O}}} + 2\nabla\hat{\mu}_e = 0, \text{ and} \tag{2.7}$$

$$\nabla\mu_{e'} + \nabla\mu_{h^{\cdot}} = 0 \tag{2.8}$$

holds, where μ_{O_2}, $\mu_{V_{\ddot{O}}}$, and μ_e are the chemical potential gradient for the oxygen vacancy, electrons and electron holes, respectively. $\mu_{V_{\ddot{O}}} = \mu_{O^{2-}}$. At steady state, these transports are in equilibrium and charge accumulations do not occur. As a result, a gradient in electrical potential is not established at steady-state,

$$\nabla\mu_{O_2} - 2(\nabla\mu_{O^{2-}} + z_{O^{2-}}F\nabla\phi) + 4(\nabla\mu_e + z_eF\nabla\phi) = 0 \quad (2.9)$$

$$\nabla\mu_{O_2} - 2(\nabla\mu_{O^{2-}} - 2F\nabla\phi) + 4(\nabla\mu_e - F\nabla\phi) = 0 \quad (2.10)$$

$$\nabla\mu_{O_2} - 2\nabla\mu_{O^{2-}} + 4\nabla\mu_e = 0 \quad (2.11)$$

As can be seen the potential term, $\nabla\phi$, cancels out. In addition, the charge balance between ions and electrons with respect to no charge accumulation can be related as

$$2j_{O^{2-}} + j_e = 0 \quad (2.12)$$

Substituting the fluxes for oxygen ion and electron from Equations (2.5) and (2.6), respectively, in the charge balance equation yields

$$-2\frac{\sigma_{O^{2-}}}{(-2)^2F^2}\nabla\hat{\mu}_{O^{2-}} - \frac{\sigma_e}{(-1)^2F^2}\nabla\hat{\mu}_e = 0 \quad (2.13)$$

This can be further simplified to give

$$\sigma_{O^{2-}}\nabla\hat{\mu}_{O^{2-}} + \sigma_e\nabla\hat{\mu}_e = 0 \quad (2.14)$$

The flux of O_2 is

$$j_{O_2} = \frac{1}{2}j_{O^{2-}}, \quad (2.15)$$

$$j_{O_2} = -\frac{1}{2}\frac{\sigma_{O^{2-}}}{(-2)F^2}\nabla\hat{\mu}_{O^{2-}} \quad (2.16)$$

Therefore, substituting Eq. (2.14) in Eq. (2.11) and finally substituting the outcome in Eq. (2.16), the oxygen flux through the membrane can be evaluated by

$$j_{O_2} = -\frac{1}{16F^2}\left[\frac{\sigma_e\cdot\sigma_{O^{2-}}}{\sigma_e+\sigma_{O^{2-}}}\right]\nabla\mu_{O_2}. \quad (2.17)$$

Where σ_e and, σ_{ion} are the partial electronic and ionic conductivity respectively. Using the relationship,

$$\nabla\mu_{O_2} = RT\frac{\partial\ln P_{O_2}}{\partial x} \quad (2.18)$$

R = molar gas constant L = Membrane thickness

T = temperature P_{O_2} = oxygen partial pressure

and substituting it in Eq. (2.17) yields the Wagner equation

$$j_{O_2} = -\frac{RT}{16F^2}\frac{1}{L}\int_{\ln p'_{O_2}}^{\ln p''_{O_2}}\sigma_{amb}\,d\ln p_{O_2}, \quad (2.19)$$

$$\text{where } \sigma_{amb} = \frac{\sigma_e\cdot\sigma_{O^{2-}}}{\sigma_e+\sigma_{O^{2-}}}. \quad (2.20)$$

The Wagner equation can be further simplified for perovskites like BSCF where $\sigma_{el} \gg \sigma_{ion}$ with the assumption that $\sigma_{ion} \neq f(P_{O_2})$ to

$$j_{O_2} = -\frac{RT}{16F^2}\frac{1}{L}\sigma_{amb}\ln\frac{p''_{O_2}}{p'_{O_2}}. \qquad (2.21)$$

2.1.3.2 Surface exchange

Considered with respect to characteristic thickness

Bulk transport is more dominating for thick membrane, while the surface transport effect is very minimal. The inverse relationship between the membrane thickness and flux in Wagner equation (Eq. (2.21)) underscores the need for a very thin membrane. However, the surface exchange becomes more rate-limiting with decrease in membrane thickness. There is a need to extend the Wagner equation for cases where the surface exchange kinetics controls the transport. Schematically, the bulk and interfacial zones of a membrane are as presented in Figure 2.5. The individual zones yield separate chemical potentials which sum up to the total chemical potential as

$$\Delta\mu_{O_2}^{total} = \Delta\mu_{O_2}' + \Delta\mu_{O_2}^{bulk} + \Delta\mu_{O_2}'' \qquad (2.22)$$

$\Delta\mu_{O_2}^{bulk}$ = driving forces at the bulk

$\Delta\mu_{O_2}'$ = driving forces at the low-pressure interface zone

$\Delta\mu_{O_2}''$ = driving forces at the high-pressure interface zone

The low and the high-pressure sides are represented with the single and double prime, respectively. The rate limiting/the controlling process between the bulk diffusion and the surface exchange kinetics receive a greater proportion of the driving force [17, 80]. The oxygen flux, j_{O_2}, through the membrane (bulk and interfacial zones) according to the Onsager relation [81] is given as

$$j_{O_2} = -j_{ex}^0{}'\frac{\Delta\mu_{O_2}'}{RT} = -\frac{\overline{t_{el}\sigma_{ion}}}{16F^2}\frac{\Delta\mu_{O_2}^{bulk}}{L} = -j_{ex}^0{}''\frac{\Delta\mu_{O_2}''}{RT} \qquad (2.23)$$

j_{ex}^0 = surface exchange rate

where t_{el} and t_{ion} are the fractions (transference number) of the total conductivity provided by electronic and ionic defects [17], and $t_{el}t_{ion}\sigma_{total} = t_{ion}\sigma_{el} = t_{el}\sigma_{ion}$. $\overline{t_{el}\sigma_{ion}}$ is the average value of the product across the membrane thickness. According to Bouwmeester *et al*. [80], t_{el} was set to 1. Using isotope exchange measurements, j_{ex}^0, can be determined by surface exchange coefficient, k_s, and the equilibrium concentration of oxygen anions, c_o.

$$j_{ex}^0 = \frac{1}{4}k_s c_o \qquad (2.24)$$

For very small p_{O_2} gradient across the membrane, $j_{ex}^0{}' = j_{ex}^0{}''$, and adopting the condition for mixed control where the total driving force is equal for both bulk diffusion ($\Delta\mu_{O_2}^{bulk}$) and surface exchange $\Delta\mu_{O_2}^{surface}$ ($\Delta\mu_{O_2}^{surface} = \Delta\mu_{O_2}' + \Delta\mu_{O_2}''$). Comparing the bulk flux to the surface flux for this small p_{O_2} gradient across the membrane, the flux balance would be;

$$-\frac{t_{el}\,\sigma_{ion}}{16F^2L}\Delta\mu_{O_2}^{bulk} = -j_{ex}^{0}\frac{\Delta\mu_{O_2}^{surface}}{RT}\ . \tag{2.25}$$

Therefore, from Eq. (2.23) the condition of mixed control stated above is satisfied at a characteristic thickness expressed as

$$L_c = \frac{RT}{16F^2}\frac{t_{el}\sigma_{ion}}{j_{ex}^{0}}, \tag{2.26}$$

The concept of the characteristic thickness, L_c, according to Bouwmeester *et al.* [17] can be used to determine the rate limiting steps for dense OTM. L_c represents the thickness at which the oxygen transport is equally governed by bulk diffusion and surface exchange kinetics. Below this thickness the transport is limited by surface exchange kinetics.
Incorporating the characteristic thickness (Eq. (2.26)) in Eq. (2.13), the entire oxygen flow through a symmetrical membrane is governed by:

$$j_{O_2} = -\frac{RT}{16F^2}\frac{1}{L}\frac{1}{1+\left(\frac{2L_c}{L}\right)}\sigma_{amb}\ln\frac{\mathrm{p}_{O_2}^{''}}{\mathrm{p}_{O_2}^{'}} \tag{2.27}$$

Here, $2L_c$ implies the same exchange rate on both sides of the membrane if the membrane is symmetric. In perovskite material where $\sigma_{el} \gg \sigma_{ion}$ and with the assumption that the ionic conductivity is purely anionic, it can be represented using the Nernst-Einstein relation [82] as

$$\sigma_{ion} = \frac{c_o D_s z_o^2 F^2}{RT} \tag{2.28}$$

D_s = self diffusion coefficient z_o = valence charge number = -2

Inserting Eq. (2.24) and Eq. (2.28) in (2.26) while setting $t_{el} = 1$ yields,

$$L_c = \frac{D_s}{k_s} \tag{2.29}$$

The self-diffusion can be assumed to be equivalent to the tracer diffusion if the correlation effect and the effects due to mass difference are neglected.

Considered with correlation to oxygen partial pressures

Xu and Thompson [79] developed an explicit model for oxygen permeation based on the analysis of the individual step of the permeation mechanism. Considering also oxygen transport through a perovskite type system, similar assumptions as in section 2.2.1.1 were also assumed here. The oxygen flux with respect to oxygen vacancy as the charge carrier can be expressed in the form of Fick's law by using $\nabla\mu_k = RT\nabla\ln C_v$ and combining equations (2.3), (2.11), and (2.15) to be

$$j_{O_2} = \frac{D_v}{2L}(C_v^{''} - C_v^{'}). \tag{2.30}$$

D_v = diffusion coefficient of oxygen vacancies
$\mathrm{c}_o^{'}$, and $\mathrm{c}_o^{''}$ = concentration of oxygen vacancies at the high- and low-pressure side of the membrane, respectively

Surface exchange kinetics also governs the concentration of oxygen vacancies on the surfaces of the membrane [79];

$$\frac{1}{2}O_2 + V_O^{\cdot\cdot} \overset{k_f/k_r}{\rightleftharpoons} \mathrm{O}_0^x + 2h^{\cdot} \tag{2.31}$$

$$\mathrm{O}_0^x + 2h^{\cdot} \underset{k_r/k_f}{\rightleftharpoons} \frac{1}{2}O_2 + V_O^{\cdot\cdot} \tag{2.32}$$

Where k_f and k_r are the forward and the reverse reaction rate constants at zone 2 and 4, respectively, as presented in Figure 2.5. At steady state under isothermal conditions, the reverse and forward reactions at zone 2 and 4, respectively, are of pseudo zero-order [79]. This can be attributed to the high electronic conductivity, thereby making the electron holes constant at both surfaces. Therefore,

$$j_{O_2} = k_f P_{O_2}^{'0.5} C_v^{'} - k_r \tag{2.33}$$

$$j_{O_2} = k_r - k_f P_{O_2}^{'0.5} C_v^{"}. \tag{1.34}$$

Solving Eq. (2.30), (2.33), and (1.34) simultaneously, the oxygen permeation through the membrane can be described by

$$j_{O_2} = \frac{D_v k_r (\mathrm{P}_{O_2}^{'\ 0.5} - \mathrm{P}_{O_2}^{"\ 0.5})}{2L k_f (\mathrm{P}_{O_2}^{'\ 0.5} \cdot \mathrm{P}_{O_2}^{"\ 0.5}) + D_v (\mathrm{P}_{O_2}^{'\ 0.5} + \mathrm{P}_{O_2}^{"\ 0.5})} \tag{2. 35}$$

The diffusion coefficient and the reaction rate constants are temperature dependent. They can be determined by fitting experimental oxygen permeation data as a function of temperature. Introducing surface exchange coefficients $k_{ex}^{'}$ and $k_{ex}^{"}$ for the interfacial zones 2, and 4, respectively and expressing the equilibrium concentration in terms of partial pressures at the interfacial zone by setting $j_{O_2} = 0$ yields

$$k_{ex}^{'} = k_f \, \mathrm{P}_{O_2}^{'\ 0.5} \tag{2.36}$$

$$k_{ex}^{"} = k_f \, \mathrm{P}_{O_2}^{"\ 0.5} \tag{2.37}$$

Therefore, the transport at the oxygen rich surface, oxygen lean surface, and the bulk can be described by Eq. (2.38-2.40), respectively.

$$j_{ex}^{'} = k_r \left[\left(\frac{\mathrm{P}_{O_2}^{'}}{\mathrm{P}_{O_2}^{"}} \right)^{0.5} - 1 \right] \tag{2.38}$$

$$j_{ex}^{"} = k_r \left[1 - \left(\frac{\mathrm{P}_{O_2}^{"}}{\mathrm{P}_{O_2}^{'}} \right)^{0.5} \right] \tag{2.39}$$

$$j_{diff} = \frac{D_v k_r}{2L k_f} (\mathrm{P}_{O_2}^{'\ 0.5} - \mathrm{P}_{O_2}^{"\ 0.5}) \tag{2.40}$$

The oxygen flux is then determined based on the rate limiting step. This explicit model according to Ref. [79] can also be employed for the evaluation of the surface exchange effects. However, for the scope of the present work, the consideration of the surface exchange according to Bouwmeester *et al.* [17] was employed.

2.1.4 Dense membrane modifications for flux improvement

2.1.4.1 Surface modification

In a situation whereby, the surface exchange reaction is rate-limiting, modifying the membrane surface by roughening it would increase the surface-to-volume ratio [83, 84]. This technique has been reported to increase flux. In addition, coating the surface of the dense MIEC membrane with a porous layer is also another effective means to increase surface area. The porous layer can be of the same material as the dense MIEC membrane or a different MIEC material [85-91]. In comparison to the roughening technique, coating a porous layer has proven to be more effective. Coating a catalytic layer on the membrane surface to increase adsorption and dissociation of oxygen is another way to improve flux. Research studies on the deposition of palladium or platinum catalyst on the surface of MIEC membranes; have demonstrated an increase in oxygen flux in comparison to the unmodified membrane surfaces [88, 92-94]. Similarly, the oxygen permeability of an LSCF membrane was significantly improved by coating the open surface of the hollow fibre with a silver catalyst.

2.1.4.2 Reduction of membrane thickness

According to the Wagner equation (Eq. 2.27), reducing the thickness of the membrane when the bulk diffusion is the rate limiting step invariably increases the oxygen flux but reduces the mechanical stability with consideration to the operating condition. Niehoff *et al.* [95] showed the effect of reducing the membrane thickness by varying the membrane thickness from 0.9 mm to 20μm. Oxygen flux through the membranes increased reciprocally with the membrane thickness. Reducing the thickness below the characteristic membrane thickness, L_c, the diffusion processes become sufficiently fast, which leads to a change in the kinetic behaviour [17].

Notwithstanding the improvement in the transport rate across the thin membrane, the low mechanical stability of free-standing membrane motivated the processing of asymmetric membranes, where the thin membranes are supported by a porous structure [95, 96].

2.2 Asymmetric membranes

Initial studies with regards to asymmetric membranes were the coating of thin layers of MIEC OTM on conventional porous substrates like alumina (Al_2O_3). However, the use of the same material for both the membrane and the porous support avoids chemical and physical incom-

patibility [16, 21, 85, 89, 97, 98]. Numerous studies [16, 19, 93-98] have shown flux improvement for an asymmetric membrane when compared to the thick dense membrane. However, the flux observed [21, 98] from asymmetric membranes is not commensurate to the thickness of the thin dense membrane with regards to Wagner equation [16-19]. Li *et al.* [20] showed through a permeation experiment for both H_2 and CO_2 that the flux observed for thin supported membrane when compared to thick dense membrane was not as high as expected. This is due to the fact that non-adequate support microstructure becomes rate-limiting for the gas transfer.

Novel fabrication methods for instance, freeze-casting [22-27], and phase inverse casting [28, 29] have been lately under investigation as a means to optimize microstructure of the porous support. This is because the porosity, tortuosity, pore opening diameter and the morphology of the pores are tailored and controlled based on the processing route. In comparison to bulk membranes, the resulting architectures from these fabrication routes offer various advantages; improving flux, reducing concentration polarization, etc. Reason is that tailored microstructures might possess channel-like pores with reduced tortuosity (flow path for the diffusing species). Using different membrane materials; these asymmetric membranes have demonstrated an improvement on permeation rate [16, 30, 31]. However, the effect of the porous support on the overall flux through an asymmetric membrane is still not negligible.

2.2.1 Transport processes

In membrane application, either the 3-end mode or 4-end mode of transport (Figure 2.6) is been employed during the separation/mixing process. For both processes, there is a feed gas which is the gas mixture to be separated. When this feed gas reaches the surface of the membrane, the desired specie is transported across the membrane and collected as the permeated gas, while the depleted gas is been collected as the retentate gas.

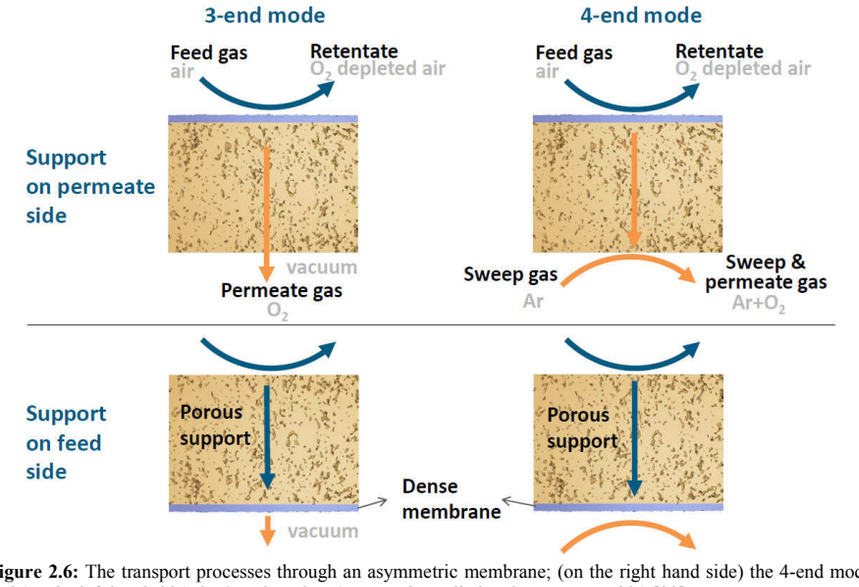

Figure 2.6: The transport processes through an asymmetric membrane; (on the right hand side) the 4-end mode and (on the left hand side) the 3-end mode (vacuum is applied at the permeate side) [99]

The difference between the 4-end mode and the 3-end mode transport process is how the permeated gas is collected. Sweep gas is used to remove the permeated gas in 4-end mode while vacuum is applied for the removal of the permeated gas in the 3-end mode. In the present work, these transport processes were considered during the simulation of the transport through an asymmetric membrane.

2.3 Porous substrate

Porous materials are encountered in a wide variety of technologies, where it is been employed for filtration, mixing or reacting transported species, and separation purposes. The description of the transport process of multicomponent or single component fluid through porous media (from nano-porous to micro-porous media) is of great interest for the modelling of a wide range of processes. As such, the transport of gaseous component through porous media has been extensively studied. In the past, many models and theories have been proffered that, although correct in rendering experimental observations, are inadequate on closer inspection. This may be attributed to the fact that the porous media is not properly being considered or not considered at all.

In the case of gas transport in porous media, the material-specific characteristics of the membrane material, the geometry of the media, as well as the thermodynamic laws for the gas must be considered. This is so because the thermodynamic and chemical properties of the gas and

the material play a major role. In addition, all gas molecule interactions (self, gas-gas, and gas-wall) should be considered.

2.4 Transport mechanism in porous support

The transport mechanisms through porous structures have a dependency on the pore morphology (e.g. size of the pore, pore shape, etc.), porosity, pressure, the size of the transported molecule and interconnected pores. A relationship between pore size and porosity exists [100]. The interconnected pores are essential for the evaluation of the effective porosity of the structure. Notwithstanding that high porosity of the porous structure yields a high permeability, however, it limits the relative strength [101]. Therefore, an understanding of the transport processes through pore is essential. The molecular mean free path length, λ, of the particle is the average distance a molecule can travel between two collisions, and is represented as

$$\lambda = \frac{K_b T}{\sqrt{2}\pi d^2 P}, \tag{2.41}$$

K_b = Boltzmann constant d = pore diameter

The predominating gas transport process for high temperature (~ 900°C) can be deduced from the relationship between the mean free path length and the average pore diameter [102]. The Knudsen number, *Kn*, [103] is the defining parameter for differentiating between different transport modes.

$$Kn = \frac{\lambda}{d} \tag{2.42}$$

Knudsen diffusion (Figure 2.7.a) occurs when the molecular mean free path is much larger than the pore diameter in which the diffusing molecules are being transported. As a result, the molecules tend to collide with the wall rather than colliding with other molecules. This transport mechanism occurs usually when $Kn \gg 1$ and for pore sizes in the range of 10-100 nm. The total momentum of the gas molecules is not conserved in this case and the molecules move at different rates as a function of thermal mobility, which depends on the molecular mass. The transport of molecules of different type is independent of each other. In a straight cylindrical tube with pore diameter *d* and length *L*, the Knudsen flux can be evaluated using [104]

$$j_i^{K,cap} = -CD_i^K \nabla x_i \tag{2.43}$$

$j_i^{K,cap}$ = molar Knudsen flux of gas *i* C = total molar density

∇x_i = gradient in the mole fraction of specie *i* D_i^K = the Knudsen diffusion coefficient for gas *i*

The Knudsen diffusion coefficient for gas *i* can be represented as;

$$D_i^K = \frac{d}{3}\sqrt{\frac{8RT}{\pi M_i}} \tag{2.44}$$

M_i = molecular weight of the gas molecule.

The ratio of the porosity and the tortuosity factor can be included in the Knudsen diffusion coefficient to take into the consideration the geometry of the porous media

A molecular sieve is a material that has very small, yet definite uniformly sized pores. In molecular sieving as shown in Figure 2.7.b, the separation of gas components is based on the differences in the kinetic diameter of the gas molecules. The pores are expected to be small enough as to allow the passage of smaller molecules and hinder that of larger molecules.

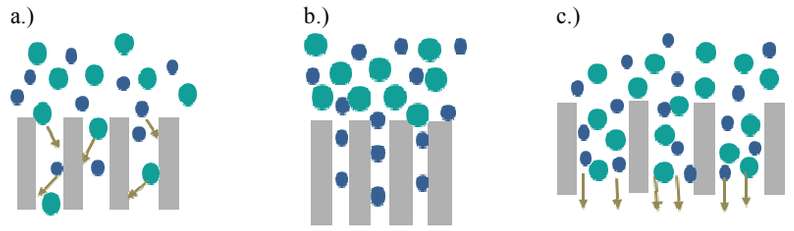

Figure 2.7: The (a) the Knudsen diffusion, (b) the molecular sieving, and (c) viscous flow mechanism of transport in porous media.

The mechanism of viscous flow (Figure 2.7.c) occurs when the pore diameter is greater than the mean free path of a gas molecule. In this transport mechanism, $Kn \ll 1$. In contrast to the Knudsen diffusion, the probability of the particles colliding is higher than a collision between pore wall and gas particles. As such, the total momentum is conserved since the momentum is transferred from gas molecule to gas molecule. The total pressure gradient is the driving force for a viscous flow, and this maintains same speed for all transported gas molecules. Considering viscous flow in a capillary, the Hagen Poiseuille equation can be used to describe the flow rate

$$Q = \frac{\Delta P \pi R^4}{8 \eta L} \tag{2.45}$$

Q = total discharge (flow rate) η = viscosity

ΔP = total pressure drop L = length over which the pressure drop is taking place

Similarly, the Darcy law can also be used for the description of a viscous flow through a porous media, and can be represented as;

$$Q = \frac{B_0 A \Delta P}{\eta L} \tag{2.46}$$

B_0 = intrinsic permeability of the medium A = cross-sectional area

Multiplying the obtained volumetric flow rate with the total molar concentration of the transported species, C_i, yields the viscous flux, j_{visc}, as

$$j_{visc} = -C \frac{B_0 \Delta P}{\eta L}. \tag{2.47}$$

2.5 Transport models for porous media

Considering the different models that have been employed for the quantification of the diffusive transport through the porous structure, Fick's law and the Graham's law are the basis for understanding of the gas diffusion phenomena. Amongst these models, Fick's law is the most popular approach owing to its simplicity. The validity of the application of Fick's law for the description of transport through porous media has been questioned [105-107] and found not sufficient under many operating conditions. Maxwell-Stefan model (MSM) [106, 108], which is simply an extension of the Fick's law for multicomponent mixture is an approach often employed. Comparison between MSM and the Fick's law pointed out special conditions where Fick's law is appropriate [109]. For the above two models (MSM and Fick's law) efforts have be made to account for the porous media without altering the basic transport equation. They can be better applied for the description of diffusive transport in open space but not to porous media. Another widely used model is the advective dispersive model (ADM) [110]. It is a linear addition of advection and ordinary diffusion calculated by Darcy's law and Fick's law, respectively. The ADM considers the Knudsen diffusion or slip effects using a Klinkenberg factor for advection. The effect of porous media is included through a porosity-tortuosity-gas saturation factor.

Evans *et al.* [111-115] presented the dusty gas model (DGM), which combines different transport mechanisms as well as the effect of the porous media. In this approach, the porous media is assumed to be a large molecule fixed in space. The material component is treated as a very heavy gas and the resulting gas mixture of heavy gas (porous media) and light gas (permeating gas) is considered. Cunningham and Williams [116] have extensively reviewed this work. Kerkhof [32] however, found an inconsistency within the dusty gas model where the viscous flux was considered twice. For a better description of the situation, Kerkhof derived the "Binary Friction Model" (BFM) starting from the Lightfoot equation [117], and it combines bulk diffusion, Knudsen diffusion and viscous flow. The analytical description of the transport through the porous support using the binary friction model according to Kerkhoff [32] has been observed to be sufficient [20, 21, 95, 118, 119].

2.5.1 The Binary Friction Model

Entropy is the degree of randomness or disorder in a system. Therefore, a complete description of entropy changes taking place in a system should also provide a description for all spontaneous processes which are possible in that system. The general conservation equation for entropy is

$$\rho \frac{\mathrm{d}\hat{S}}{\mathrm{d}t} = -\left(\nabla \cdot j_s\right) + \sigma \tag{2.48}$$

$\hat{S}$ = entropy per unit mass

j_s = entropy flux relative to the mass average velocity

σ = volumetric rate of entropy production

2.5. Transport models for porous media

The complete description of the rate of entropy production considers all-natural processes possible in a system being considered. This agrees with first postulates of non-equilibrium thermodynamics which states that "Departures from local equilibrium are sufficiently small that all thermodynamic quantities may be defined locally by the corresponding relations for systems in equilibrium". Therefore, the rate of entropy production [32, 117, 120] due to diffusion can be represented as

$$T\sigma = -\sum_{i=1}^{n}\left(\nabla_T \tilde{\mu}_i - \tilde{F}_i\right)\cdot j_i \tag{2.49}$$

where j_i is the mass diffusion flux with respect to the mass average velocity. $j_i = \rho_i\left(u_i - v\right)$ and $\rho_i = c_i M_i$; ρ_i is the mass density of *i*, u_i is the velocity of diffusion of species *i*, v is the mass average mixture velocity, c_i is the molar density of *i*, and M_i is the molar mass of specie *i*. *T* is the absolute temperature, $\nabla_T \tilde{\mu}_i$ represents the isothermal gradient of the specific chemical potential; $\tilde{\mu}_i$ is the specific chemical potential of species *i*, $\tilde{\mu}_i = \mu_i / M_i$. $\tilde{F}_i = F_i / M_i$; F_i is the external body force per mole of species *i*. Eq. (2.49) can be rewritten as

$$T\sigma = -\sum_{i=1}^{n}\left(c_i \nabla_{T,p}\,\mu_i + c_i \overline{V}_i \nabla p - \rho_i \tilde{F}_i\right)\cdot\left(u_i - v\right) \tag{2.50}$$

$$\omega_i = c_i \overline{V}_i \tag{2.51}$$

$\overline{V}_i$ = partial molar volume of *i* ω_i = volume fraction of species *i*

$\nabla_{T,p}\,\mu_i$ = isothermal-isobaric gradient of the molar chemical potential

The driving force per unit volume of mixture to move species *i* relative to the mixture is represented as

$$c_t RT\, e_i = c_i \nabla_{T,p}\,\mu_i + \phi_i \nabla p - \rho_i \tilde{F}\,, \tag{2.52}$$

$$\text{with } \sigma = -c_t R \sum_{i=1}^{n} e_i \cdot\left(u_i - v\right). \tag{2.53}$$

Comparing with Maxwell-Stefan equation also shows e_i to be

$$e_i = \sum_{j=1}^{n} \frac{x_i x_j}{D_{ij}}\left(u_i - u_j\right). \tag{2.54}$$

Expressing Eq. (2.54) in terms of the molar fluxes ($N_i = c_i u_i$) and substituting it in Eq. (2.52) and rearranging the equation gives

$$\frac{x_i \nabla_{T,p}\,\mu_i}{RT} + \frac{\omega_i}{c_t RT}\nabla p - \frac{\rho_i}{c_t RT}\tilde{F}_i = \sum_{j=1}^{n} \frac{x_i N_j - x_j N_i}{c_t D_{ij}} \tag{2.55}$$

R = molar gas constant D_{ij} = effective binary diffusion coefficient

With the assumption that the transport equation does not change with pore averaged quantities, it is reasonable to add the friction force with the membrane to the averaged intermolecular friction terms. Therefore, the Lightfoot equation for binary solution becomes

$$\frac{x_i \nabla_{T,p}\mu_i}{RT} + \frac{\omega_i}{c_t RT}\nabla p - \frac{\rho_i}{c_t RT}\tilde{F}_i = \sum_{j=1}^{n}\frac{x_i N_j - x_j N_i}{c_t D_{ij}} - r_{im}N_i \tag{2.56}$$

For isothermal gases with consideration to slip flow [32, 116, 121],

$$\frac{x_i \nabla_{T,p}\mu_i}{RT} + \frac{\omega_i}{c_t RT}\nabla p = \sum_{j=1}^{n}\frac{x_i N_j - x_j N_i}{c_t D_{ij}} - r_{im}N_i . \tag{2.57}$$

Assuming an ideal gas behavior and considering the flux through the pores [32],

$$\nabla x_i + \frac{x_i}{P_t}\nabla p_t = RT\sum_{j=1}^{n}\frac{x_i N_j - x_j N_i}{c_t D_{ij}} - r_{im}N_i . \tag{2.58}$$

Eq. (2.58) can alternatively be formulated as

$$\frac{1}{P_t}\vec{\nabla}P_i = RT\sum_{j=1}^{n}\frac{(x_i\vec{N}_j - x_j\vec{N}_i)}{P_t D_{ij}^{eff}} - r_{im}\vec{N}_i \tag{2.59}$$

P_t and P_i = total and partial pressure of the diffusing specie

r_{im} = friction term

The Binary Friction Model (BFM) [32] which is a modification of the Lightfoot equation [117] has been found to be sufficient in describing the transport through the porous support.

2.5.1.1 Single gas permeation

The Maxwell-Stefan term of the BFM cancels when summed over all species present

$$\frac{1}{P_t}\vec{\nabla}P_t = -\sum_{i=1}^{n} r_{im}\vec{N}_i \tag{2.60}$$

The Eq. (2.60) can be further simplified for single gas permeation as

$$\frac{1}{P_g}\vec{\nabla}P_g = -r_{im}\vec{N}_g \tag{2.61}$$

The friction term considers Knudsen diffusion and viscous flow as

$$\frac{1}{r_{im}} = \frac{P_g}{RT}\left(D_g^K + \frac{B_0 P_g}{\eta_g}\right) \tag{2.62}$$

and the Knudsen diffusion coefficient, D_g^K is evaluated by

$$D_g^K = \frac{d_{pore}}{3}\sqrt{\frac{8K_B T}{\pi M_g}} \times \frac{\varepsilon}{\kappa} \tag{2.63}$$

B_o = permeability
d_{pore} = average pore diameter
κ = tortuosity factor
η = fluid viscosity
ε = porosity
M_g = molecular mass of the gas

Substituting equations 2.62 and 2.63 in Eq. (2.61) yields the single gas permeation equation for BFM

$$N_g = -\frac{\nabla P_g}{RT}\left(\frac{\varepsilon}{\kappa} D_g^K + \frac{B_o P_g}{\eta_g}\right) \tag{2.64}$$

2.5.1.2 Permeation of gas mixtures

The BFM equation for the gas mixture permeation can be obtained by also starting from Eq. (2.59). In the present study oxygen / or air and argon were used as feed and sweep gas, respectively, and there was no flux of argon or nitrogen through the membrane.

$n = 2$ (n is the number of species),

$i = 1 \equiv O_2$, $i = 2 \equiv Ar / N_2$, $N_1 = O_2$ flux, and N_2 = Argon or Nitrogen flux = 0, and the flux of each specie from Eq. (2.59) is

$$\frac{1}{P_t}\vec{\nabla} P_1 = -\frac{RTx_2 N_1}{P_t D_{12}} - r_{1m} N_1 \tag{2.65}$$

The mole fraction of the species can be obtained as

$$x_i = \frac{P_i}{P_t} \tag{2.66}$$

The interspecies friction term is absent for gas mixture permeation, but a modified coefficient is introduced as

$$f_{im} = \frac{\beta_{im}}{x_i} = \frac{RT}{P_t}\left(D_i^K + \frac{B_o}{k_i}\right)^{-1} \tag{2.67}$$

f_{im} = modified wall friction factor — k_i = fractional viscosity coefficient

β_{im} = friction coefficient — n = Number of components in the mixture

The fractional viscosity coefficient can be expressed as:

$$k_i = \frac{1}{P_t}\frac{\eta_i^0}{\sum_{j=1}^{n}\frac{P_j}{P_t}\zeta} \tag{2.68}$$

η_i^0 = pure component viscosity — ζ = interaction parameter

The interaction parameter can be evaluated using Wilke's approximation [122] as

$$\zeta_{ij} = \frac{\left(1 + \left(\frac{\eta_i}{\eta_j}\right)^{1/2}\left(\frac{M_j}{M_i}\right)^{1/4}\right)^2}{\left(8\left(1 + \frac{M_i}{M_j}\right)\right)^{1/2}} \tag{2.69}$$

$$\zeta_{ji} = \left(\left(\frac{\eta_j}{\eta_i}\right)\frac{M_i}{M_j}\right) * \zeta_{ij} \tag{2.70}$$

η_i and η_j are the viscosities of the species *i* and *j*.

Using pure oxygen / or air and Argon (*Ar*) as feed gas and sweep gas, respectively, ζ_{ji} was evaluated by solving Eq. (2.69 and 2.70) to be:

$\zeta_{O_2Ar} = 1.05 = \zeta_{O_2N_2}, \zeta_{ArO_2} = 0.95 = \zeta_{N_2O_2}, \zeta_{O_2O_2} = \zeta_{ArAr} = \zeta_{N_2N_2} = 1.$

For the case considered, the fractional viscosity was approximated to be:

$$k_i \approx \frac{\eta_i}{P_t} \tag{2.71}$$

For a better description of the porous support's pore geometry which is randomly shaped, the ratio of the porosity (ε) and tortuosity (τ) is included to scale it up so as to obtain the effective diffusion coefficient which considers porous media factor.

Therefore, substituting the terms in Eq. (2.65), the equation for obtaining the flux for mixed gas permeation becomes

$$N_1 = \frac{\nabla P_1}{RT} \frac{1}{\frac{P_2}{\frac{\varepsilon}{\kappa} D_{12} P_t} + \frac{1}{\frac{\varepsilon}{\kappa} D_g^K + \frac{B_o P_t}{\eta_1}}} \tag{2.72}$$

3. Experimental methods

3.1 Membrane/sample manufacturing

The inverse relationship between the membrane thickness and the observed flux has been presented according to Wagner equation in section 2.1.3. As such, the reduction of the membrane layer thickness increases the oxygen permeation through the membrane layer. This motivates the processing of an asymmetric membrane whereby this thin dense membrane is supported by a porous support of the same material. These asymmetric membranes were manufactured by my colleagues at institute of energy and climate research (IEK-1) Forschungszentrum Jülich GmbH using $Ba_{0.5}Sr_{0.5}Co_{0.8}Fe_{0.2}O_{3-\delta}$ (BSCF) and $Ba_{0.5}Sr_{0.5}(Co_{0.8}Fe_{0.2})_{0.97}Zr_{0.03}O_{3-\delta}$ (BSCF3Zr) ceramic powder. Sequential tape casting (TC) and freeze casting (FC) were used for the porous support and a subsequent screen printing for the membrane layer. It should be noted that a set of these asymmetric membranes processed from two different routes (tape cast and freeze cast) had comparable porosities. This is to further compare and study the effect of the support microstructure on flux.

3.1.1 Sequential tape casting

This processing route can be used to fabricate thin flat ceramic sheets. Generally, tape thicknesses within the range of 25 µm to 1 mm can be achieved. Notwithstanding, it is still possible to manufacture thin tapes as small as 5 µm. The basic principles of the technique are: firstly, the preparation of the ceramic slurry from a mixture of the ceramic powder, solvent, additives and binder. This ceramic slurry is poured on to a moving tape through the reservoir with the doctor blade controlling the thickness of the tape. This green tape is dried in a horizontal position. Afterwards, the tape is mechanically strong enough to be peeled off and cut into desired shape before sintering. This technique is schematically shown in Figure 3.1. This manufacturing route is described in more details in [14, 16, 71, 119]

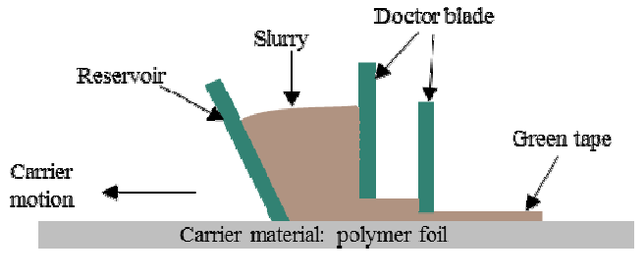

Figure 3.1: Schematically representing a typical tape casting process

3.1.1.1 Sample preparation

Commercially available BSCF and BSCF3Zr powders from Treibacher Industrie AG, Austria were used for the fabrication of asymmetric membranes by tape casting technique. The BSCF3Zr powder exhibits a monomodal particle size distribution with d_{50} ~3.6 µm, while the BSCF powder has an average grain size of d_{50} = 4.2 µm.

The slurry for the tape casting using BSCF3Zr ceramic powder was prepared using an azeotropic mixture of ethanol and methyl ethyl kethone using Nuosperse® FX9086 (Elementis Specialties, Inc.), and Polyvinyl butyral (Butvar® PVB B-98, Solutia Inc.) as the dispersant and the binder, respectively. In addition, Solusolv® 2075 (Solutia Inc.) and PEG400® (Merck) were added as plasticisers. The sequential tape casting was carried out in these steps:

Firstly, using a doctor blade gap of 50 µm, the thin dense membrane was cast on a polymer foil, and was allowed to dry. No pore former was used in the slurry for casting the dense membrane. Afterwards, the porous support was cast on top of the dense membrane with a doctor blade gap of 2.25 mm. In the slurry for casting the BSCF3Zr and BSCF porous support, 40.5wt.% and 30wt.% of pore formers were used, respectively. Corn starch from Cargill C-Gel (Cargill, Germany) with a particle size range of 2–30 µm was then used as the pore former in relation to the total solid content. The pore former burns out leaving a desired porosity. Disc shaped samples were stamped out from the green tape, debindered, and subsequently co-fired in air for 3h at 1130 °C.

Finally, an oxygen activation layer was screen-printed on the top of the already sintered membrane. The ink for screen printing consisted of the same powder (BSCF3Zr or BSCF) as was used for the dense membrane and support layer, 94% terpineol as solvent, and 6% ethylene cellulose as binder. In order to have a porous activation layer that is well attached to membrane surface, these layers were only sintered at 1000 °C for 1h. More details on the in-house manufacturing of asymmetric membranes by tape cast are described in ref. [30, 95, 119].

3.1.2 Freeze casting

Tailored microstructures with straight pore channels can be produced by the method of freeze drying. The process is schematically shown in Figure 3.2. Similar to other conventional processing routes, the slurry is prepared by mixing the powder together with water, binder, and other additives.

The process is based on freezing the prepared slurry, and subsequent sublimation of the solidified solvent under reduced temperature and pressure; the structure is sintered. During the freezing process, the nucleated solvent crystals separate the dispersed particles present in the slurry as the solidification front advances. These particles are trapped in between the advancing solvent crystals (Figure 3.2.b). Afterwards, porous structures with defined pores with re-

spect to the solvent crystals are obtained. This manufacturing route is described in more details in [24, 25].

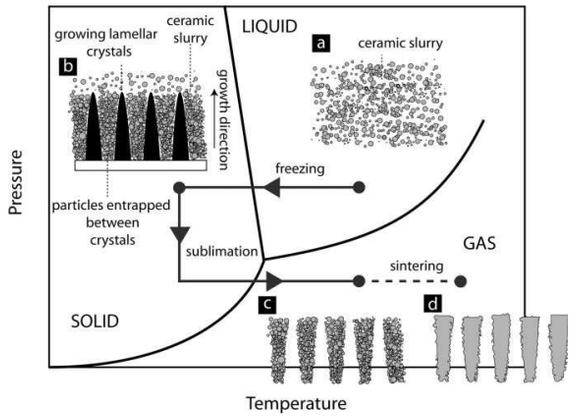

Figure 3.2: The freeze casting steps going from slurry preparation, solidification, sublimation, and finally sintering. [24]

3.1.2.1 Sample preparation

Freeze casting or otherwise known as the freeze drying method was used for the processing of an ice templated porous support. The slurry was prepared by mixing the powder with water, binder (2.5 wt.% PEG4000S, Clariant), and dispersant (2 wt.% Dolapix C64, Zschimmer & Schwarz GmbH & Co). In other to obtain a homogeneous blend, the prepared slurry was mixed in a planetary mixer.

Using a cylindrical Teflon mould with an aluminium base plate cooled to -50°C with a Martin Christ Epsilon 2-4 lyophilizer, the slurry was cast after a homogeneous mixture was obtained. After complete freezing at -55°C and at a pressure of 0.1 mbar pressure for 24 hours, the sublimation of ice crystals took place after a final drying step at +30 °C at the same pressure yielding a solidified structure. The green support was pre-sintered in air with a dwell time of 3 hours at 1050°C. The free support faces were ground off before screen printing. For the fabrication of the screen printing ink for the dense membrane layer, 94wt.% terpineol and 6wt.% ethylcellulose were used as a solvent and a binder, respectively.

Owing to the onset of the nucleation of the ice crystal, the part of the porous support in contact with the polished aluminium base plate had a fine porous region with randomly oriented pores. The dense BSCF3Zr membrane layer was screen-printed on this side of the support, which makes it easier to cover the pores with the screen-printed layer. The entire structure was sintered at 1130 °C in air for 5 hours. Finally, an oxygen activation layer was screen-printed on the top of the already sintered membrane. Same ink for the dense membrane was used for the activation layer, but these layers were only sintered at 1000 °C for 1h in order to have a porous activation layer that is well attached to membrane surface.

3.2 Oxygen permeation

A double chamber quartz glass reactor was used for the permeation measurements. The membrane discs were sealed in between two quartz glass tubes using two gold rings. The transport configuration with the support at the feed side and the dense membrane at the permeate side (see section 2.2.1) was used for the permeation measurement. Oxygen (200 ml/min) or ambient air (250 ml/min) was used as a feed gas, while argon (50 ml/min) was used as a sweep gas. The setup was allowed to run for three hours to give room for equilibration before measurements are taken. The total oxygen permeation rate was calculated by analysing the permeate gas for Ar, O_2, and N_2. Using a mass spectrometer (Pfeiffer OmniStar), the total oxygen permeation rate was calculated. The planar surface area of the membrane was used to divide the oxygen mass flow rate in the permeate gas for the calculation of the permeation rates. The performance of the membranes was measured as a function of temperature and oxygen partial pressure in the feed gas, i.e. ambient air (P_{O_2} = 0.21 bar) and oxygen (P_{O_2} = 1 bar). The pressure at the permeate side was measured at the down stream.

3.3 Analysis of microstructure

Scanning electron microscopy of the polished membrane cross sections was performed with a Zeiss Ultra 55 and a FEI Phenom. Energy-dispersive X-ray spectroscopy (EDX-INCA) was used for elemental analysis. Gas tightness was measured using He leakage testing (Pfeiffer vacuum). Quantitative image analysis was conducted using the commercial software analySIS pro (Olympus Soft Imaging Solutions GmbH, Germany). Same microstructural analysis was carried out on the samples manufactured from BSCF and BSCF3Zr.

3.3.1 µXCT data acquisition

3D microstructure analysis was performed by X-ray computed tomography (XCT) on the membranes after permeation measurements. These samples were embedded in resin by vacuum impregnation to protect the porous structure before cutting. Cylindrical samples with a diameter of 1 mm and a thickness of 0.95 mm were cut using an abrasive cut off wheel.

For the BSCFZr samples, a Zeiss Xradia 520 Versa X-ray microscope with a tungsten transmission target was used. Scanning of the TC sample was performed at a voltage of 140 kV using an HE2 filter. The FC sample was scanned at a voltage of 120 kV using an HE1 filter. Each tomography was acquired with an X-ray source power of 10 W, 20× optical magnification, the binning 2 setting of the 4 Megapixel CCD camera, and an exposure time of 26 s for each radiograph – with 3001 radiographs being taken over 360° [102].

For the BSCF samples, the µXCT data of the sample was acquired using Xradia microXCT (Xradia inc. Pleasanton, CA) system at an X-ray imaging facility of the University of Man-

chester. The samples were scanned at 80 kV using an optical magnification of 40×, with 1801 radiographs being taken over 182°. Ref [95, 119] explains in more details how the computed tomography data was acquired. Finally the recorded data was reconstructed with voxel size of 0.6 µm for the BSCF sample and 0.70 µm for the freeze cast and tape cast sample from BSCF3Zr using Feldkamp–Davies–Kress [123] algorithm.

µXCT data of an inverse tape cast fabricated from BSCFZr powder was received from colleagues at the department of Energy Conversion and Storage, Technical University Denmark (DTU). This was used in this work for the stimulation of viscous flow effect on large pore porous support.

4. Simulation methods

4.1 Geometrical parameters of the porous substrate

4.1.1 Tortuosity and diffusive simulation

The diffusion through the support was modelled by continuum mechanics, solving the Laplace equation in pores with the application of the Neumann boundary condition on the pore/solid boundaries using the FlowDict module of the Geodict software (Math2Market GmbH, Kaiserslautern, Germany). The resulting effective diffusivity equals the ratio of the porosity to the tortuosity factor and depends only on the pore geometry. The effective diffusivity (Eq. (4.1)) describes the effect of support pore space geometry on diffusion:

$$D^{eff} = \frac{\varepsilon}{\kappa} D_{ij} \tag{4.1}$$

For more detailed information on tortuosity and tortuosity factor, see [124-127]. The tortuosity factor (κ) describes how strongly the effective diffusivity is reduced by the elongated tortuous pore path between the two faces of the support. The relationship between tortuosity factor and tortuosity (τ), according to Norman Epstein [125], was used in the present study for the evaluation of the tortuosity of the porous structure.

$$\tau = \frac{L_e}{L} \equiv \kappa^{1/2} \tag{4.2}$$

Tortuosity is the ratio of the average length of true flow paths (the pore length), L_e, to the straight-line dimension of the porous medium, L.

$$\kappa = \left(\frac{L_e}{L}\right)^2 \tag{4.3}$$

4.1.2 Pore diameter evaluation

The pore diameter of the porous support was evaluated from the CT data by mimicking the liquid intrusion porosimetry method (simulating the pressing of a non-wetting fluid into the pore and recording the applied pressure and the volume absorbed), using the PoroDict module of the GeoDict software. The resulting pore throat diameter is related to the pressure applied to force the non-wetting fluid into the pore. The connected, closed or blind pores were accounted for by evaluating the percentage of the closed and open pores in the flow direction of the porous support. Open pores are extensive networks of interconnected pores, leading from the surface to the core in any of the Cartesian directions. This can be evaluated by specifying a domain boundary (face, edge or vertex) and then checking if the pore components are connected by the specified domain boundaries. The pore is computed as an open pore if it is connected; otherwise it is computed as a closed pore. Also, isolated pores which do not open to the surface in any direction are referred to as closed pores.

4.1.3 Permeability

Using the FlowDict module of the GeoDict software, the flow experiment was computed virtually by solving the Stokes equation. Subsequently, the results were post-processed to predict the effective material permeability. The flow was assumed to be laminar. The pressure difference during the simulation was set very low (0.02Pa), to ensure the flow to be laminar and that the obtained permeability is a material property independent of the fluid viscosity, pressure drop, or temperature. The permeability B_0 is determined during the post processing by Darcy's law (Eq. (2.46)).

4.1.4 Boundary condition

The boundary condition during the computation of the geometrical parameter from the 3D XCT reconstructed structures can be either periodic or symmetric. This is schematically shown in Figure 4.1 using a slice of the acquired XCT data after flow experiment.

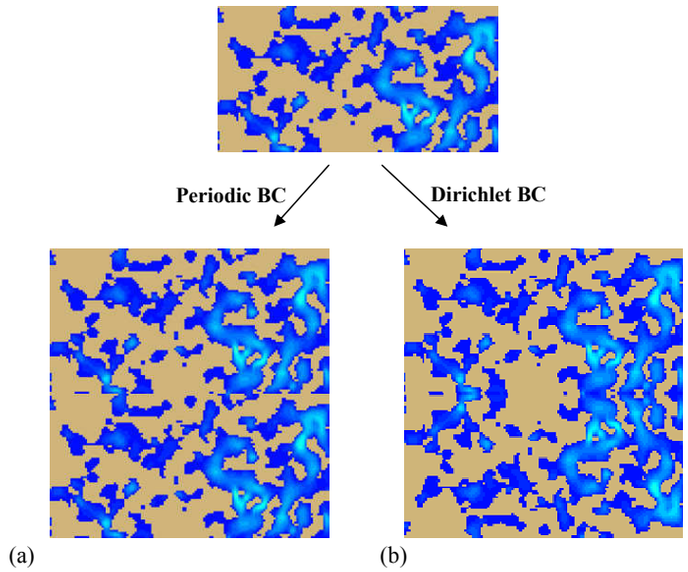

Figure 4.1: 2D slice images of a tape cast structure after flow simulations showing the effect of applying (a) periodic and (b) Drichlet (symmetric) boundary condition on the flow. The blue areas depict the pores and the solid part is in brown

The blue and the brown coloured areas are the pore and solid parts, respectively. Applying the periodic boundary conditions can be simply stated as stacking the structures on opposite faces, while the symmetric is simply stacking on similar faces (mirror imaging while stacking). The stacking for the periodic either constricts the flow paths or blocks it. In a case where the pores

are blocked, the fluid travels a longer path in other to connect to another pore. This increases artificially the tortuous nature of the flow path, whereas, applying the symmetric boundary conditions does not. For periodic boundary condition, less than 50% of the pores are connected. Therefore, the Dirichlet (symmetric) boundary condition (Figure 4.1.a) was preferred over the periodic (Figure 4.1.b) and was used during the computation of the flow parameters. Notwithstanding, applying the symmetric boundary conditions requires more computational time and memory than the periodic boundary condition. For the tangential direction, the boundary condition was set to periodic. This was to mimic the experiment conditions where the sides are sealed off during measurement. For the diffusive transport computation, the boundary condition in the diffusion and tangential direction was also taken to be symmetric. The concentration at the feed side and at the permeate side was set to 1 and 0, respectively.

4.2 Different pressure simplifications of the BFM on flux

4.2.1 One dimensional exact solution of BFM

The total pressure is considered in this configuration not to be constant, rather varying throughout the support thickness, $P_g(X)$, with X the position in the support. This gives a more realistic description of the transport through the porous support, whereby in reality it should vary depending on the position in the support.

For single gas permeation:

$$N_g = -\frac{\nabla P_g}{RT}\left(\frac{\varepsilon}{\kappa} D_g^K + \frac{B_o P_g(X)}{\eta_g}\right) \tag{4.4}$$

The gradient of the partial pressure of the diffusing species can be evaluated by solving

$$\nabla P_g = -N_g RT\left(\frac{\varepsilon}{\kappa} D_g^K + \frac{B_o P_g(X)}{\eta_g}\right)^{-1} \tag{4.5}$$

$$P_g(0) = P_0 \tag{4.6}$$

P_0 can be either equated to P_{gFeed} or P_{gPerm}, if the porous support is positioned on either the feed or permeates side, respectively. $P_g(0) = P_{gFeed}$ when the support is placed at the feed side and $P_g(0) = P_{gPerm}$ when the support is at the permeate side. Solving the Eq. (4.5) using the boundary condition in Eq. (4.6), will give the partial pressure at the membrane support interface (Eq. (4.7)), where X is the position in the support.

$$P_g(X) = \frac{-D_g^K \varepsilon \eta_g + \sqrt{(D_g^K)^2 \varepsilon^2 \eta_g{}^2 + 2B_o D_g^K P_0 \varepsilon \eta_g \kappa + B_o(B_o P_0{}^2 - 2N_g RTX\eta_g)\kappa^2}}{B_o \kappa} \tag{4.7}$$

For mixed gas permeation

4.2. Different pressure simplifications of the BFM on flux

$$N_1 = \frac{\nabla P_1(X)}{RT} \frac{1}{\frac{P_2(X)}{\frac{\varepsilon}{\kappa} D_{12} P_t(X)} + \frac{1}{\frac{\varepsilon}{\kappa} D_g^K + \frac{B_o P_t(X)}{\eta_1}}} \tag{4.8}$$

For gas mixtures, there are total and partial pressure gradients, because there is more than one species involved.

$$\nabla P_t = -RTN_1 \left(\frac{\varepsilon}{\kappa} D_1^K + \frac{B_o P_{t0}}{\eta_1} \right)^{-1} \tag{4.9}$$

$$\nabla P_1 = -RTN_1 \left(\frac{P_t(X) - P_1(X)}{\frac{\varepsilon}{\kappa} D_{12} P_t(X)} + \frac{1}{\frac{\varepsilon}{\kappa} D_1^K + \frac{B_o P_{t0}}{\eta_1}} \right) \tag{4.10}$$

The solution of the varying total pressure in the viscous term of the BFM was non-trivial. As a result, a constant pressure was assumed, but the effect of using a constant pressure in the viscous term was also investigated using an iterative approach (Table 4.1).

Table 4.1: An iterative approach to show the effect of using a constant pressure in the viscous term of the varying pressure configuration of the BFM model

Total pressure (Pa)	**Interface pressure (Pa)**	**Flux (ml cm^{-2} min^{-1})**	**Manual iteration of next total pressure (Pa)**
100000	100320	0.118053	(100320 + 100000)/2 = 100160
100160	100480	0.118036	(100480 + 100160)/2 = 100320
100320	100639	0.118020	(100320 + 100639)/2 = 100479.5
100479.5	100798	0.118004	(100479.5+100798) = 100638.75

The first assumption is made by assuming that the total pressure is 1 bar. After the evaluation of the flux, the total and interface pressure were obtained. The average between the first total pressure and the obtained interface pressure is used as the constant total pressure input in the viscous term. This is similar to solving an averaged pressure in the viscous term for the varying pressure configuration. As can be seen up to 5 iterations, the flux obtained is still similar to the fourth decimal digit. Hence, the constant pressure in the viscous term was employed for the present evaluation.

The pressure gradients were obtained by solving the partial differential equations (Eq. (4.9 and 4.10)) using P_{t0} to be equal to either P_{tperm} or P_{tfeed} (depending on the position of the porous support) as the boundary conditions. The solutions for the total and partial pressure through the porous support for the mixed gas permeation are

$$P_t(X) = \frac{D_1^K \varepsilon \eta_1 P_{t0} + B_o P_{t0}{}^2 \kappa - N_1 RTx\eta_1 \kappa}{D_1^K \varepsilon \eta_1 + B_o P_{t0} \kappa}, \text{ and} \tag{4.11}$$

$$P_1(X) = P_t(X) + \left(P_{1Perm} - P_{t0}\right)\left(\frac{P_{t0}\left(D_1^K \varepsilon \eta_1 + B_o P_{t0}\kappa\right)}{P_{t0}(X)(D_1^K \varepsilon \eta_1 + B_o P_{t0}\kappa)}\right)^{\frac{D_1^K \varepsilon \eta_1 + B_o P_{t0}\kappa}{D_{12}\varepsilon\eta_1}} \tag{4.12}$$

respectively. The implementation of the exact solution of the BFM for the single gas and mixed gas permeation for 3-dimensional CFD simulation through the porous support is a complex numerical solution and requires high computational efforts. Reason is that a real microstructure has millions of cells, and each of these cells will have a partial pressure if the exact solution of the BFM would be employed for the description of the transport through it. The one-dimensional analytical simulation of the transport through the porous support using the exact solution in Mathematica takes approximately 30 seconds. This will increase greatly if one intends to make the same simulation in 3D using real microstructures. Therefore, a simplified modification of the BFM with negligible deviation from the outcome of the exact solution is desirable.

The description of the transport through the porous support by the BFM was considered using the exact solution and two simplifications with respect to the pressure profile inside the porous support, which is non-linear. The simplifications considered are i) surface constant pressure and ii) an averaged constant pressure.

4.2.2 BFM – Constant pressure configurations

In this pressure simplification, the pressure through the porous support is assumed to be constant. A constant pressure gradient was assumed through the porous support; in other words, the pressure gradient (∇P_i) of the diffusing specie in the BFM which is the driving force for the transport is assumed to have a linear behaviour. Two simplifications with respect to the pressure profile inside the support were considered. This constant pressure simplification is subdivided into: surface constant pressure and averaged constant pressure.

4.2.2.1 Surface constant pressure

In this simplification, the pressure of the free surface of the porous support is assumed to be constant through the porous support. The pressure is dependent on the orientation of the porous support. If the support is at the feed side, the feed pressure is assumed to be constant through the porous support. Similarly, if the support is at the permeate side, the permeate pressure is assumed to be constant through the porous support. This simplification is graphically shown in Figure 4.2.

4.2. Different pressure simplifications of the BFM on flux

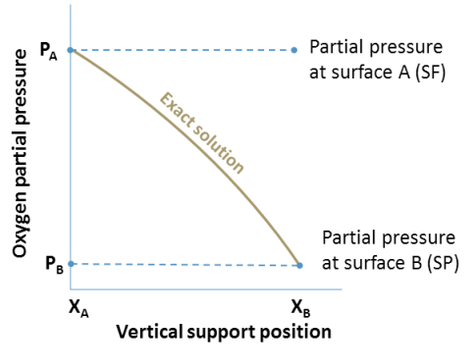

Figure 4.2: The plot of the exact solution and the surface constant pressure simplification. For the exact solution, P_A and P_B denote the feed and interface or interface and permeate pressure for when the support is at the feed or permeate side, respectively. Whereas for the surface constant pressure simplification, P_A or P_B denote the surface pressure of the diffusing specie when the support is at the feed (SF) or permeate side (SP), respectively, and this is assumed constant through the support.

Figure 4.2 shows the pressure profile through the support for the surface constant pressure simplification. For the evaluation of flux through the asymmetric membrane for this simplification, the single gas and mixed gas permeation equations are equal to Eq. (2.64) and Eq. (2.72), respectively. Significant errors in the flux can be expected as soon as a significant relative pressure drop occurs.

4.2.2.2 Averaged constant pressure

In this pressure simplification, the pressures on both sides of the porous support were averaged and assumed to be constant through the porous support. The feed and interface pressure or the interface and permeate pressure were averaged for the support at the feed side or permeate side, respectively.

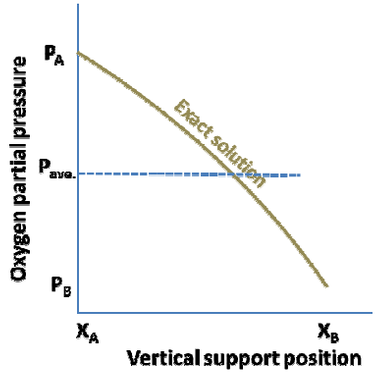

Figure 4.3: The plot of the exact solution and the averaged constant pressure simplification. For the exact solution, P_A and P_B denote the feed and interface or interface and permeate pressure of the diffusing specie when the support is at the feed or permeate side, respectively. Whereas for the averaged constant pressure simplification, the pressure through the support thickness was assumed to be the average of the pressures ($P_{ave.}$) on both surfaces of the porous support. P_A/P_B is the feed/interface pressure of the diffusing specie when the support is at the feed side (SF) or interface/permeate pressure (SP) when the support is the permeate side.

Depending on the position of the porous support P_A and P_B can either be feed and interface pressures or interface and permeate pressures, respectively, as can be seen in

Figure 4.3. These pressures (P_A and P_B) are to be averaged and assumed constant through the support. The single and mixed gas permeation equations for averaged constant pressure simplification are

$$N_g = -\frac{\nabla P_g}{RT}\frac{\varepsilon}{\kappa}D_g^K + \frac{B_o\frac{P_A+P_B}{2}}{\eta}, \tag{4.13}$$

and

$$N_1 = -\frac{\nabla P_1}{RT}\frac{1}{\frac{P_t-\left(\frac{P_{1A}-P_{1B}}{2}\right)}{\frac{\varepsilon}{\kappa}D_{12}P_t}+\frac{1}{\frac{\varepsilon}{\kappa}D_1^K+\frac{B_0P_t}{\eta_1}}}, \tag{4.14}$$

respectively. From the BFM equation for single gas permeation, the P_A and P_B are as explained in the graph. For mixed gas permeation equation where there exists more than one gas, P_{1A} and P_{1B} mean same as P_A and P_B for the diffusing specie of the mixture. The average pressure configuration will be equal to the exact solution if the flux is a linear function of the pressure. The more the pressure dependency is non-linear, the longer the deviation become.

4.3 Simulation procedure

Using Mathematica software (Wolfram Inc., Champaign IL, USA), the one-dimensional transport of the fluid through the overall membrane was modelled numerically. The BFM was used for the description of the transport through the porous support and the Wagner equation for the solid-state transport through the dense membrane. Continuity relation was assumed (i.e. the flux through the dense membrane equals that through the porous support) for the evaluation of the flux through the asymmetric membrane. The transport governing terms in the binary friction model are shown in Table 4.2.

Table 4.2: The transport governing terms of the BFM in Eq (2.72).

Binary diffusion		**Knudsen diffusion**		**Viscous flow**
$\frac{P_j}{\frac{\varepsilon}{k}D_{ij}P_t}$;	$D_{ij}=\frac{10^{-3}T^{1.75}(\frac{1}{M_i}+\frac{1}{M_j})^{1/2}}{P[(\sum V_i)^{\frac{1}{3}}+(\sum V_j)^{\frac{1}{3}}]^2}$ [128]	$\frac{\varepsilon}{k}D_g^K$;	$D_g^K=\frac{d_{pore}}{3}\sqrt{\frac{8K_BT}{\pi M_g}}$	$\frac{B_oP_g}{\eta_g}$ $B_o \propto d_{pore}^2$

The continuum condition requires that the flux through the thin dense membrane, by solving the modified Wagner equation (Eq. 2.27), should equal the flux through the porous support, by solving the BFM for single gas permeation using Eq. (2.64), (or the approximated variants Eq. (4.8) and (4.13)) depending on the pressure profile employed. Similarly, for mixed gas permeation, Eq. (2.27) should equal Eq. (2.72) , (or the approximated variants Eq. (4.8), and (4.14)). The BFM for the single or mixed gas permeation were used accordingly for the 3-end mode or the 4-end mode transport processes, respectively.

4.3. Simulation procedure

The Table 4.3 shows the permeation equation for the BFM that was employed for the simulation of the transport through the porous support, as well as considering the feed gas, transport processes, and the position configurations of the porous support.

Table 4.3: The permeation equations used for the description of the transport through the porous support for the transport processes depending on the feed gas. N/A means not applicable

Transport process	**Feed gas**	**Transport equations (BFM) - porous support**	
		Single gas permeation (Eq. (2.64))	Mixed gas permeation (Eq. (2.72))
3-end mode	O_2	Irrespective of support position	N/A
	Air	Support at the permeate side	Support at the feed side
4-end mode	O_2	Support at the feed side	Support at the permeate side
	Air	N/A	Irrespective of support position

The characteristic thickness, L_c, was determined and by minimizing the squared deviation (χ^2) between model and experiment

$$\chi^2 = \sum \left[\frac{N_{O_2}^{mod}(L_i) - N_{O_2}^{exp}(L_i)}{N_{O_2}^{exp}} \right]^2 \tag{4.15}$$

where $N_{O_2}^{mod}(L_i)$ and $N_{O_2}^{exp}(L_i)$ are, respectively, the modelled and experimentally observed flux with respect to membrane thickness, L_i. The total pressures P_{tperm}, and P_{tfeed} were taken to be constant at 1000 mbar.

ANSYS Fluent [129], a Computational fluid dynamic software package, is used extensively for 2-D and 3-D fluid flow simulation. In the present work, ANSYS Fluent was used for the 3D CFD simulation of the convective flow through the porous support (see section 5.6). This is to investigate the effect of pore morphology on the transport through the porous support. The reconstructed 3D structure of the acquired computer tomography data (see section 3.3) of the membrane supports were employed for the simulation. After the 3D reconstruction, the structures were inverted in other to mesh the pore volume for the transport simulation in ANSYS fluent. The 3D reconstruction, inversion and meshing of the structure file for use in ANSYS Fluent was done using Geodict software. Afterwards, the exported meshed file was imported into ANSYS Fluent for the CFD simulation. An in-built viscous (laminar) flow model was used for the simulation. In addition, the flow is symmetric in the tangential direction of flow and periodic in the direction of the flow. Air was used as feed gas and at an operating temperature of 900°C. The flow velocity of the sweep gas was assumed to be 4m/s. For the walls, the no-slip condition was assumed.

5. Results and discussions

5.1 Sample parameter evaluation

5.1.1 As received sample parameter – permeation measurement

5.1.1.1 $Ba_{0.5}Sr_{0.5}Co_{0.8}Fe_{0.2}O_{3-\delta}$ (BSCF)

Asymmetric membranes with a porous support thickness of 0.9 mm and dense membrane thicknesses of 20 and 70 µm, respectively, were obtained using the BSCF powder. The considered support corresponds to the C30 support in [95], prepared with 30wt.% corn starch as the pore former, yielding an average sintered porosity of 43%. In addition, from permeation measurements, the as received pore opening diameter of the TC porous support is 5.3 µm. Dense bulk membranes with four different thicknesses (Table 5.1) were also fabricated showing the effect of reducing membrane thickness. Permeation measurements as was explained in section 3.2 were carried out on the samples. Table 5.1 summarizes the measured flux and some operating conditions that would be used later for the analytical study of the transport through the porous support of an asymmetric membrane.

Table 5.1: Average permeation data and oxygen partial pressure for different membrane thicknesses obtained experimentally at 900°C with the support at the feed side using Ar (50 – 300 ml/min) as sweep gas [95, 119]. Here, L denotes the membrane thickness, N_{O2} the flux, P_{O2}' and P_{O2}'' the partial pressures at the feed and permeate side, and correspond to N_1 and P_1', P_1'' in the equation that was subsequently derived in section 2.4.

L (µm)	*O_2 as feed*			*Air as feed*		
	N_{O2} (ml cm^{-2} min^{-1})	P_{O2}' (mbar)	P_{O2}'' (mbar)	N_{O2} (ml cm^{-2} min^{-1})	P_{O2}' (mbar)	P_{O2}'' (mbar)
2500 bulk	1.8	1000	20			
2000 bulk	2.2	1000	24			
1000 bulk	3.2	1000	40			
500 bulk	5.9	1000	61			
70 with support	18.5	1000	179			
20 with support	21.8	1000	217	3.3	200	41.5

5.1.1.2 $Ba_{0.5}Sr_{0.5}(Co_{0.8}Fe_{0.2})_{0.97}Zr_{0.03}O_{3-\delta}$ (BSCF3Zr)

Similar to the BSCF powders, asymmetric membranes were also fabricated from two different processing routes (freeze casting and tape casting) using the BSCF3Zr powder. The different fabrication methods yielded asymmetric membranes with different support microstructures (see section 3.1). The porous supports of these asymmetric membranes were processed to have a comparable porosity, in other to be able to compare the effect of the different fabrication route on oxygen permeation through the asymmetric membrane. 40.5 % pore former (corn starch) was used for the TC structure in other to achieve similar porosity with the FC structure.

The geometrical parameter of the manufactured TC and FC samples is as stipulated in Table 5.2.

Table 5.2: The operating parameter from the permeation measurement of tape cast and freeze cast asymmetric membrane at a constant temperature of 900°C. The values are the average of the value obtained by varying the flow rate of the sweep gas for the configuration with the support on the feed side.

		P_{O2}' (mbar)	P_{O2}'' (mbar)	N_{O2} (ml/min cm²)	$L_{mem.\ Layer}$ [µm]	$L_{support}$ [µm]	ε (%)
Tape cast	O_2	1000	212	26	22-24	1000	45.5 ± 1.8
	Air	200	41	4			
Freeze cast	O_2	1000	217	25	22-24	990	45.5 ± 5.5
	Air	200	40	4			

The ambipolar conductivity of the dense BSCF membrane was calculated to be 123.3 S/m by fitting the Wagner equation (Eq. 2.21) to the four oxygen flux values for the thick bulk membrane in Table 5.1, where the effect due to surface exchange reactions can be neglected. The ambipolar conductivity for the two materials is comparable for the same operating conditions. As such the ambipolar conductivity is taken to be 123.3 S/m for all structures considered, irrespective of the membrane material used or the fabrication route.

5.2 3D reconstruction of the XCT data

The as-received CT data were imported into the Geodict 2017, a virtual material laboratory for reconstructing the three-dimensional geometry, and also for the evaluation of the geometrical parameters of the different porous support of the asymmetric membranes.

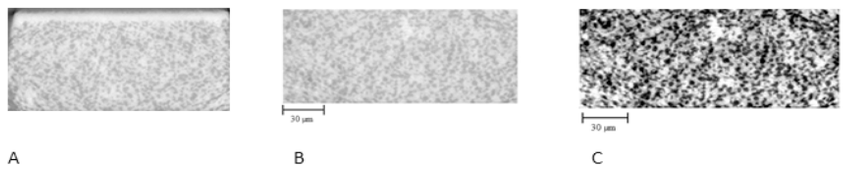

Figure 5.1: Shows (A) the image of the as received µCT data, (B) a slice before image enhancement, and (C) the slice after Image enhancement.

Prior to reconstructing the three-dimensional geometry of the BSCF by binarization with the virtual material laboratory, the images were deshaded. This was by enhancing the cropped tiff file (Figure 5.1) for better differentiation between pores and solid part. Figure 5.2 shows the 2D and 3D representation of the reconstructed BSCF tape cast structure. The pores are depicted in white colour while the solid part is in brown.

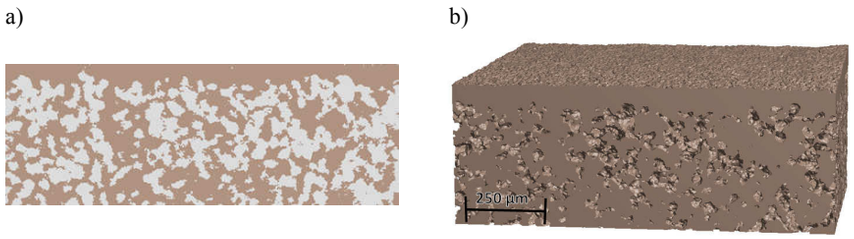

Figure 5.2: Shows (a) the 2D, and (b) the 3D view of the reconstructed tape cast structure manufactured with BSCF material. The lighter colours are the pores while the brown colour depicts the solid part of the asymmetric membrane.

No image enhancement was necessary for the µXCT samples (TC and FC) acquired from the membranes processed from BSCF3Zr. The reconstructed 2D and 3D image of the BSCF3Zr freeze cast and tape cast sample are as shown in Figure 5.3 and Figure 5.4.

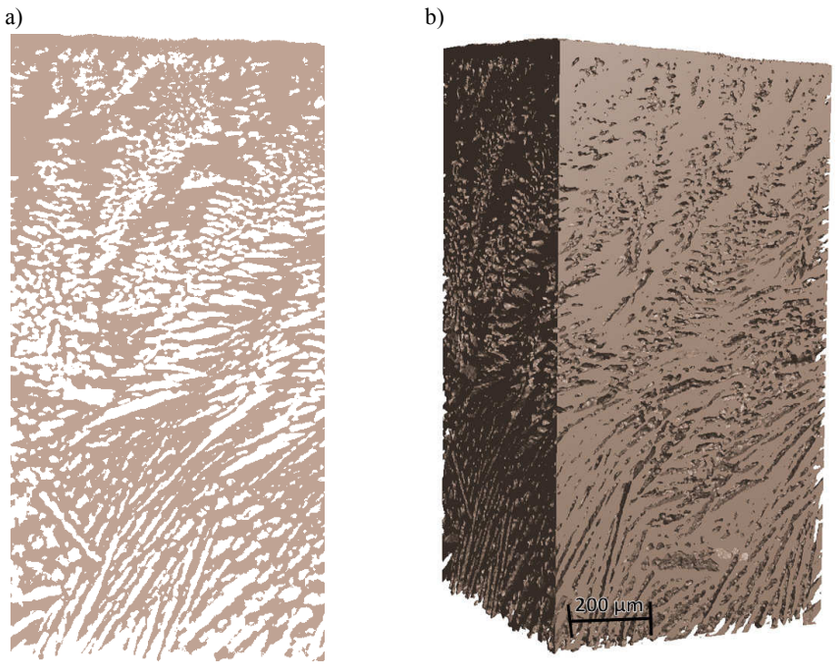

Figure 5.3: The reconstructed freeze cast sample in a) 2D and b) 3D using the acquired computed tomography data. The lighter colours are the pores while the brown colour depicts the solid part of the asymmetric membrane.

5.2. 3D reconstruction of the XCT data

a) b)

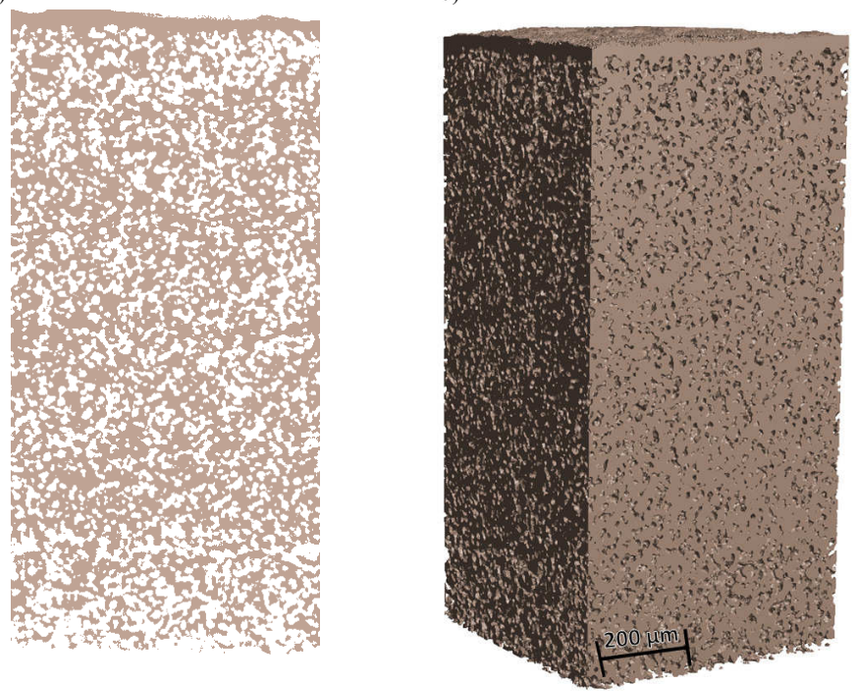

Figure 5.4: The reconstructed sequential tape cast sample in a) 2D and b) 3D using the acquired computed tomography data. The lighter colours (white) are the pores while the dark colour (brown) depicts the solid part of the asymmetric.

a) b)

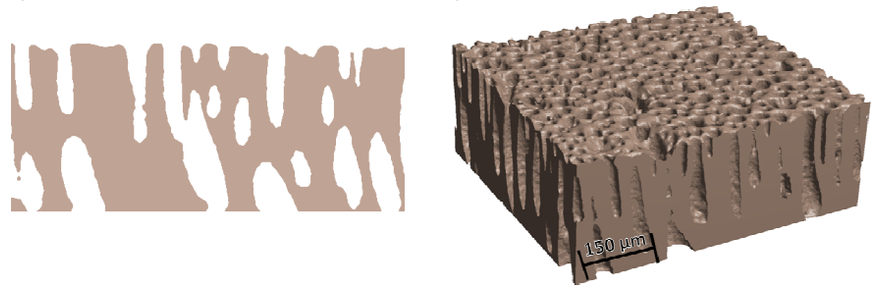

Figure 5.5: The reconstructed inverse tape cast sample in a) 2D and b) 3D using the acquired computed tomography data. The lighter colours (white) are the pores while the dark colour (brown) depicts the solid part of the asymmetric membrane.

After the 3D reconstruction of the µXCT 2D slices/images, the dense membrane was cropped off from the porous substrate as only the geometrical/structural parameters of the porous support such as permeability, tortuosity factor, porosity, and the average pore opening diameter need to be evaluated. These parameters, in addition to the data in Table 5.1 and Table 5.2,

were taken as input data for the analytical simulation of the transport through an asymmetric membrane using the transport model presented in section 2.2.1. The support side in contact with the membrane will be referred to as support/membrane interface while the other surface will be referred to as the free surface. The support/membrane interface will be used as the feed side and the free surface as the permeate side for the evaluation of the structural parameters.

5.3 Computation/Evaluation of the geometrical parameters

After the 3D reconstruction of the XCT data, the average geometrical parameters for the structures considered were evaluated. Similar procedures were employed for the simulation of the geometrical parameters irrespective of fabrication route or membrane material used. Other geometrical information like the percentage of the open and closed pores, surface area, and etc. were also evaluated. This will aid the understanding of the behaviour of the porous support during transport simulation. The effect of the support microstructure for TC and FC samples manufactured form BSCF3Zr were compared in section 5.7. Hence, porous support of the TC and the FC were sectioned into 4 and 12 layers, respectively. The geometrical parameters evaluated for the sectioned layers of the TC and FC will be presented in this section, but further discussions will be in section 5.7.

The evaluated geometrical parameters obtained from the tape cast BSCF sample in this section, in addition to the input data from section 5.1.1.1 were used for the simulations studies in sections 5.4 and 5.5. Similarly, the geometrical parameters from the BSCF3Zr in addition to the input data from section 5.1.1.2 were used for the simulations studies in section 5.7 and partly with the geometrical parameters of the inverse tape cast for section 5.8.

5.3.1 Flow simulation

After the flow simulation, the streamline of the transported species through the porous support is as shown in Figure 5.6. The colour of the streamline shows the relative pressure of the flow. Some part of the porous support was clipped off in other to view the flow paths of the fluid through the porous structure.

The permeability, B_0, for the tape cast sample fabricated from BSCF material was evaluated to be 3.09×10^{-13} m^{-2}. Similarly, for the tape cast and freeze cast fabricated from BSCF3Zr, B_0 was evaluated to be 2.22×10^{-13} and 2.68×10^{-13} m^{-2}, respectively. The permeability of the inverse tape cast sample was also evaluated to be 2.61×10^{-11} m^{-2}. The evaluated permeability values for the different structures considered are of the same other of magnitude and is similar with carbonate oil reservoir rocks with comparable porosities and pore sizes [130].

5.3. Computation/Evaluation of the geometrical parameters

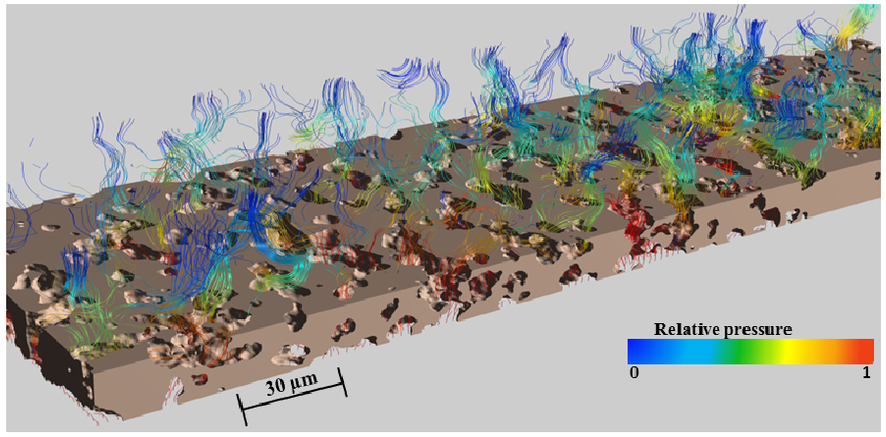

Figure 5.6: The porous support showing the relative pressure after a flow simulation through a tape cast porous structure.

The evaluated permeability, B_0, for the sectioned layers of the tape cast and the freeze cast sample fabricated from BSCF3Zr are summarized in Table 5.3.

Table 5.3: The evaluated permeability values on sectioned layers for (a) the freeze cast and (b) the tape cast substrates fabricated from BSCF3Zr.

a)

Layer	**1**	**2**	**3**	**4**	**5**	**6**	**7**	**8**	**9**	**10**	**11**	**12**
Permeability, (B_0) (m^2) $\times 10^{-13}$	17.3	8.99	8.07	8.86	8.22	6.49	5.06	3.96	3.09	2.14	1.38	1.20

b)

Layer	**1**	**2**	**3**	**4**
Permeability, (B_0) (m^2) $\times 10^{-13}$	2.72	1.86	1.99	2.87

5.3.2 Diffusion simulation

Figure 5.7 shows the concentration gradient across the porous supports after the diffusion simulation as was explained in section 4.1.1 and using the boundary conditions stipulated in section 4.1.4. The colour of the concentration gradient along the structures depicts the variations of the effective diffusivity across the structure. This behaviour is more uniform for the tape cast substrate (Figure 5.7.b) than for the freeze cast substrate (Figure 5.7a), as the latter exhibits a graded structure.

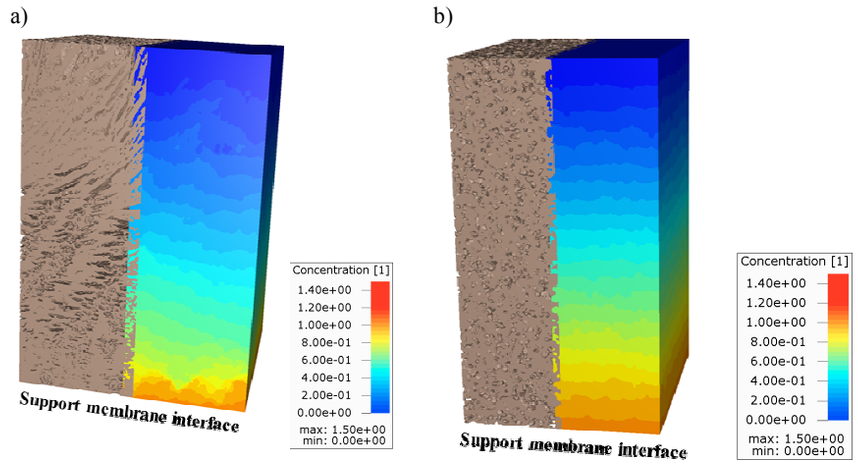

Figure 5.7: Showing the concentration gradient across (a) the freeze cast and (b) the tape cast porous support, respectively.

Around the nucleation zone for the freeze cast structure (Figure 5.7.a), the effective diffusivity here is higher and reduces ($k \rightarrow 1$) towards the air surface. As a result, it shows that the tortuous nature of the freeze cast structure decreases across the FC structure from membrane-support interface to the free surface. On the other hand, this variation in effective diffusivity is seen to be uniform across the TC structure (Figure 5.7.b), depicting uniformity in the tortuous nature of the flow path. The average tortuosity factor for the TC irrespective of the material used was 2.9, while the FC was 3.3. For the inverse tape cast sample, the tortuosity factor was evaluated to be 1.75, and it had a porosity of 35%.

The evaluated tortuosity factor, k, and the porosity, ε , for the sectioned layers of the tape cast and the freeze cast sample fabricated from BSCF3Zr are summarized in Table 5.4.

Table 5.4: The evaluated tortuosity factor (k), and porosity (ε) on sectioned layers for (a) the freeze cast and (b) the tape cast substrates fabricated from BSCF3Zr.

a)

Layer	**1**	**2**	**3**	**4**	**5**	**6**	**7**	**8**	**9**	**10**	**11**	**12**
(*k*)	1.44	1.73	2.2	2.46	2.72	2.94	3.02	3.09	3.15	3.29	3.48	3.46
(ε) (%)	55.36	43.32	44.06	47.84	49.37	49.23	49.67	47.93	45.89	41.55	35.52	29.3

b)

Layer	**1**	**2**	**3**	**4**
(*k*)	2.52	2.85	2.79	2.48
(ε) (%)	48.34	42.53	43.24	46.58

5.3.3 Pore simulation

After the porosimetry evaluation (see section 4.1.2) of the FC, TC (BSCF3Zr), and TC (BSCF) structure, the D_{50} was 6.8, 5.0, and 6.5 µm, respectively. Similarly, the D_{50} for the inverse tape cast sample was evaluated to be 66.0µm. These evaluated average pore diameters are the pore throat diameter. In addition, the connectivity of the pores was investigated by evaluating the percentages of the closed and open pores for the structures. For the TC and the FC structures, the percentage of the closed pores was evaluated to be 0.04 and 0.09 % respectively. As such, both porous supports (freeze cast and tape cast structures) have less than 0.1 % closed pores, and this shows that the pores are well connected with less blocked pores or islands.

The evaluated average pore opening diameter, D_{50}, for the sectioned layers of the tape cast and the freeze cast sample fabricated from BSCF3Zr are summarized in Table 5.5.

Table 5.5: The average pore opening diameter, D_{50}, of the sectioned layers for (a) the freeze cast and (b) the tape cast substrates fabricated from BSCF3Zr.

a)

Layer	**1**	**2**	**3**	**4**	**5**	**6**	**7**	**8**	**9**	**10**	**11**	**12**
D_{50} (µm)	8.4	7.0	7.93	10.0	9.7	9.0	8.3	7.6	6.8	6.0	5.0	4.4

b)

Layer	**1**	**2**	**3**	**4**
D_{50} (µm)	8.4	7.0	7.93	10.0

5.4 Evaluation of the characteristic thickness, L_c

The characteristic thickness/length L_c, was evaluated according to Eq. (4.15) to be 28 µm using experimental flux data obtained at 900°C with oxygen as feed gas and argon as sweep gas (Table 5.1). This is comparable to the value obtained in [95], where the $\frac{2L_c}{\beta}$ was predicted to be 44 µm by using a least square fit of the measured data, with a correction factor, ß, which was 0.874. With the assumption that the membrane-support interface pressure was equal to the feed pressure, the support effect was neglected while fitting the L_c in Ref. [95]. In the present work, using the same operating conditions as in [95], the membrane-support interface pressure, with the support on the feed side, was evaluated to be approximately 940 mbar with a feed pressure of 1000 mbar.

Figure 5.8 shows a comparison of the simulated and the experimental plot of the flux at varying bulk and asymmetric membrane thickness. The membranes with a thickness of 500 µm or larger shown in the plot were bulk membrane only. The 20 and 70 µm thick membranes are supported by a 0.9 mm thick porous support. Using the analytical model, the experimental behaviour from [95] was reproduced. At a membrane thickness of 20 µm, the analytically ob-

tained flux was ~7% higher than the experimentally observed flux, whilst the 70 µm thick membrane yielded a decrease in flux of ~17%.

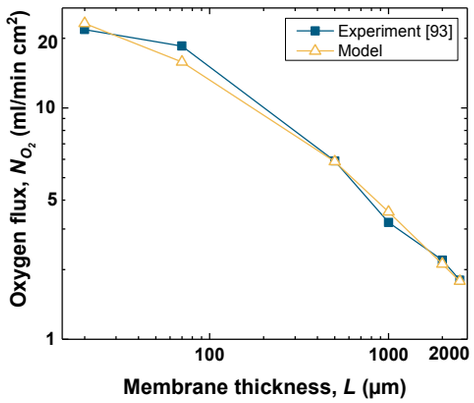

Figure 5.8: The dependence of the oxygen permeation rate on the membrane thickness, with support thickness of 0.9 mm for asymmetric membranes (with 20 and 70 µm thick dense membrane), all others: bulk membrane. Oxygen was used as feed gas at an operating temperature of 900°C with the support at the feed side. The operating pressure is as stipulated in Table 5.1.

5.5 Effect of variation in support geometry on flux

5.5.1 Effect of the support pore diameter

The geometry of the 3D tape cast structure was scaled isotropically to vary the pore diameter from 1 – 50 µm.

Figure 5.9 presents the evaluated permeability as a function of the varied pore diameter. The pore diameter in the present work is referred to the average throat diameter of the porous structure.

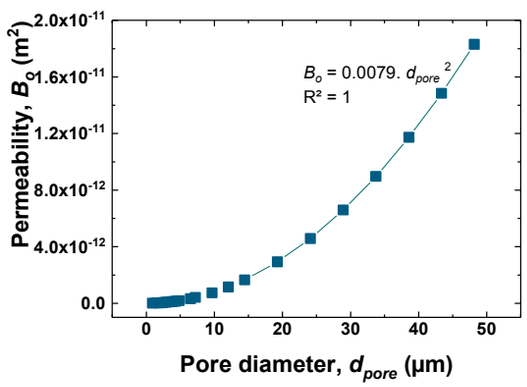

Figure 5.9: The permeability, B_o (used as input parameter for the evaluation of the BFM) of the porous support as a function of the pore diameter.

5.5. Effect of variation in support geometry on flux

According to Hagen Poiseuille, the flow rate scales with the fourth exponent of the cylinder diameter and scales with the square of the pore diameter with respect to multiple cylinders. This plot (Figure 5.9) reflects the behaviour according to Hagen Poiseuille and cylinder density, where the permeability scales with the square of the pore diameter. The bulk gas diffusivity and the tortuous nature of the sample did not change while scaling the pore diameter; because the porosity was kept constant.

The effect of varying the pore diameter of the porous support on the flux through an asymmetric membrane was evaluated. Irrespective of the feed gas used, the same transport model and similar operating conditions were used to model the transport through the porous support for the 3-end mode and 4-end mode transport processes with the support at the feed side (SF). Support at the feed and permeate side will be represented by SF and SP, respectively.

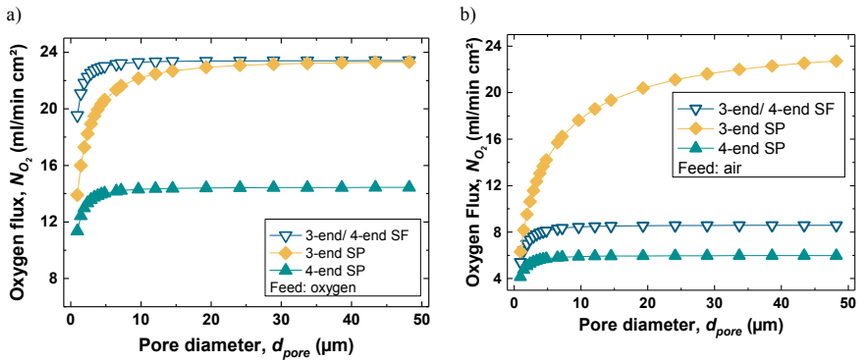

Figure 5.10: Calculated oxygen permeation rate at varying pore diameter, using (a) oxygen and (b) air as feed gas on a 20 µm thick supported membrane, and considering the 3-end mode and the 4-end mode transport processes, respectively. SF and SP indicate support at the feed and permeate side, respectively. The operating pressure is as stipulated in Table 5.1.

Figure 5.10 shows the relationship between the pore diameter and the flux using oxygen and air as feed gas. For O_2 as feed gas, increasing the pore diameter above 30 µm for the 3-end / 4-end mode of transport with support at the feed side and 3-end mode with the support at the permeate side, produced no further increase in the flux (Figure 5.10.a). Similarly, increasing the pore diameter above 10 µm for the 4-end mode with the support at the permeate side also yielded no further increase in flux. At larger pore diameters (>35 µm) for the 3-end mode of transport, the position of the porous support does not have any effect on the flux, which is not the case for the 4-end mode (Figure 5.10.a). This is attributed to the membrane dominating the transport for 3-end mode with large pore diameter, and the support being more rate-limiting for the 4-end mode.

Using air as feed gas (Figure 5.10.b), the position and pore diameter of the porous support affected the flux for the 3-end mode transport process unlike when oxygen was used as feed gas. Even at larger pore diameters, the flux observed with the support on the feed and permeate side were never equal or even comparable as was observed with oxygen as feed gas. Instead, the 3-end mode with the support on the feed side demonstrated behaviour similar to that of the

4-end mode. Whereas with the support at the permeate side, an increase in flux comparable to using oxygen as feed gas was observed for the 3-end mode. The influence of the support and the membrane irrespective of the support position for both transport processes are not negligible. It was also observed that no further increase in flux was observed by increasing the pore diameter above 10µm for mixed gas permeation. However, the flux through the asymmetric membrane increased with increasing support pore diameter. In Ref. [30], similar observation with respect to improvement in overall flux with increase in the support pore diameter has been observed. Schulze-Küppers *et al.* have compared the effect of using different pore formers to increase porosity of the asymmetric membrane. However, not only the porosity improved, the pore size was also increased and could also contribute to the improvement in flux that they observed. They did not quantify the improvement in flux with respect to the pore size, but this has been done in Figure 5.10.

5.5.1.1 Effect of transport terms in BFM (Viscous, Knudsen and binary diffusion term) on flux

To better understand why the flux for the mixed gas transport in the porous support did not increase further above 10 µm pore diameter as was shown in section 5.5.1, the effect of the viscous, Knudsen, and the binary diffusion term of the BFM was evaluated. This was to identify which of the terms and at what conditions they are dominating or negligible for the transport processes.

With the support at the permeate side and using oxygen as feed gas, the flux obtained was lower than when the support was at the feed side. This is due to the pressure in the viscous term of the BFM which is dependent on the position of the porous support. It is higher or lower with the support on the feed or permeate side, respectively, and this invariably affects the flux. The Knudsen and the viscous term in the BFM equation are pore-size dependent. An in-

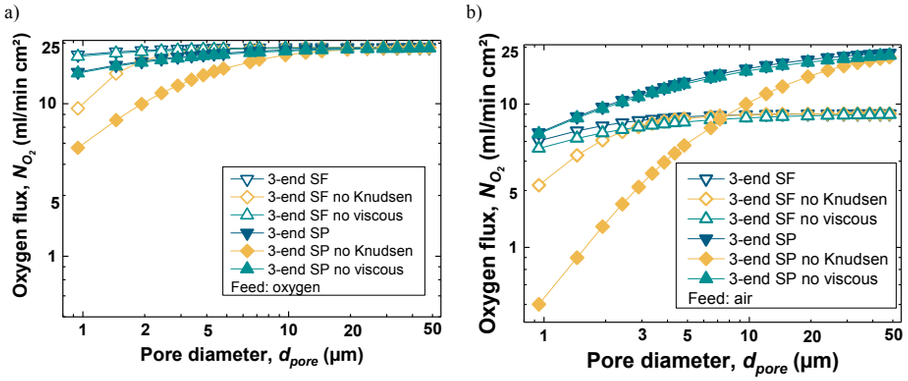

Figure 5.11: The flux of oxygen at varying pore diameter, switching off either the viscous or the Knudsen term in the binary friction model to ascertain their effects on the transport through the asymmetric membrane. For the 3-end mode of transport, with (a) oxygen as feed gas, and (b) air as feed gas. SF and SP indicate support at the feed and permeate side, respectively. The operating pressure is as stipulated in Table 5.1.

crease in pore diameter increases both the Knudsen diffusion and the permeability and, consequently, the overall flux. Irrespective of the feed gas used, the effect of the Knudsen term was more dominant with the support at the permeate side than at the feed side. Also, the effect of the viscous flow on the overall flux is minimal compared to Knudsen diffusion transport, although not negligible.

Using oxygen as feed gas (Figure 5.11.a) with the support at the feed or permeate side, the Knudsen term dominated for pore diameters below ~4.0 µm or 15 µm respectively; above this, both the viscous and the Knudsen term had a comparable effect on the flux. When air was used as feed gas (Figure 5.11.b), the Knudsen term dominated for pore diameters below 3.5 µm/~40 µm with the support at the feed/permeate side, respectively. When the pore diameter was greater than 30 µm, the effects of the support position, viscous and Knudsen term were minimal, although not negligible, except when air was used as feed gas with the support at the permeate side.

This can be understood by considering that the transport governing terms of the BFM (2.72) for mixed gas transport through the porous support are connected as shown in Figure 5.12.

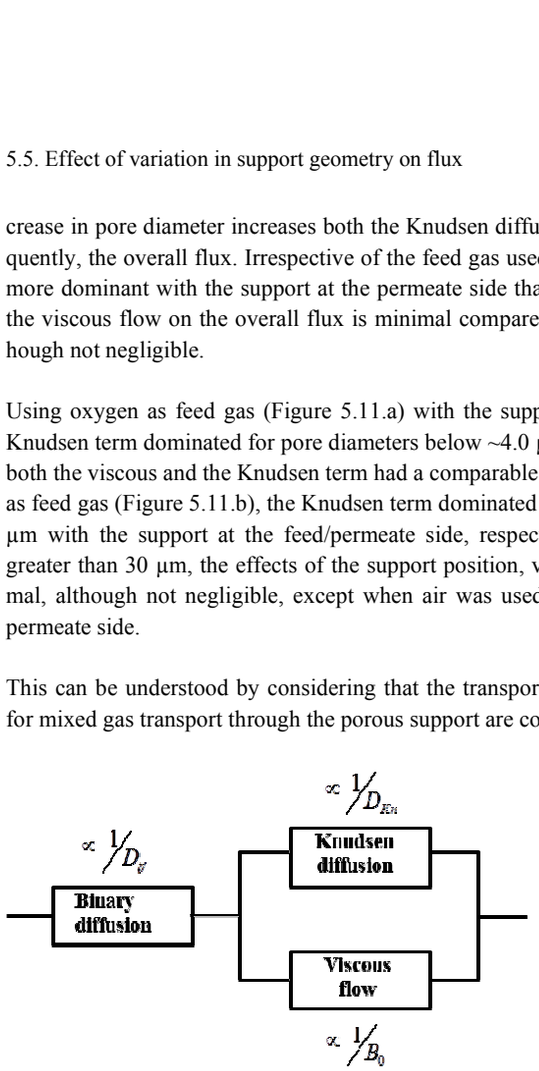

Figure 5.12: Shows that the binary diffusion term of the BFM (Eq. 2.72) is connected in series to the parallel connection between the Knudsen diffusion term and viscous term.

The binary diffusion term is connected in series to the sum of the Knudsen diffusion and the viscous flow term. Hence, for small pore diameters of the support microstructure, the contribution of the binary diffusion term is negligible compared to the sum of the contributions of the Knudsen diffusion and the viscous flow terms.

$$1/D_{ij} \ll 1/D_{Kn} + 1/B_0$$

As a result, the binary diffusion term is not the rate limiting term for the transport, rather, the transport term with the smaller contribution between $1/D_{Kn}$ and $1/B_0$ becomes the rate limiting term. In the present case with consideration to small pore support microstructure, the Knudsen term is rate limiting. This is because the permeability, B_0, of small pored support microstructure is small thereby making the contribution of the viscous flow term larger when compared to the contribution of the Knudsen diffusion, D_{Kn} with respect to small pored support microstructure.

Considering support microstructures with large pore diameters, the contribution of the binary diffusion term to the overall flow through the porous support is larger compared to the sum of the contributions of the viscous flow and Knudsen diffusion terms.

$$1/D_{ij} \gg 1/D_{Kn} + 1/B_0$$

In this case, the binary diffusion term becomes rate limiting. This explains the plateau observed for the mixed gas permeations (4-end mode SF & SP and 3-end mode SF) in Figure 5.10. This is because the numerical model for mixed gas permeation (Eq. 2.72) still describes the transport through the porous support as being governed by binary diffusion. This is not realistic for very large pores, where the sweep gas must be assumed to be able to flow. The effect of the microstructural geometry of the porous support on convective flow will be presented in section 5.6.

5.5.1.2 Conclusion

Irrespective of the transport mode considered, increasing the pore diameter of the porous support improved overall flux. However, increasing the pore diameter above 10 µm and 30 µm for mixed and single gas permeation transport yielded no further improvement on flux.
Knudsen diffusion term of the BFM is more rate-limiting for the transport through the porous support at lower pore diameter, while, the binary diffusion term becomes more rate-limiting for larger pore diameters. However, this is not realistic for large pore where convective flow is expected.

5.5.2 Effects of pore diameters on partial pressure/pressure drop

5.5.2.1 Interfacial pressure

Since the feed and the permeate pressures were known, the pressure drop at the support-membrane interface was evaluated. The interfacial pressure increased (tends $\rightarrow P_{O_2feed}$) for the 3-end / 4-end mode when the support is at the feed side with increasing pore diameter of the porous support by 22 or 28% using either air or oxygen as feed gas, respectively. For 3-end mode with the support at the permeate side, and using air or oxygen as feed gas, it reduced (tends $\rightarrow P_{O_2perm}$) by 65 or 46%, respectively. Similarly, for 4-end mode with the support at the permeate side, it also reduced (tends $\rightarrow P_{O_2perm}$) by 11% or 20% using either air or oxygen as feed gas. This occurs because of the reduced support effect when the pore diameter of the porous support increases. Therefore, the pressure drop across the dense membrane and the porous support was evaluated from the obtained interface pressure as shown in Figure 5.13.

5.5. Effect of variation in support geometry on flux

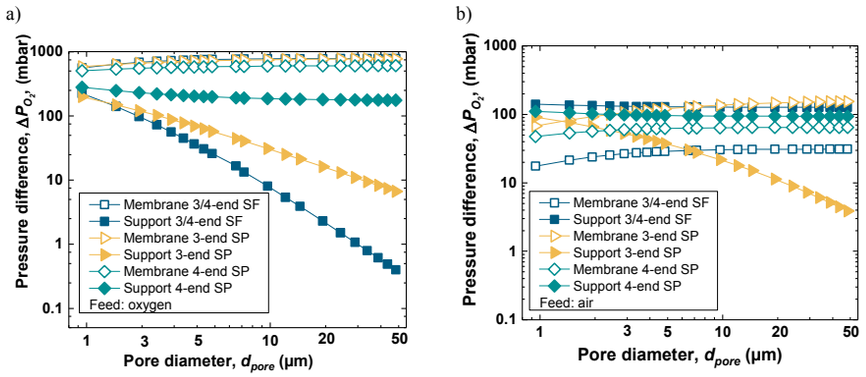

Figure 5.13: The pressure drops through the dense membrane and porous support for the 3-end and 4-end mode transport processes using (a) oxygen and (b) air as feed respectively. 3/4 – end indicates 3-end and 4-end mode, SF and SP indicate support at the feed and permeate side, respectively. The operating pressure is as stipulated in Table 5.1.

Irrespective of the support position for the 3-end mode, and using oxygen as feed gas (Figure 5.13.a), the pressure drop across the dense membrane increased as the pore diameter of the porous support is increased, and it reduced across the porous support. The greater pressure drop across the dense membrane demonstrates and confirms that the membrane dominates the transport, even though support effects exist. The rate-limiting effect of the porous support decreases with the decrease in pressure drop across the support and, consequently, increases flux. When the support is the permeate side (Figure 5.13.b), the pressure drop across the support for the 4-end mode transport process is higher than it is for other transport configurations.
This can be attributed to the effect of the binary diffusion in the porous support as explained using Figure 5.12.

When air is used as feed gas (Figure 5.13.b), the resistance of the support to flux for the 4-end mode, irrespective of support position, and the 3-end mode with the support at the feed side, is comparable to that of the membrane. This is can be attributed to the binary diffusion term in the BFM. Comparing Figure 5.10 with Figure 5.13 (which shows the dependence of the flux on the pore diameter), reveals that the lower the pressure drop through the support, the greater the observed flux.

5.5.2.2 Pressure profiles

Figure 5.14 shows the pressure profiles of the flow through the 20 μm thick supported membrane with the support on the permeate side, using oxygen (Figure 5.14.a) and air (Figure 5.14.b) as feed gas, and argon as sweep gas. The drop in pressure at the surfaces of the dense membrane reflects the limited surface exchange kinetics that has been considered by the introduction of the characteristic thickness, L_c, in Eq. (2.27). As no further data were available, both sides of the membrane were assumed to exhibit the same surface exchange kinetics.

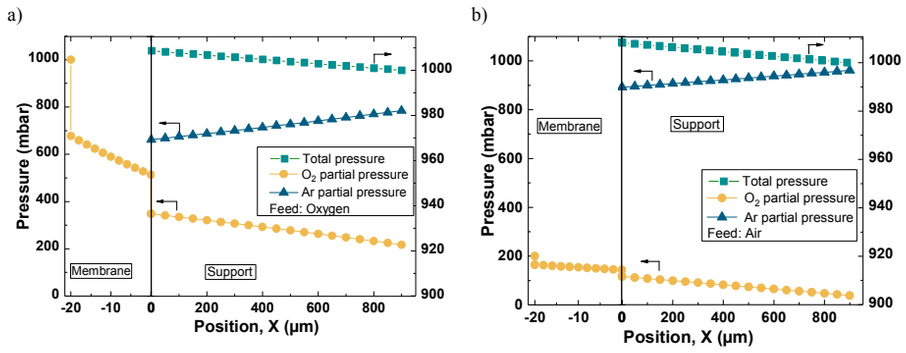

Figure 5.14: The total pressure gradient, argon and oxygen partial gradients across the supported membrane for the 4-end mode transport process with the membrane on the feed side using (a) oxygen and (b) air as feed gas, and argon as sweep gas. Please note the different scales for position X in the membrane and the support. The operating pressure is as stipulated in Table 5.1.

The oxygen partial pressure decreases across the porous support, while the argon partial pressure increases. Similar behavior was observed by H. Li *et al.* [20], where they investigated the concentration (which can be related to the pressure using the ideal gas relation) of oxygen and argon in the porous support. The total pressure P_t exhibits a slight gradient according to Eq. (4.8), otherwise there would be no total gas transport. Since there is no argon flux through the porous support, the argon partial pressure, P_{Ar}, describes the opposite gradient with respect to levelling the friction of transported oxygen.

5.5.2.3 Conclusion

The higher the pressure drop through the membrane or the porous support, the more the rate limiting effect and the lower the overall flux. Pressure profile across the porous support is not constant. This consequently shows that there is difference between the surface pressure and the pressure across the porous support. This will be considered in more detail in section 5.9 by comparing the effect of the different simplification of the pressure profiles across the support.

5.5.3 Effect of thickness and tortuosity factor of the porous support on flux

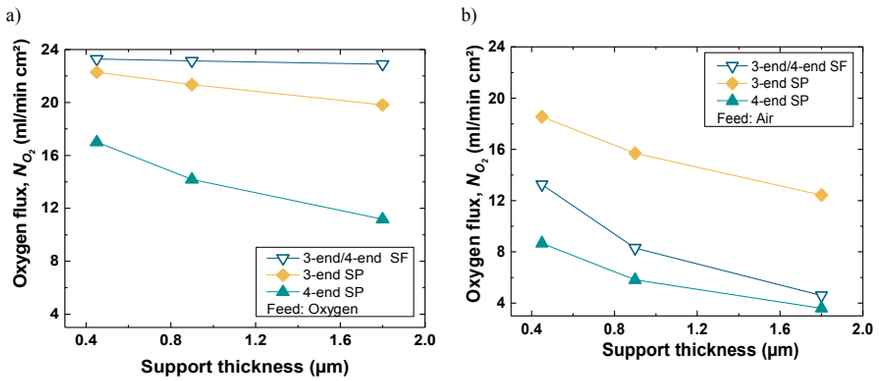

Figure 5.15: Effect of increasing or decreasing the thickness of the porous support using (a) oxygen and (b) air as feed gas for a porous support with 6.5 μm pore diameter and considering the 3-end mode and 4-end mode transport processes, respectively. SF and SP represent support at the feed and permeate side, respectively. The operating pressure is as stipulated in Table 5.1.

The effect of the support thickness was investigated by reducing / increasing the as received support thickness of 0.9 mm by a factor of 2. As shown from Figure 5.15, the flux increased/decreased with decrease/increase in support thickness. For the 3-end mode, with the support on the feed/permeate side and using oxygen as feed gas (Figure 5.15.a), the flux increased by ~0.2%/~2% when the thickness was reduced by a factor of 2 and reduced by 0.3%/~4% when it was increased by a factor of 2. The effect of increasing or decreasing the support thickness is more obvious for the 4-end mode transport process with the support at the permeate side. The flux increased by 15% when the thickness was reduced by a factor of 2 and decreased by 29% when it was increased by a factor of 2.

When air was used as feed gas (Figure 5.15.b), the flux with the support at the feed/permeate side for the 3-end mode increased by 39%/~12% when the thickness was reduced by a factor of 2 and decreased by 39%/15% when it was increased by a factor of 2. The 4-end mode with the support at the feed side and the 3-end mode with the support at the feed side behaved similarly. When the support was at the permeate side, for the 4-end mode, the flux increased by ~40% when the thickness was reduced by a factor of 2 and decreased by 34% when the thickness was increased by a factor of 2. The trend in Figure 5.15 can be compared to the experimental observation according to Chang *et al.* [131] using air and helium as feed and sweep gas, respectively, at 1223 K. They have observed an increase in flux with increasing support thickness (0.5×10^{-13} m, 0.9×10^{-13} m, and 1.3×10^{-13} m). In addition, Chang *et al.* have also considered the asymmetric membrane assembly with the support at the feed and permeate side, and observed that the flux with the support at the feed side was higher than with the support at the permeate side as have been shown in the present work. The effect of varying the support thickness was further investigated by varying in addition the pore diameter of the porous support, as shown in Figure 5.16.

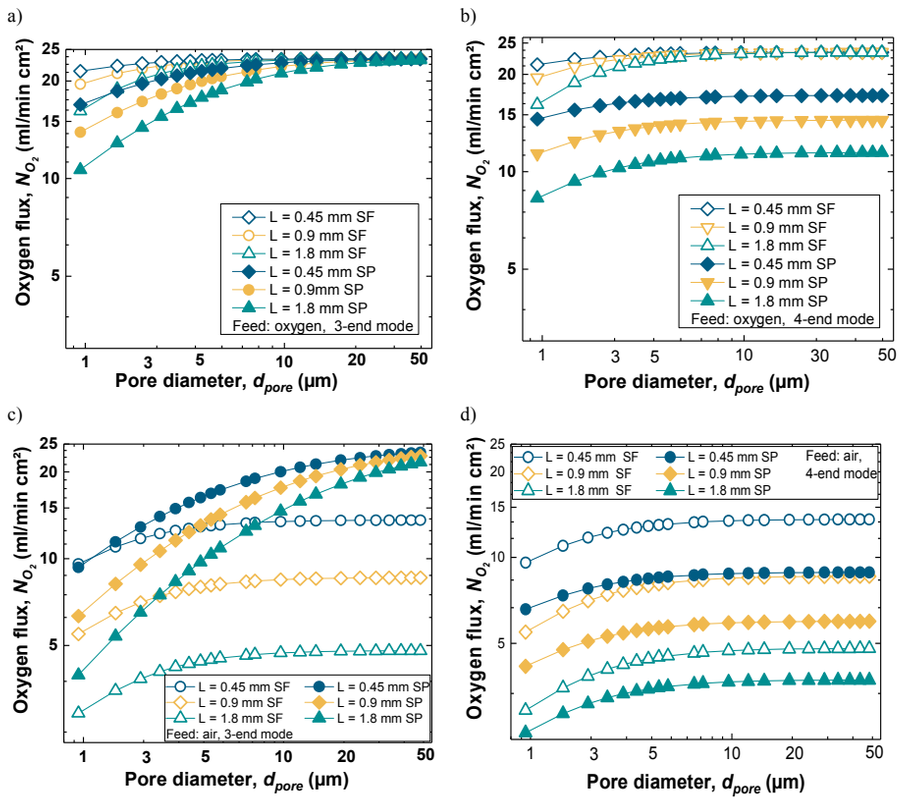

Figure 5.16: Effect of varying support thickness and pore diameter on the flux through an asymmetric membrane for the (a) 3-end mode and (b) 4-end mode transport process, using oxygen as feed gas, (c and d) 3-end and 4-end mode transport process using air as feed gas. *L* is the thickness of the porous support. SF and SP represent support at the feed and permeate side, respectively. The operating pressure is as stipulated in Table 5.1.

For the single gas permeation transport (see Table 4.3) through the porous support, the effect of support position and thickness was evident for smaller pore diameters (< 15µm) irrespective of the transport mode or feed gas used (Figure 5.16.a, b, and c). This can be attributed to the fact that the Knudsen diffusion term of the BFM becomes more rate limiting for smaller pore diameters of the porous support. Wheras for mixed gas permeation transport (Table 4.3), the effect of support position and thickness is more evident for smaller pore diameters (< 15µm) and plateaus out for larger pore diameters (Figure 5.16.b, c, and d). this can be attributed to the explanation of Figure 5.12.

For the 3-end mode and using oxygen as feed gas (Figure 5.16.a), the position, thickness, and pore diameter of the porous support did not affect the flux for pore diameters above 35 µm. The same observation was made when using oxygen as feed gas for the 4-end mode with the support at the feed side (Figure 5.16.b), but when the support was at the permeate side, both the position and the thickness of the support affected the flux. Observations similar to the latter were made for 3-end mode with the support on the feed side and 4-end mode (irrespective of

support position, using air as feed gas). Therefore, for the optimisation of the support, there is a need for a graded layer system (whereby most part of the support geometry will be coarse). This will be further studied in section 5.8.

The relative flux was obtained by comparing the simulated flux from the modified Wagner (2.27) when only the unsupported 20 µm thick dense membrane was used and the flux (from Wagner + BFM) with the supported membrane. This evaluation was also done considering different geometry combinations of the porous support. Assuming the same operating conditions (pressure gradient, temperature, etc.) for the choosen configuration, the flux through the unsupported membrane was simulated to yield approximately 24 ml/min cm². This is the expected flux from the dense membrane without the influence of the porous support. The relative flux was investigated for the 4-end mode transport process with the support at the feed side using air as feed gas. This is because the mixed gas permeation transport shows more support limiting effect on the observed flux. The relative flux with respect to the unsupported membrane flux was obtained using the relation

$$\text{Re}lative\ flux = \frac{supported\ membrane\ flux}{unsupported\ membrane\ flux} \times 100$$

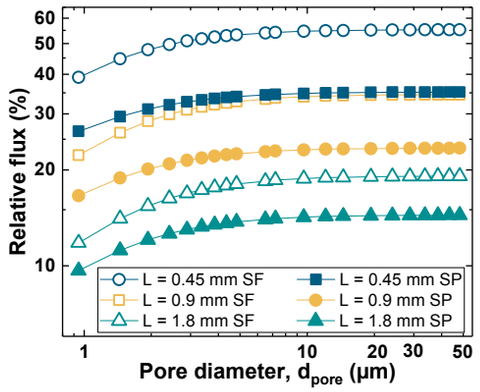

Figure 5.17: The relative flux with respect to the unsupported membrane flux as a function of the pore diameter for the 4-end mode transport process at varying support thickness. The operating pressure is as stipulated in Table 5.1.

The relative flux with respect to the unsupported membrane flux is presented in Figure 5.17. The as-received support thickness of 0.9 mm within the pore diameter range considered yields only 23-30% and 17-19.5 % of the theoretical possible flux with the support at the feed side and permeate side, respectively. Decreasing the thickness of the support while increasing the d_{pore}, reduces the rate limiting effect of the support on flux. This in turn increases the dominance of the dense membrane on flux. The limitation in the flux for mixed gas permeation transport in the porous support can be attributed to the flux of the sweep gas (Ar) at the permeate side or to the retentate (N_2) when the support is at the feed side. Mixed gas transport occur for 4-end mode irrespective of support position using air as feed gas and argon as sweep gas, and for 3-end mode with support at the feed side using air as feed gas. Because only oxygen flows through the dense membrane, nitrogen or argon are accumulated, but they can

diffuse through the porous support. This hinders the flux of oxygen diffusing through the porous support.

Amongst the three terms of the BFM (viscous flow, binary and Knudsen diffusion), only the binary diffusion term does not scale with the pore diameter. The Knudsen diffusion scales linearly with pore diameter and the viscous flow scales with square of the pore diameter (permeability). The porosity and the tortuosity factor are the geometrical parameters affecting the binary diffusion term. This explains why no further increase in flux was observed in Figure 5.17 with increasing pore diameter above 10 µm. Therefore, the relative flux was also considered numerically as a function of the tortuosity factor of the porous support (Figure 5.18), while the membrane thickness of 0.9 mm and a pore diameter of 6.5 µm were kept constant.

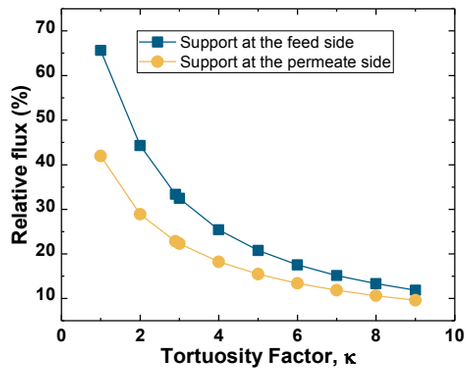

Figure 5.18: The relative flux with respect to the unsupported membrane flux as a function of the tortuosity factor for the 4-end mode transport process at a support thickness 0.9 mm. The operating pressure is as stipulated in Table 5.1.

Irrespective of support position, the flux increased as the tortuosity factor [125] approaches unity (Figure 5.18). The configuration with the support on the feed side was more favourable than the support at the permeate side. For the 4-end mode transport with the support on the feed, the theoretical possible flux increased from ~10-42% for the range of tortuosity values considered. Similarly, when the support is at the permeate side, the flux increased from ~12-65%. Very small tortuosity factor values ($k \rightarrow 1$) mean channel-like pores (freeze cast or inverse tape cast) [24, 28].

The effect of the thickness and pore diameter of the porous support was further investigated by assuming that the highest flux obtained for the 3-end mode, using air as feed gas, was membrane-dominated. Furthermore, 10% of this flux was assumed to be an acceptable loss due to the influence of the support (Figure 5.19). In other words, this evaluates at what geometrical parameter (support thickness, and pore diameter) of the porous support will the overall flux be the 90% relative flux performance with respect to the unsupported membrane.

5.5. Effect of variation in support geometry on flux

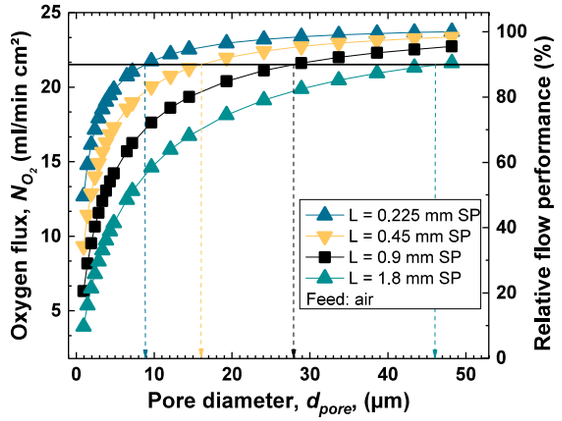

Figure 5.19: The relative flow performance of the flux through an asymmetric membrane for 3-end mode using air as feed gas and varying support thickness and pore diameter. SP represents support at the permeate side, and L is the thickness of the porous support. The operating pressure is as stipulated in Table 5.1.

From the intersecting points of the plots to the horizontal 90% limit (Figure 5.19), the corresponding pore diameters were measured. Figure 5.19 shows that the 0.225, 0.45, 0.9, and 1.8 mm thick porous supports yielded the same flux (at 90% relative flow performance of the membrane) with pore diameters of approximately 9, 16.2, 28, and 46 µm, respectively, at the same porosity of 43%. The relationship between the support pore diameter and thickness, with respect to the 90% relative flow performance of the asymmetric membrane was further studied. Also, since a specific flux (90% relative flow performance of the membrane) is being investigated, a constant interface pressure is expected irrespective of the support geometry.

From the Wagner equation, which is used for the description of the transport through the dense membrane, the only unknown in this case is the membrane-support interface pressure. Therefore, solving separately the Wagner equation for the flux (at 90% membrane performance) through the dense membrane, the membrane-support interface pressure (P''_{O_2}) was evaluated by rearranging Eq. (9) as

$$P''_{O_2} = P'_{O_2} \times \mathrm{e}^{-\frac{16F^2 N_{O_2} d_{mem}\left(1+\frac{L_c}{d_{mem}}\right)}{RT\sigma}} \tag{5.1}$$

where d_{mem} is the thickness of the dense membrane. This pressure was employed in the evaluation of the BFM for single gas transport (Eq. (2.64)) through the porous support. In section 5.5.1 the relation that the permeability scales with the square of the pore diameter ($B_o \propto d_{pore}^2$) was presented. Therefore, using this relation, the evaluated interface pressure, and substituting in the BFM for single gas permeation, the relationship between the porous support's thickness and the pore diameter for single gas permeation was rearranged to be

$$L_{Support} = \frac{P_A - P_B}{NRT}\left(\frac{\varepsilon}{\kappa}\times\frac{d_{pore}}{3}\sqrt{\frac{8RT}{\pi M_{O_2}}} + \frac{0.0079\times d_{pore}^2 P''_{O_2}}{\eta}\right) \tag{5.2}$$

L =	Length	d_{pore} =	Pore diameter	R =	Molar gas constant
N =	Flux	P_A / P_B =	Pressure at interface/permeate	T =	Temperature
ε =	Porosity	M_{O_2} =	Molecular mass	κ =	Tortuosity factor

Solving equation Eq. (5.2) for average pore diameter in the range of 1-50 µm for the flux considered, the corresponding support thicknesses were evaluated.

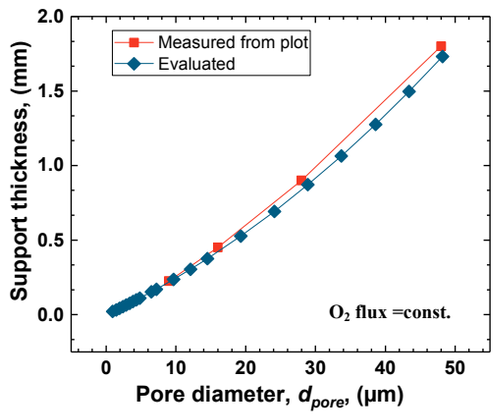

Figure 5.20: The support thickness as a function of the pore diameter for the evaluation the 90% relative flux through an asymmetric membrane for 3-end mode with the support at the feed side (SP), using air as feed gas. The plot in red is the measured data from (Figure 5.19).

The red curve corresponds to the intersection points between the plot and the horizontal axis in Figure 5.19, and it fits well with the evaluated data points (Figure 5.20) obtained by solving Eq. (5.2). Therefore, when using similar operating conditions, thinner supports allow smaller pore sizes, whereas thicker supports require larger pore sizes. This can be used for the optimization of the support's microstructure with regards to mechanical strength and permeability.

5.5.3.1 Conclusion

Reducing the thickness of the porous support yielded an increase in flux. However, thin supports may not give the desired mechanical stability needed for the asymmetric membranes in application. As such this observation will be used as basis in section 5.7 for the design of a double support layer system. Whereby the geometry of the thin and the thick support can be incorporated in a single graded layer system in order to optimize the support and consequently improve flux. Under same operating conditions, thinner supports with small pore diameter showed same flux as thicker supports with larger pore diameter. This can be used to optimize support's microstructure with regards to mechanical strength and permeability.

5.5.4 The effect of anisotropic scaling

Isotropy occurs when the material property of a structure is uniform in all direction, while anisotropy occurs in the case of direction-dependent property. The pore diameter of the porous

support as presented in section 5.5.1 was scaled isotropically, as the structure was scaled equally in all directions. To study the effect of anisotropy in the porous support, it was scaled only in the flow direction. The obtained anisotropic structure is shown in Figure 5.21. The effect of the structure on flux was investigated. Scaling the porous support in the flow direction by a factor of 0.5 and 2 tantamount to compression and stretching, respectively in the flow direction.

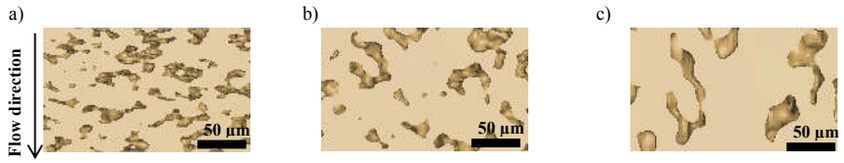

Figure 5.21: Changes observed in the shape of the pores as result of scaling the porous support in the flow direction by a factor of (a) 0.5, (b) 1, and (b) 2, respectively.

The structure parameter (permeability, pore diameter, and tortuosity) of the different scaled structures obtained were evaluated. Figure 5.22 shows the evaluated values of the permeability, pore size and tortuosity factor of the different scaled structures.

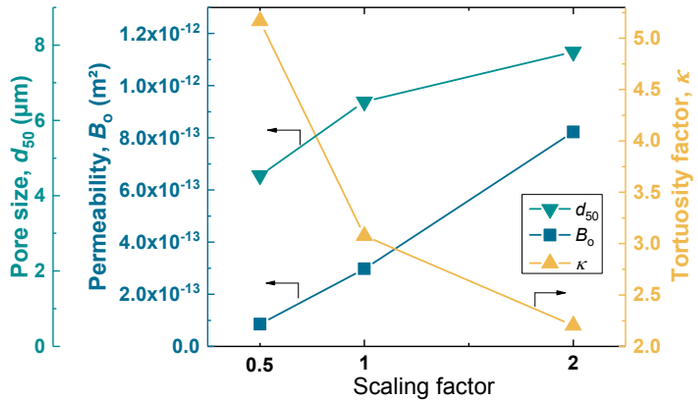

Figure 5.22: The structure parameter (pore size, permeability and tortuosity) of the porous support as a function of scaling in the flow direction.

From Figure 5.22 the pore diameter as well as the permeability of the porous support increased with increase in scaling factor, but the tortuosity factor reduced with increase in scaling factor. The reason is, the more the structure is stretched, the more the pores become more aligned to the flow direction and less tortuous ($\tau \rightarrow 1$). Also, the more channel-like the travel path of the fluid is, the easier it is for the fluid to permeate through. Therefore, all three parameters favour an increase of the flux with increasing stretch factor in the flow direction as shown in the result in Figure 5.23. The tortuosity factor for the isotropically scaled structure is constant. Using the relation $B_o \propto d_{pore}^2$ (refer to Section 5.5.1), the pore diameter and the permeability of the support for the isotropically scaled structure was evaluated.

In Figure 5.23 the flux obtained from the isotropic and anisotropic scaled samples were compared for the transport processes considered (3-end and 4-end mode). Air was used as feed gas for this evaluation.

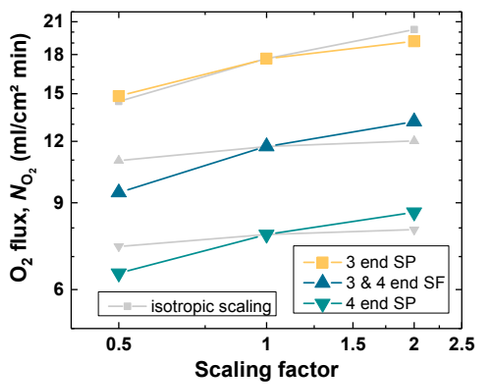

Figure 5.23: The oxygen flux as a function of isotropic or anisotropic scaling factor, for the transport processes (3-end and 4-end mode). SF/SP is support at the feed/permeate side, respectively.

From Figure 5.23 the 4-end mode irrespective of the support position and the 3-end mode with the support at the feed side showed similar trends. The anisotropic scaling was observed to be more effective with increased scaling factor for these cases. This can be attributed to the fact that the binary diffusion term of the mixed gas permeation equation of the BFM is the rate limiting factor. Therefore, as the tortuosity factor (k) reduces with increased anisotropic scaling factor, the effect of the binary diffusion term decreases and this invariable increases the flux, even exceeding the maximum plateau for isotropic scaling. On the other hand, the tortuosity factor is independent on isotropic scaling.

For the 3-end mode of transport and with the support at the permeate side, an opposite trend was observed. For this case the isotropic scaling was more favourable than the anisotropic scaling for large scaling factor. However, the trend at a smaller scaling factor was comparable for both isotropic and anisotropic structure. This behaviour can be attributed to the effect of the Knudsen diffusion term (2.63) of the binary friction model (2.72) on the flux. This stems from the fact that, for the range of pore diameter considered, the transport was dominated by the Knudsen diffusion term. The pore diameter which is the only varying term for the Knudsen diffusion (2.63) scales differently for both cases. For the isotropic case, the pore diameter is either uniformly shrunk or coarsened by scaling with a factor of 0.5 or 2, respectively. But for the anisotropic case, it is compressed or stretched in the flow direction resulting only in a smaller change of the effective pore diameter. Thus, the anisotropic scaling is less effective with regards to increasing flux for the single gas permeation transport. Whereas, these elongated pores favour mixed gas permeation through the porous support and might find application in membrane reactors.

5.5.4.1 Conclusion

Anisotropic tailored support microstructure (elongated pores) will be favourable for mixed gas permeation through the support (e.g. membrane reactors). Whereas for single gas transport

through the porous support, both isotropic and anisotropic scaled supports have comparable effects on flux.

5.6 Convective flow in the porous support

Increase in pore diameter of a porous support yields an increase in flux through an asymmetric membrane. However, a different behaviour has been observed for mixed gas permeation as presented earlier (section 5.5.1). Depending on the position (feed or permeate side) of the porous support no further increase in flux is observed above a certain pore size, rather it leads off into a plateau.

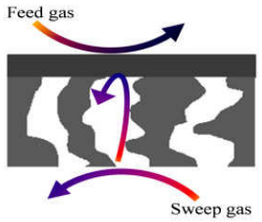

Figure 5.24: The transport of the sweep gas through the large pores to the membrane-support interface [132].

Notwithstanding that for large pore diameters the gas flow as schematically depicted in Figure 5.24, should give rise to a viscous flow [133] up to the membrane-support interface. As a result, such microstructure, should lead to an increase in flux, but this behaviour is not accounted for or observed with the one-dimensional numerical model. This is because the model describes the transport as being dominated by binary diffusion, which is no longer the case at very large pore diameters where convection processes are expected. Therefore, a more appropriate computational fluid dynamics [134-136] evaluation is needed to describe the transport for very large pores.

As such, the effect of the sweep gas on porous support with large pore diameter was simulated. This was to understand how deep or shallow the convective flow of the sweep gas is before it sweeps away together with the permeated gas. For this evaluation, the CT data of an inverse tape cast received from colleagues at the department of Energy Conversion and Storage, Technical University Denmark was employed. Since the inverse tape cast pores are channel-like, the structure is more ideal for understanding the behaviour of the gas flow in the pores. Using the geodicct software, the 3D reconstruction of the CT data as explained in section 3.2 was carried out, and afterwards meshed. The mesh file was exported to be used for the simulation in ANSYS Fluent. The y-direction of the structure as shown in Figure 5.25 was used as the flow direction.

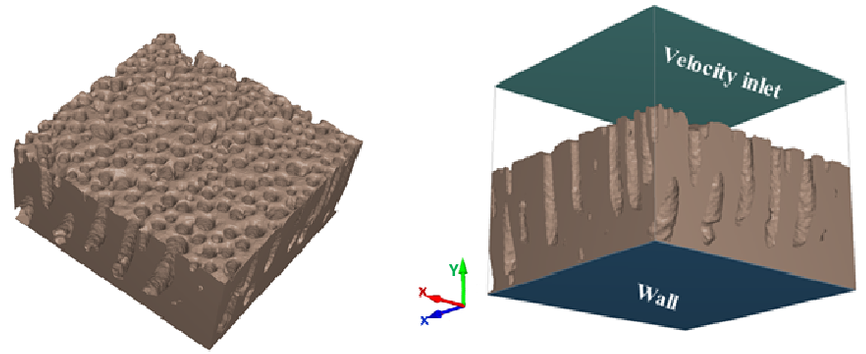

Figure 5.25: Three dimensional representation of the CT data of an inverse tape cast asymmetric membrane, specifying the boundary conditions used for the simulation in anysy fluent.

In addition to the boundary conditions stipulted in section 4.3, the displaced area parallel to the surface of the porous support (the positive y-axis shown in green) and the opposite side (the negative y-axis shown in dark blue) were taken to be the velocity inlet and wall, respectively. This is to mimic the fact that the sweep gas is inert and will not pass the membrane. The other surfaces perpendicular to the in-flow and the wall surfaces were set to outflow (pressure outlet).

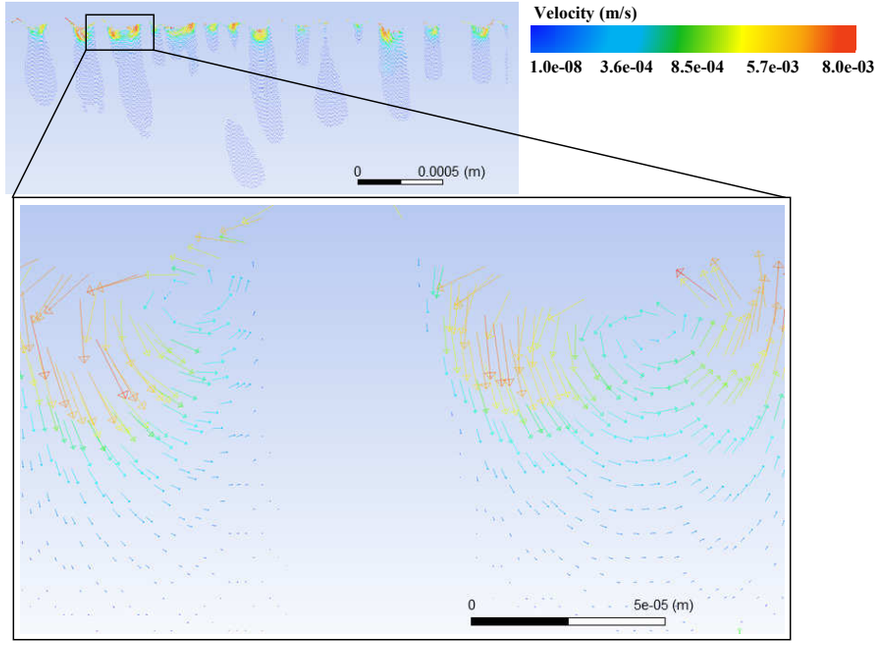

Figure 5.26: The flow of the gas through the pore. The length and colour of the arrows shows the magnitude of the velocity.

Figure 5.26 shows the velocity magnitude of the sweep gas through the pore. The convection takes place only at the pore entrance regions for most of the pores. The shape of the pore was observed to affect the velocity and the depth of the gas travel.

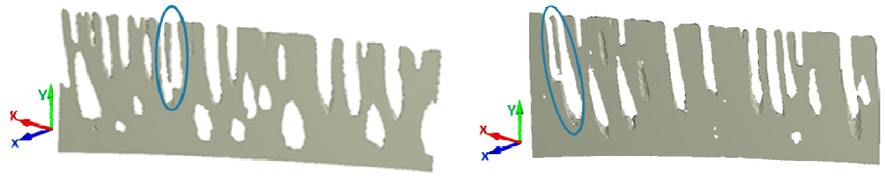

Figure 5.27: The CT image of the freeze cast structure, showing the shape of the pore perpendicular to the flow direction.

Pores connected as shown in the areas marked in blue ovals in Figure 5.27, were observed after the flow simulation to have a higher in-pore velocity (Figure 5.28) and as such more favourable. As a result, flow does not stall as in a blind pore rather one “limb” acts as an inflow and the other as outflow channel. This will reduce the travel time of the permeated gas and also increase the flux.

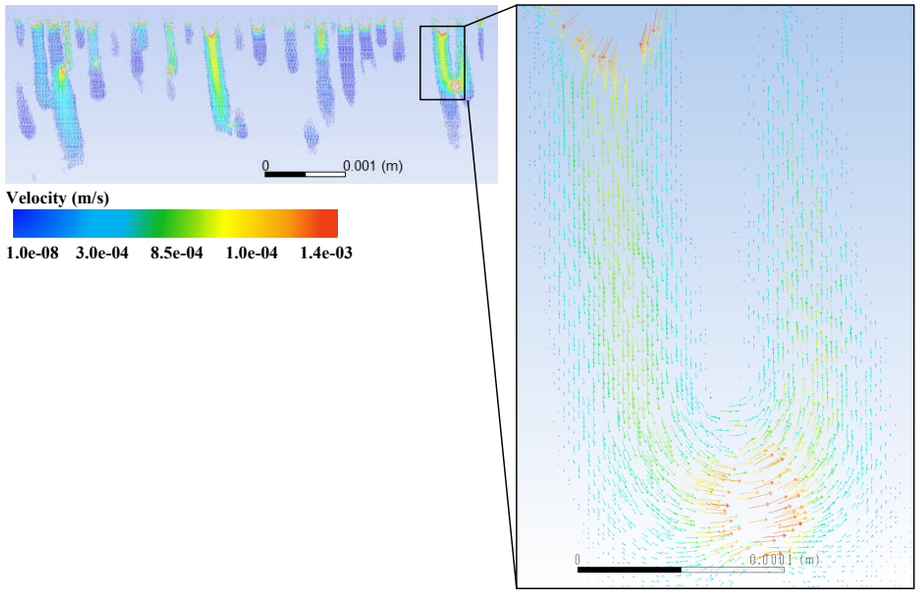

Figure 5.28: The velocity field showing high velocity at the u-shaped pores.

From Figure 5.28, the velocity observed when the pores are connected in u-shape are higher compared to when the pores are blind. However, this in-pore velocity is not affected or dependent only on the pore opening diameter at the surface or within the porous support,

rather on the overall morphology (shape, size and orientation) of the pore. For unbent channel-like pores, shallow depth convection at the gas side were mostly observed. From Figure 5.26 and Figure 5.28, the highest velocities obtained were 8 and 1.4 mm/s respctively. The velocities vary depending on the position of the slice as explained earlier. The effect of the sweep gas velocity on the overall flux through the asymmetric membrane for the 4-end mode transport process was then evaluated. Firstly, the flux experimentally obtained according to ref. [119] for the 4-end mode transport process using air and argon as feed and permeate gas, respectively, was used for the evaluation of the permeate velocity. From the permeate flux which is 4.1ml/min cm^{-2}, the velocity of the gas flow in the pores of the porous support was calculated to be ~ 8mm/s. The pore velocity measured from experimental simulation is comparable to the pore velocity of the simulation. This confirms the assumption made earlier about the convective flow of the transported gas not being properly described by the mixed gas permeation equation of the BFM.

Furthermore, the tape cast, and freeze cast porous support microstructures were compared to investigate the effect of the support microstructures on convective flow. Similar operating conditions and operating steps carried out for the simulation using the inverse tape cast was employed here.

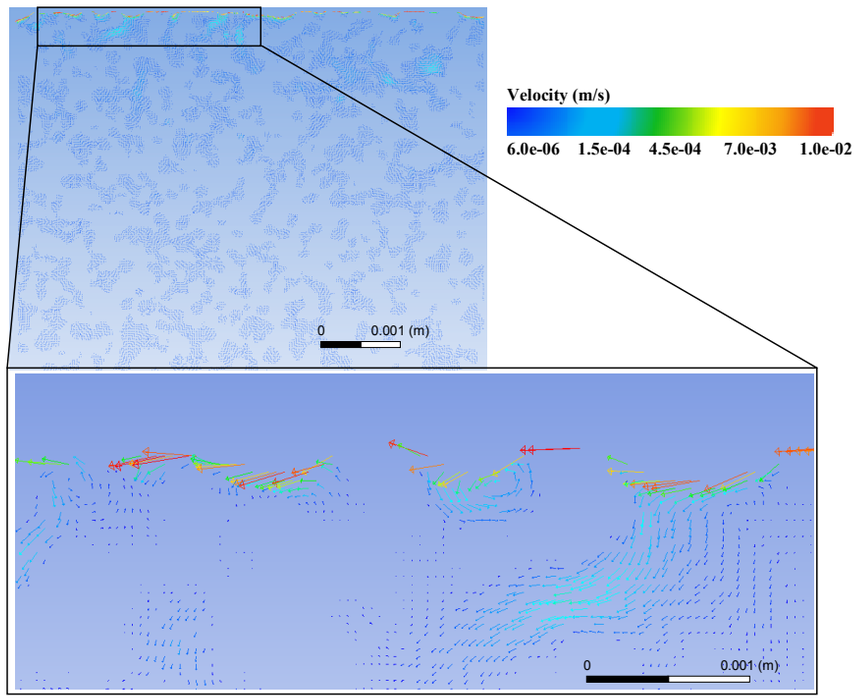

Figure 5.29: The simulated flow within the tape cast support showing the flow velocity (zoom) in the pores.

5.6. Convective flow in the porous support

From Figure 5.29, there was evidently the sweeping away of permeated species, but the flux showed shallow depth of travel for the sweep gas. This shallow flow depth existed more at the surface of the support. The tape cast shows lower flow velocities in the pores when compared to the other support microstructures. This might be attributed to the fact that the porous TC structure employed for the present simulation has an average pore diameter of 6.5 µm and is more tortuous the other support microstructures. As such no convective flow was expected in the pores.

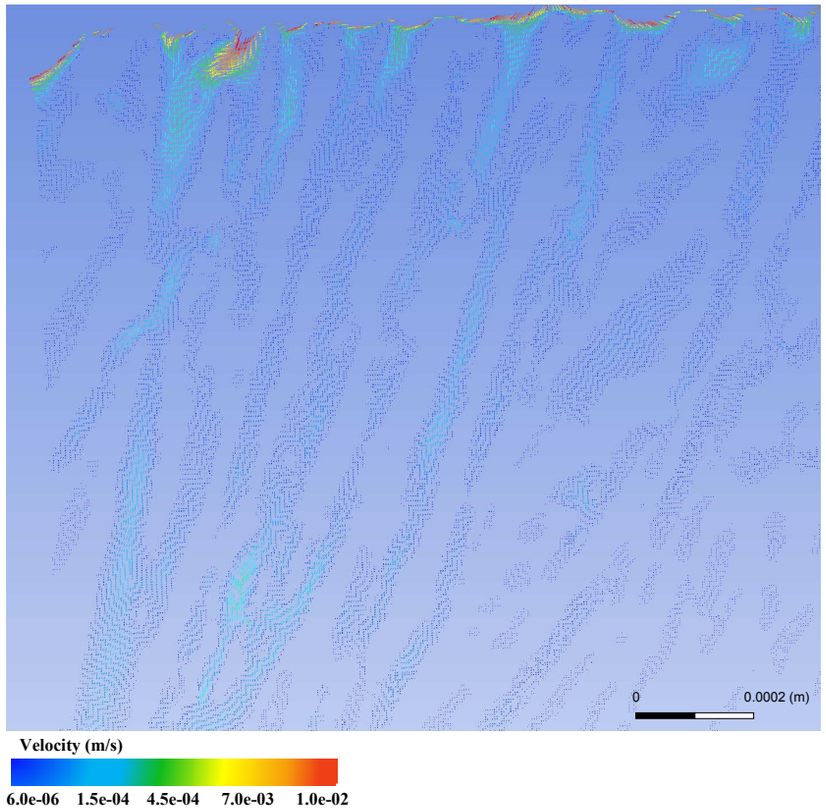

Figure 5.30: The simulated flow within the freeze cast support showing the flow velocity within the pores.

The freeze cast structure (Figure 5.30) had high velocities within the pores than the tape cast (Figure 5.29) or inverse tape cast (Figure 5.26); this could aid the collection of the permeated gas. In Figure 5.30, at a maximum velocity of 10 mm/s, there was just shallow depth flux of the sweep gas at the surface. The high velocities observed in the pores of the freeze cast porous structure might be dependent on the shape and orientation of the pore. When the pores are perpendicular to the inflow surface, it favours shallower depth sweep flow at the surface, just as was observed for the inverse tape cast (Figure 5.26). But when the pores are aligned at an angle or slanted with respect to the inflow region, the velocity in the pores increase.

From the observation made form the freeze cast and the inverse tape, convective flow exists for channel-like pores with large diameter. Therefore, the transport through the porous support can be better described using a computational fluid dynamics simulation.

5.6.1 Conclusion

U-shaped pores are assumed to be more favourable with respect to increase in permeated flux. Reason for this is that two openings can provide pressure differences. Therefore, if samples with inter opening between two parallel pores (u-shaped pores) can be experimentally processed, it is assumed to be more favourable with respect to increased permeated flux. Freeze cast channel orientation should be adapted to macroscopic flow field around the membrane to take into consideration pore angle in the flow direction.
In addition, it was observed that the freeze cast support had a higher flow velocity within the pores than the other (tape cast and inverse tape cast) support microstructures. This could be attributed to the aligning of the pores (slanted or inclined pores).

5.7 Comparison of freeze cast and tape cast porous structure

An experimental permeation measurement was carried out on both asymmetric membranes using air or oxygen as feed gas. It was observed as shown in Figure 5.31 that the two membranes had similar permeation behavior, irrespective of the feed gas used with the support at the feed side using argon as sweep gas.

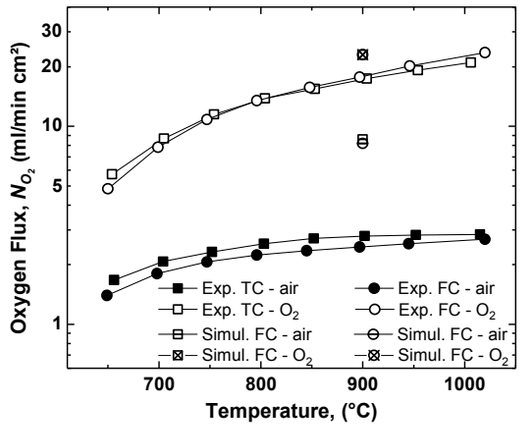

Figure 5.31: Shows the permeation measurements of the freeze cast and tape cast asymmetric membranes using air or oxygen as feed gas, and argon as sweep gas at varying temperature, as well as the simulated flux for the TC and FC at 900°C with same operating conditions as experiment.

When air was used as feed gas, the flux through the TC was higher than that through the FC structure in the range of temperatures considered.

Similarly, when using oxygen as feed gas in the permeation measurement, the FC support performs at temperatures above 800°C better than the TC support. In this case gas transport takes place only by oxygen self-diffusion and convective flow, which excludes binary gas diffusion. From the flux observed for the FC and TC asymmetric membranes with either air or oxygen as feed gas were comparable. This was not in agreement to observations made in literature, where the freeze cast structure was expected to have a higher flux than the tape cast sample irrespective of feed gas. As such, the effect of the geometrical parameters of the support microstructures on the overall flux through the membrane was further investigated.

The TC and the FC samples fabricated from BSCF3Zr material with comparable porosities were compared, to find out which factors is the main criterion for the flux performance. The TC porous support possesses randomly shaped pores with a tortuosity which depends on the pore volume and percolation of the pore network, caused by the burn out of a pore-former. Whereas for the manufacturing of the freeze cast structure, the grown ice crystals are the templates for the pores. By tailoring the growth and shape of the ice crystals, unidirectional and highly oriented pores with very low tortuosity are theoretically possible. As the microstructure of the freeze cast sample appears very inhomogeneous, it was sliced into twelve sections across the support thickness, in order to have a clearer description of the graded nature of the structure.

Since the TC support is very uniform, only four segments were evaluated. The free surface of the support was taken to be the position z = 0, while the membrane-support interface was taken to be the position z = 1000 µm (Figure 5.32).

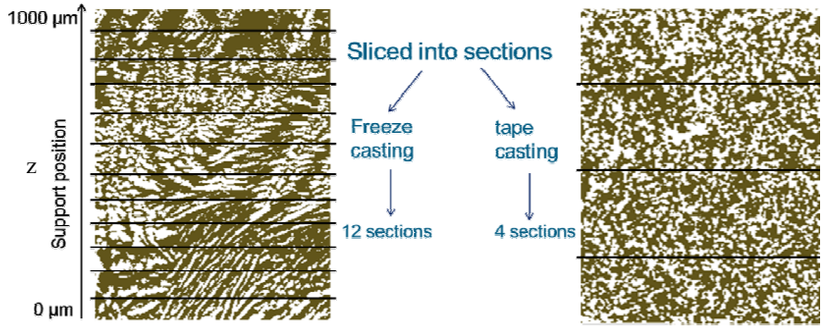

Figure 5.32: The sectioning of the freeze cast and tape cast asymmetric membranes before the evaluation of the geometric parameters.

The FC and the TC supports possess an average specific surface area ($A_{spec.support}$) of 0.16 m^2/cm^3 and 0.21 m^2/cm^3, respectively. The average surface area for the FC is 24 % lower compared to that of the TC support. Due to varying porosity and pore diameters, the specific surface area changes along the FC support thickness. This is not the case for the TC structure. As a result, the average surface area of the FC and TC supports were evaluated on the sectioned layers as shown in Figure 5.33.

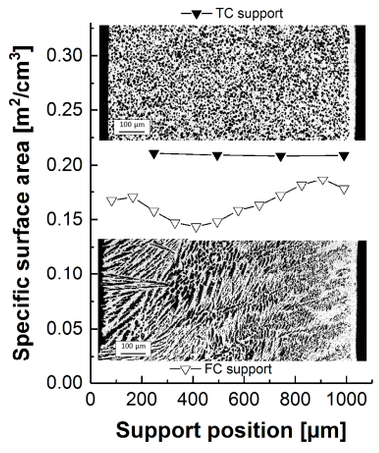

Figure 5.33: Specific surface area vs. support position (for the sections) where 0 is the air surface side and 1000 the position underneath the membrane layer [102].

The evaluated average geometrical parameters of the entire TC and FC samples and the sectioned layers have been introduced in section 5.3. Figure 5.34 and Figure 5.35 shows the plot of the evaluated geometrical parameters for the different layers. Judging from the percentage of the closed porosity of the structures which is 0.04 % for TC and 0.09 % for FC supports, the pores of the FC and TC structures are very well connected and contribute in gas transport.
As intended, both support types possess identical average porosities of 45 %. Nevertheless, the porosity of the TC support is homogenous over the support thickness, while the FC support shows a porosity gradient. This can also be attributed to the ice crystal growth and shape. The local porosity increases gradually from 32 % at the membrane-support interface (layer) to 55 % at the free surface, as shown in Figure 5.34.

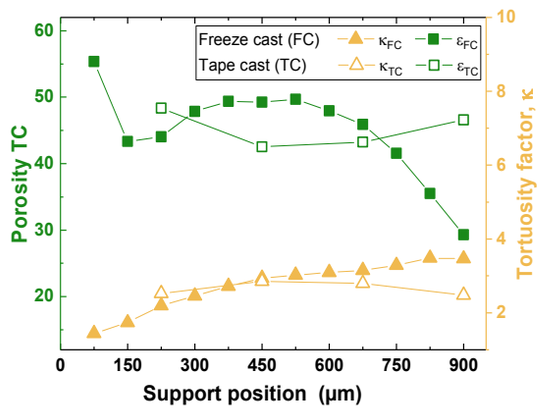

Figure 5.34: Profile of porosity (ε), and tortuosity factor (κ) plotted vs. support thickness position (x-coordinate) where 0 is support side and 1000 position underneath the membrane layer.

The average tortuosity factor evaluated from the XCT, for the not optimized FC support is 3.2 and thereby nearly the same as for the TC support with 2.9. However, while tortuosity of the TC support does not vary over the support thickness, the FC support shows an increasing tor-

tuosity factor of 1.4 at the air surface, and up to ~3.5 at the membrane-support surface as can be seen from Figure 5.34. This is because the nucleated ice crystals are templates for the pore shape and size, the structural parameters of the FC structure are anisotropic in nature. This anisotropy in porosity is caused by the zone in which ice crystals nucleate and start to grow. Orientation of the ice crystals and the resulting porosity improves gradually with the distance from this nucleation zone. However, porosity and pore size of the TC support are homogeneously distributed, while the FC support exhibits a gradient along the growth direction of the ice crystals Figure 5.34. The nucleation zone has the least porosity and tortuosity factor.

The average pore opening diameter (d_{50}) for each layer was calculated by simulating the pressing of a non-wetting fluid into the pore and recording the applied pressure and the volume absorbed using the liquid intrusion porosimetry method (section 4.1.2). The average d_{50} of FC support is 6.8 µm and slightly larger than for TC support with 5 µm (Figure 5.35).

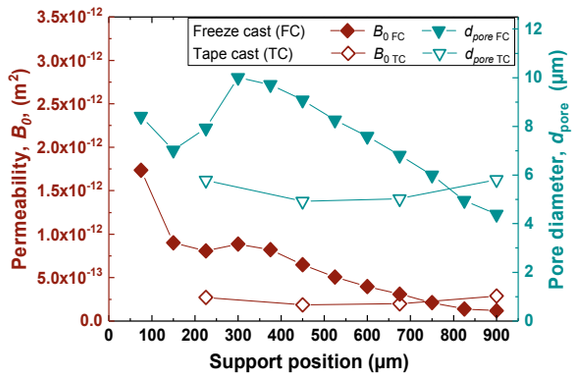

Figure 5.35: Profile of average pore opening diameter (d_{50}) and permeability at 900°C plotted vs. section position (x-coordinate).

The simulation of viscous flow transport through the supports (Figure 5.35) shows a better permeability of the FC support up to a support position of around 800 µm. Near the membrane (the bottom side during freeze casting), a transition exists where the TC support starts to perform better. Reason for the transition in gas exchange performance is the nucleation zone of the FC support. In this zone porosity and average pore diameter are lower compared to the TC support, forming a bottle neck for gas exchange as shown by the permeation measurement in air at high temperatures.

The locally resolved sample parameters have been employed to simulate in 1D the flux through both types of asymmetric membranes. Wagner equation (Eq. 2.18) and the Binary Friction Model (Eq. 4.5) were used to describe the transport through the dense membrane and the porous support, respectively. Continuity relation (the flux through the dense membrane equals the flux through each section of the porous support) through the asymmetric membrane was assumed. Therefore, to be able to simulate a continuous flow through the layered support of the asymmetric membranes, the porous supports were modelled to be connected in series. This ensures that the flux in each layer equals to one another and is also equal to the flux through the dense membrane. This is schematically explained using Figure 5.36.

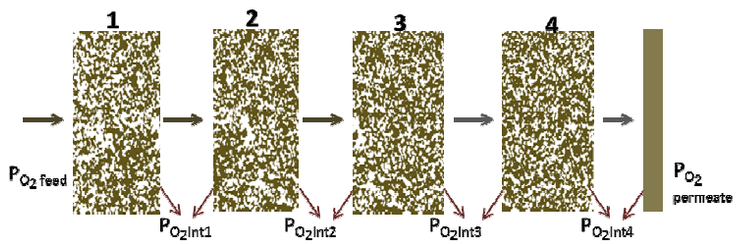

Figure 5.36: Schematically representing the solution of the flux through the sections of the porous support simulated in series using the sequential tape cast asymmetric membrane as an example.

The one-dimensional solution of BFM for the flux through layer 1 was equated to the flux for layer 2, and the same procedure was followed across the layers until the BFM solution of the flux through layer 4 was equated to the Wagner equation for the dense membrane. The interface pressures between layers (P_{O_2Int1}, P_{O_2Int2}, etc.), and the membrane-support interface pressure were evaluated. Similar steps were employed for the simulation of the flux through the porous support of the freeze cast asymmetric membrane. When oxygen or air was used as feed gas, the feed/permeate pressure was taken to be 1000/217 mbar or 195/40 mbar, respectively.

After the analytical simulation at 900°C using similar operating conditions as in experiment, the evaluated flux from the two structures was also comparable. When oxygen was used as feed gas, both structures had a comparable flux of ~23ml/min cm. Similarly, when air was used as feed gas, the flux through TC and FC was 8.6 ml/min cm² and 8.2 ml/min cm², respectively. The simulated fluxes were higher than the experimental observed flux values; this could be attributed to the fact that ideal situations were assumed for the simulation. The flux through the TC was slightly higher than that from the FC. Based on the observation made from simulating the structural parameters of the sectioned FC and TC samples, the support zone with the onset of nucleation of the ice crystals for the FC was seen to be rate limiting. Similarly, from the convective flow simulation in section 5.6, the orientation of the pore of the FC structure from the air side favours flux increase more than the pore orientation of the TC structure. This also confirms that the nucleation zone of the FC structure rate limits the overall transport. This would give rise to concentration polarization within the porous structure. For mixed gas permeation, concentration polarization within the support contributes a lot in limiting the flux. Also, above 700 μm position of the support thickness (Figure 5.34) the porosity tends to take a steep decreasing dive, to about 30%. This invariably increases bottlenecks in the pores around these areas and thereby limiting the flow through it. This part of the FC structure is slightly dense, thereby introducing a limiting factor for the observed flux.

5.7. Comparison of freeze cast and tape cast porous structure

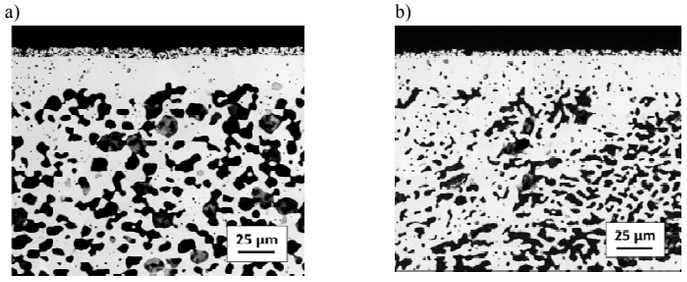

Figure 5.37: the comparison of the porous support area close to dense membrane for (a.) tape cast and (b.) freeze cast asymmetric membrane.

The pores present in the freeze cast in this area (Figure 5.37) are less cylindrically orientated in the flow direction and appear to be more randomly shaped like the tape cast. But in the case of the FC, it has a lower porosity than the tape cast. In addition, the morphology of the freeze cast porous support might also contribute to the limitation. From Figure 5.3 and Figure 5.4, we can see from the reconstructed image of the freeze cast sample that the channels of the pore are not totally oriented parallel in the flow direction throughout the thickness. From the mid-section, the pores tend to orientate at an angle perpendicular to the flow direction. This builds up a kind of a bridge in the flow direction and in turn will also limit the flux.

5.7.1 Effect of removing the nucleation zone

The evaluated geometrical parameters for the 12 sectioned layers of the FC structure were used. A further study to investigate how the flux would be improved if the rate limiting zones are removed was carried out. The effect of removing the nucleation zone from the FC structure before printing the dense membrane was simulated. The support thickness was maintained during the investigation. In other words, for each layer removed, the thickness of the remaining layer is been adapted to account for it.

Figure 5.38 shows the effect of the removal of the layers of the FC from the 12^{th} layer (nucleation zone) to the 1^{st} layer (coarse – air side). With the removal of each layer and subsequent normalization of the support thickness, it yielded an increase in flux. After the removal of the first three layers from the membrane support interface, the flux increased from 8.2 to 9.2 ml/min cm². Furthermore, if the layers were removed until the support had a uniform geometry as the last coarse layer, the flux increased up to ~15 ml/min cm². The porosity, pore diameter, effective diffusivity, and tortuosity factor of the support is improved as the layers are removed. These improved structural parameters of the porous support contributed to the increase in flux observed.

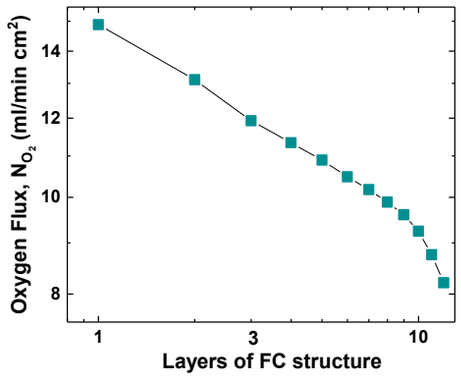

Figure 5.38: Flux improvement through the FC support as a function of removing the sectioned layers.

Notwithstanding the observed increase in the flux, the available surface area reduces as the layers are removed from the nucleation zone towards the air surface side of the support as was shown in Figure 5.33. Presently the model does not consider the effect of surface exchange; as such this was not taken into account during the simulation. The membrane-support interface of the structures considered needs to be further improved to increase available surface area without limiting the flux.

5.7.2 Conclusion

In principle the hierarchical microstructure of the freeze cast support provides an enhanced gas transport capability. However, particularly the transition zone near to the dense membrane, originated by the freezing process, strongly constrains the diffusivity by insufficient porosity and pore opening diameters. Removal of 3 layers from this constricting zone (the area with the onset of ice crystal nucleation) improved flux. However, the surface area at the membrane-support interface should also be considered. This is so because it is essential for sufficient oxygen exchange at the membrane-support interface.

5.8 Outline for designing an optimized support microstructure

In previous sections, it has been established that increasing the pore diameter, and reducing the tortuosity and thickness of the porous support/substrate would increase flux. However, there is a limit to the extent these parameters can be varied. For instance, having a very thin support will increase flux but it will defeat the essence why the support was needed which is to offer mechanical stability. Porous substrates with very large pore opening diameters have a reduced available surface area at the membrane-support interface. A high surface area is needed at the membrane-support interface for the re-association of the diffused oxygen ion (from the membrane) to oxygen molecule.

A two-layer porous support system for the porous support of an asymmetric membrane (Figure 5.39) was investigated. This two-layer system comprises of a thick and a thin support layer combined as the porous substrate. Further on, the thick and the thin layer of the porous support will be referred to as layer A and layer B, respectively. Taking into consideration the membrane mechanical stability, the structural geometry of the two layers were modified as shown in Figure 5.39, to model/simulate an optimized substrate for OTMs.

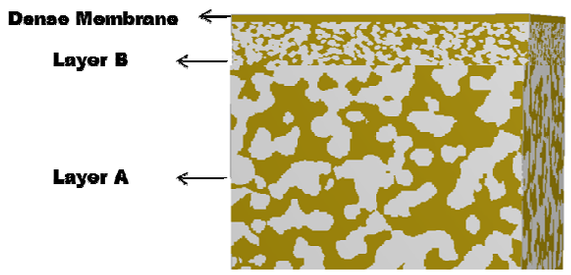

Figure 5.39: The proposed two-layer support system of an asymmetric membrane. The reconstructed 3D image of an acquired computer tomography data of a TC structure was modified and used here as an example.

The typical geometry of a tape cast substrate is assumed as the basis for the modification of the thin layer (layer B). In the same vein, the pore diameter of the thin layer considered for the thin layer was not more than 50% of the membrane thickness. The overall porosity considered for layer A was not higher than 45% because; from experimental point of view a higher porosity would not yield a mechanically stable structure. This is due to the fact that the higher the porosity the lower the strength [137]. The pore diameter of layer A will be modified with consideration to the previous studies made in section 5.7. The continuity relation was fulfilled by using the same procedure already presented in section 5.7.

5.8.1 Operating conditions considered and procedure

Air and argon were used as feed and sweep gas, respectively, at an operating temperature of 900°C. The total pressure at the feed and permeate side of the asymmetric membrane were maintained at 1000 mbar. The feed and permeate partial pressure of oxygen was assumed to be 200 mbar and 41.5 mbar, respectively. The membrane thickness was also assumed to be 20 µm. The geometrical parameters of the investigated porous structures as will be presented in section 5.8.1.1 were assumed using typical membrane supports as reference [28, 29, 95, 102]. Transport equations as stipulated in Table 4.2 was used for the different transport configuration considered. The 3-end mode and the 4-end mode transport processes with the support orientations as in section 2.2.1 were considered for the present simulation studies.

5.8.1.1 Layer geometry and procedure

The thickness of layer B was varied from 10 to 100 µm. The thickness of layer A was adjusted accordingly so that the sum remained constant at 0.9 mm. Using the measured data as reference, $B_0 \propto d_{pore}^2$ (see section 5.5.1) was employed for evaluating the permeability when scaling the pore diameter of the layers. The geometrical parameters of layer B for all structures considered are as stipulated in Table 5.6.

Tortuosity factor, τ	Pore diameter, d_{pore} (µm)		Porosity ε		
1.4-2.9	3.0	6.50	35%	40%	45%

Table 5.6: Input parameters for layer B (thin support layer) for all supports considered.

For the optimization of the geometry of a porous support of an asymmetric membrane, the pore diameter of layer A (thick support layer) was varied. From the previous evaluation made in section 5.5.1, it was seen that varying the pore diameter above 35 µm showed negligible increase in flux. Therefore, in the present evaluation the pore diameter of layer A will be varied from 6.5 to 40 µm for the structures considered. Tape cast and inverse tape cast (ITC) support microstructure of an asymmetric membrane were considered. The variations in the geometry of the TC and ITC considered for the present study is as summarized in Table 5.7.

	Tortuosity factor, τ	Pore diameter, d_{pore} (µm)	Porosity, ε
Tape cast	2.9-1.4	6.50-40	45%
Inverse tape cast	1.4-1.0	6.50-40	45%

Table 5.7: Input parameters for the layer A (thick support layer) for the tape cast and inverse tape cast.

5.8.2 Variations in geometrical parameters of the layers

5.8.2.1 Effect of porosity, thickness and pore diameter on flux

As has been pointed out form the previous sections, the flux through the membrane with the support at the feed side is always higher than when the support is at the permeate side. Similar trend was also observed here. For the range of pore diameter considered, the flux with the support on the feed side was higher than with the support at the permeate side by approximately 33%. For the **TC** structure for both transport processes and for the range of pore diameters considered for Layer A (Figure 5.40):

1) Varying the thickness of the thin layer (Layer B) did not show a significant increase in flux. (< ~1%).
2) Less than 4% improvement in flux was observed for the transport processes considered.

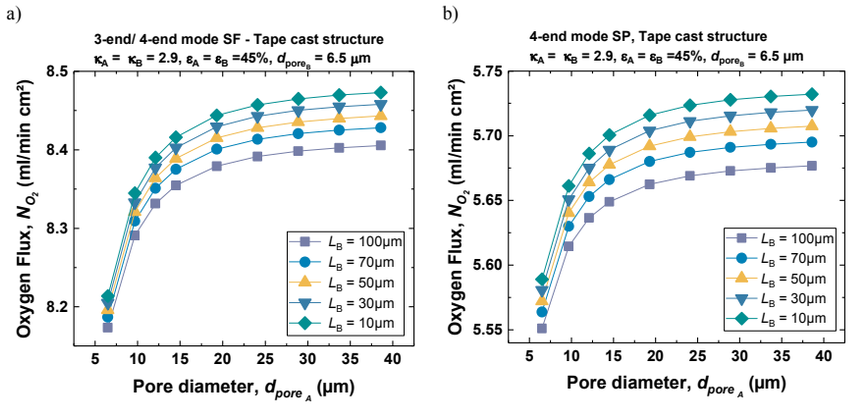

Figure 5.40: Tape cast structure - varying the pore diameter of layer A and the thickness of the two layers for (a) 3-end and 4-end mode with the support at the feed side and (b) 4-end mode with the support at the permeate side. SF and SP depict support and the feed and permeate side, respectively. L, κ, and ε, are the thickness, tortuosity factor, and porosity of support layer, respectively. The subscripts A or B refer to layer A or B.

Similarly, for an **inverse tape cast** porous structure, a similar trend in flux (Figure 5.41) was observed by varying the pore diameter of layer A. This can be attributed to the fact that the binary diffusive term of the BFM which does not scale with pore diameter is rate limiting for mixed gas transport. However, **the inverse tape cast** showed better improvement in flux as the thickness of the thin layer is reduced compared to the tape cast support. Approximately 6% relative flux improvement was gained by reducing the thickness of the thin layer from 100 to 10 µm.

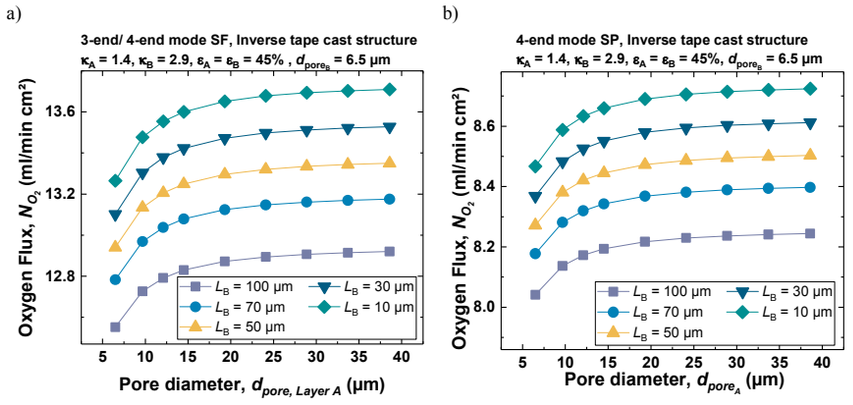

Figure 5.41: Inverse tape cast structure - varying the pore diameter of layer A and the thickness of the two layers for (a) 3-end and 4-end mode with the support at the feed side and (b) 4-end mode with the support at the permeate side. SF and SP depict support and the feed and permeate side, respectively, L, κ, and ε, are the thickness, tortuosity factor, and porosity of support layer, respectively. The subscripts A or B refer to layer A or B.

Considering the 3-end mode transport process with the support at the permeate side for both inverse tape cast and tape cast structures; increasing the pore diameter of the thick layer yielded an increase in the overall flux (Figure 5.42). The effect of the thickness of layer B increases as the thickness is reduced from 100 to 10 µm. However, at lower pore diameter, the effect of varying the thickness of the layers was negligible.

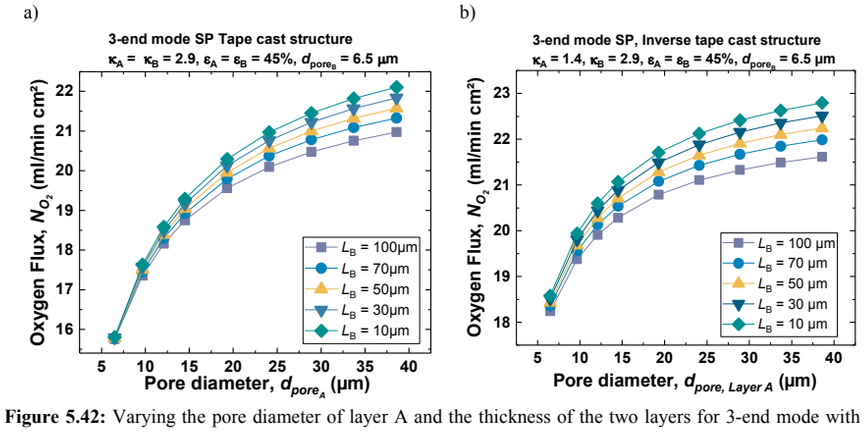

Figure 5.42: Varying the pore diameter of layer A and the thickness of the two layers for 3-end mode with the support at the permeate side for (a) tape cast and (b) inverse tape cast structure. L, κ, and ε, are the thickness, tortuosity factor, and porosity of support layer, respectively. The subscripts A or B refers to layer A or B

At a constant thickness of 10 µm for the thin layer, considering the 3-end mode transport process, the effect of reducing the average pore diameter of layer B from 6.5 to 3 µm (as a function of pore diameter considered for layer A) was modelled. This reduced the overall flux through the porous support for both tape cast (Figure 5.43.a) and inverse tape cast structure (Figure 5.43. b), but it is more evident for the tape cast structure.

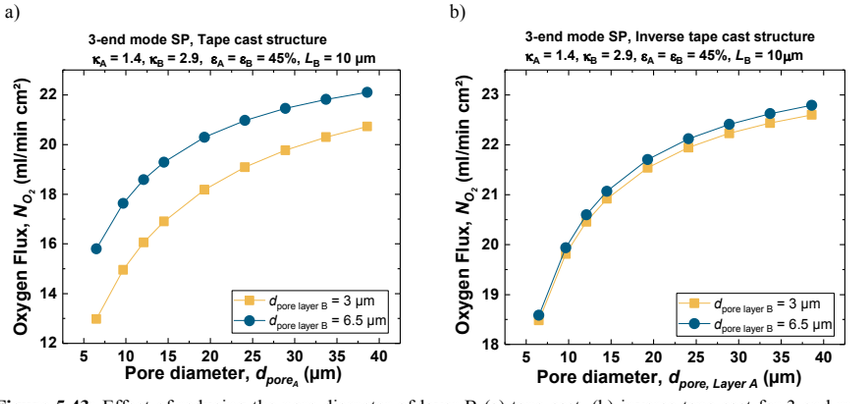

Figure 5.43: Effect of reducing the pore diameter of layer B (a) tape cast, (b) inverse tape cast for 3-end mode transport process with the support at the permeate side. κ_B and ε_B are the tortuosity factor and porosity of layer B, respectively. The subscripts A or B refers to layer A or B.

Furthermore, the porosity of the thin layer was varied as stated in Table 5.6 at a constant thickness and as a function of pore diameter considered for layer A.

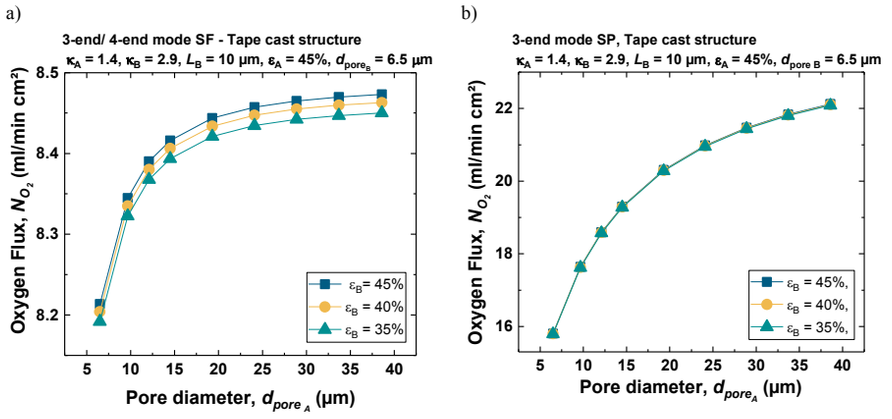

Figure 5.44: The effect of varying the porosity of layer B on overall flux using a tape cast structure with the support at the (a) feed and (b) permeate side, respectively considering the 3-end mode transport process. L, κ, and ε, are the thickness, tortuosity factor, and porosity of support layer, respectively. The subscripts A or B refers to layer A or B

For 3-end mode transport process with the support at the permeate side (Figure 5.44.b), the effect of porosity is negligible. The relative difference between the fluxes when the thin layer porosity is 45 % compared to when it is 35 % within the pore diameter ranges considered was less than 1%. Whereas, for mixed gas permeation transport, a 1% increase in the overall flux was observed when the porosity of the thin layer was increase from 35 to 45% for the tape cast structures (Figure 5.44.a).

5.8.2.2 Effect of tortuosity factor

The effect of reducing the travel path through the porous support (tortuosity factor) was evaluated, while maintaining the ideal characteristics of the structures considered. For the tape cast structures, a clear increase in flux was observed for both transport processes considered.

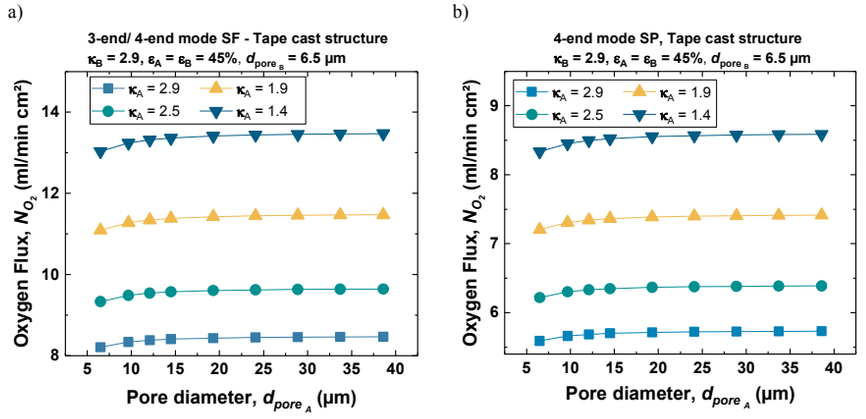

Figure 5.45: The flux through a tape cast asymmetric membrane with the support at the (a) feed and (b) permeate as a function of reducing the tortuosity factor and increasing the pore diameter of layer A for mixed gas permeation transport process. SF and SP depict support at the feed and permeate side, respectively.

For tape cast structure considering the 3-end mode/4-end mode transport process with the support at the feed side (Figure 5.45.a), the flux increased by approximately 70% when the tortuosity factor of the thin layer was reduced from 2.9-1.4. Similarly, for tape cast structure, for 4-end mode with the support at the permeate side (Figure 5.45.b), 54% increase in overall flux was observed.

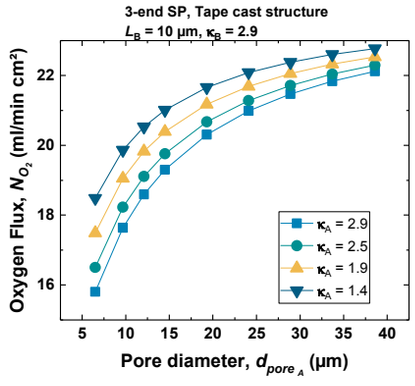

Figure 5.46: The flux through a tape cast asymmetric membrane with the support at the permeate side, as a function of reducing the tortuosity factor and increasing the pore diameter of layer A, for 3-end mode transport process. SP depict support at the permeate side.

For the 3-end mode transport in the range of pore diameter considered with the support at the permeate side for a tape cast structure:

(1) Reducing the tortuosity factor of the thin layer increased the overall flux. However, with increasing pore diameter of layer A, the improvement becomes negligible.

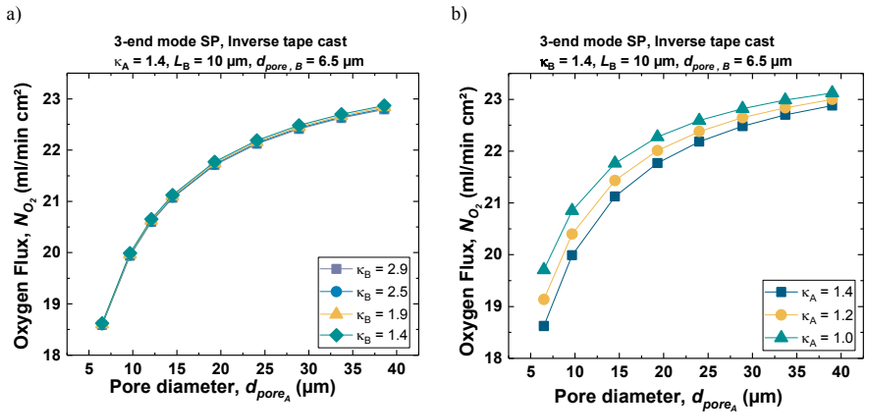

Figure 5.47: The flux through a an inverse tape cast asymmetric membrane for 3-end mode transport process with the support at the permeate side, as a function of increasing the pore diameter of layer A and reducing the tortuosity factor of (a) layer B and (b) layer A.

For the 3-end mode transport in the range of pore diameter considered with the support at the permeate side for an inverse tape cast (Figure 5.47):

(1) Reducing the tortuosity factor of the thin layer from 2.9 to 1.4 had almost no effect on the overall flux.

(2) Whereas when the tortuosity factor of the thick layer support was reduced from 1.4 to 1.2, there was flux improvement, but this reduced with increasing pore diameter of layer A.

Therefore, based on the flux improvement observed by reducing tortuosity factor of layer B (κ_B), κ_B for the inverse tape cast for mixed gas transport was taken to be 1.4 and the tortuosity factor of the thick layer was reduced from 1.4 to 1.0 (Figure 5.48).

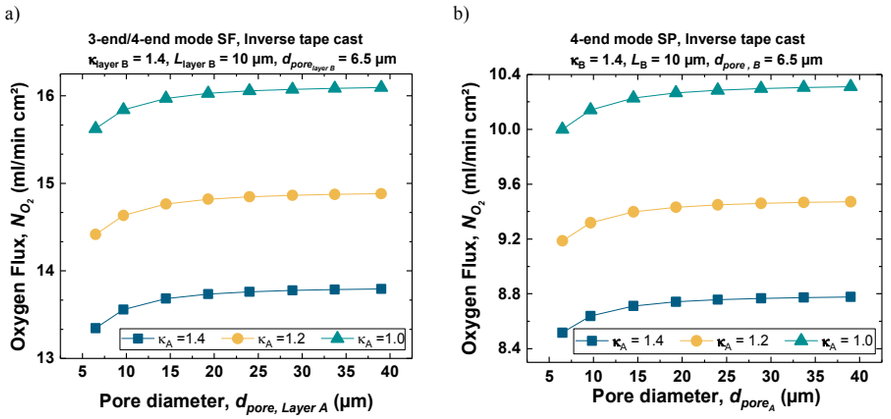

Figure 5.48: The flux through an inverse tape cast asymmetric membrane with the support at the (a) feed and (b) permeate as a function of reducing the tortuosity factor and increasing the pore diameter of layer A layer A for mixed gas permeation transport process. SF and SP depict support at the feed and permeate side, respectively.

For inverse tape cast considering the 3-end mode/ 4-end mode with the support at the feed (Figure 5.45.a) side and the 4- end mode with the support at the permeate side (Figure 5.45);

1) Reducing the tortuosity factor of layer, A (τ_A) from 1.4 to 1.0 at a tortuosity factor of 1.4 for layer B (τ_B) yielded approximately 15% increase in flux for all transport configurations considered.

5.8.3 Conclusion

There is a high need for the fabrication of a mechanically stable asymmetric membrane with high flux. Previous investigation in the earlier sections showed that varying the overall geometrical parameter, for instance increasing the pore size of the structure, would improve flux. However, manufactured asymmetric membranes with large pored supports have reduced surface area and might not be mechanically stable. Therefore, the two-layer support system comprising of a thick (layer A) and a thin (layer B) support layer combined as the porous substrate have been studied for the optimization of the porous support of an asymmetric membrane.

The flux observed by varying the geometry of the single layered TC porous support presented in Figure 5.19 for the 90% relative flow performance of the membrane is comparably similar to that observed with this two-layer system. No further improvement in flux was observed for the two-layer system. However, when other factors like available surface area, robustness of the structure and ease of fabrication, are considered, the two-layer system is more favourable. This is due to the fact that the thin layer of the porous support has tailored geometrical properties (pore size, porosity, etc.). For instance, there is enough surface area for the surface reaction (recombination of the transported oxygen ions). In addition, it is easier to screen print a dense membrane on a porous support with smaller pore sizes than on supports with large pores. For supports with larger pores, in most cases, the membrane presses into the large pore and not on top of the structure. This is not desired as it reduces the quality and robustness of the fabricated membrane. Therefore, based on the present simulation results, the following suggestions are made with respect to optimizing the porous support of an asymmetric membrane:

1) The thickness of the thin layer should be in the range 10-30µm but should not be thicker than 30 µm or thinner than 10 µm. Larger thickness of the thin layer will make the thin layer rate limiting. If the thin layer is smaller than 10µm, it might be enveloped in the large pores of the thick layer.

2) The pore diameter of the thin layer can be in the range of 3 to 6.5 µm, while the pore diameter of the thick layer can be increased up to 40µm.

3) A reduced tortuosity factor of the thin layer is desired for both tape cast and inverse tape cast structures. Efforts should be made during manufacturing to properly orientate the pores in the flow direction in other to get the desired result. Use of elongated pore formers will always align in the plane of the coating, but, a field can be applied to align theses pore formers vertically. However, no studies have been done yet, to use of a field to align pore formers.

A flux comparable to the 90% relative flow performance of the membrane was observed at a 10 µm thickness of the thin layer for the two-layer support system, and at varying support ge-

ometry. This will aid the fabrication of an optimized porous support for asymmetric membranes.

Further studies are still needed at the interface of the two-layer system to properly investigate the surface exchange reactions. In addition, mechanical characterization and permeation measurement of this two-layer system is still need for the validation of the simulation.

5.9 One dimensional exact solution of BFM

The BFM has been reported in literature assuming an averaged pressure simplification [20]. However, in the present investigation, an in-depth study of the comparison between the deviation of the constant pressure simplifications and the exact solution was studied, and the implication/effect of each simplification on the observed flux presented.

5.9.1 Comparison of the oxygen flux from the simplifications

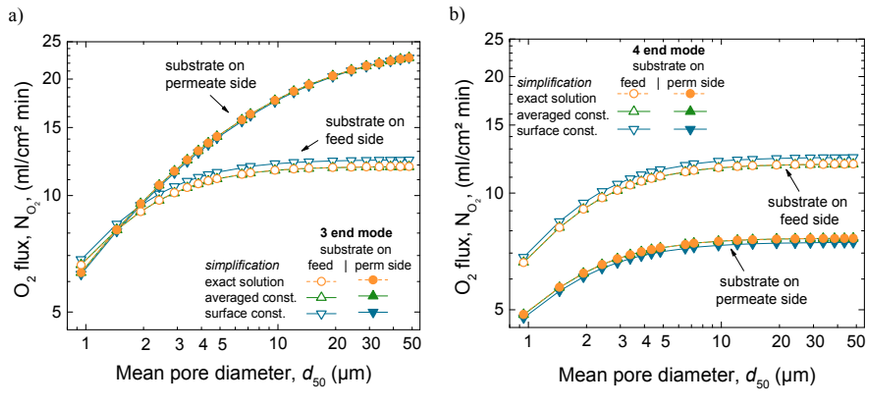

Figure 5.49: The dependence of flux on the pore diameter of the porous support for (a) 3-end, and (b) 4-end mode of transport, using air as feed gas for the exact solution and the different pressure simplifications (averaged constant and surface constant pressure) of the BFM.

A slight variation was observed between the different simplifications and the exact solution. These variations in flux at varying pore diameter of the porous support from 1 – 50 µm are evident from Figure 5.49. The configuration with the support at the feed side for the 3-end mode and the 4-end mode, are mixed gas transport. As such the mixed gas permeation equation of the BFM with the support on the feed side was employed for both cases. For 3-end mode transport process with the support at the permeate side, it is a single gas permeation through the porous support. The 1D analytical simulation of the surface constant and averaged constant pressure simplifications for BFM took 0.72 and 0.9 seconds, respectively. This is more than one order of magnitude faster than the exact solution. The flux observed for the exact solution and the simplifications for the transport modes were similar. A deviation in flux between the

exact solution and simplified solutions for mixed gas permeation through the porous support was observed.

The maximum deviations for the range of pore diameters considered between the surface constant simplification and the exact solution for the 3-end/4-end mode with the support at the feed side, the 3-end mode with the support at the permeate side, and 4-end mode with the support at the permeate side, are 3.9%, 1% and 2.5%, respectively. In contrast, the averaged constant pressure simplification, the maximum deviation for all transport modes and configurations in comparison to the exact solution was not more than 0.1%. For the case of the 3-end mode with the support on the permeate side there was zero deviation. The surface constant pressure simplification led to a larger deviation from the exact solution than the averaged constant pressure simplification. The surface constant pressure simplification is always off even at small pore diameters (a bit less than at higher pore diameters). Averaged constant pressure simplification, is always very close to the exact solution. Mixed gas permeation has several practical applications (e.g. membrane reactor); therefore, it is important to ascertain clearly how each of the simplifications can be compared to each other, and to the exact solution. Therefore, while varying the transport terms (the viscous flow, the binary and Knudsen diffusion) of the BFM, maps of the relative and the absolute difference between the exact and simplified solutions were made for a large range of transport operating parameter.

These maps as will be presented in Figure 5.50-Figure 5.53 show the effect of increasing or reducing each of the transport governing terms of the BFM for the different pressure simplifications in comparison to the exact solution. The map was studied to know which of the terms and at what configuration is more rate-limiting. These effects were studied by varying temperature, pore diameter and tortuosity factor. Except for the Knudsen diffusion, the transport equations (the viscous flow and the binary diffusion) of the BFM were modified for the different pressure simplifications. The Knudsen diffusion has a linear dependence on the mean pore diameter of the porous support, while the permeability is linearly dependent on the square of the mean pore diameter ($B_o \propto d_{pore}^2$) of the porous support. The binary diffusion shows no dependence on pore diameter. Air was the only feed gas used for the present evaluation. As such only the mixed gas permeation equations of the BFM were considered, except for the 3-end mode with the support at the permeate side for the evaluation of flux.

5.9.2 Relative and absolute flux differences between the different pressure simplifications and the exact solution

The exact solution describes more realistically the transport through the porous support and will be considered as a reference point for the other simplifications in the further calculations. The effect of varying the transport terms present in the BFM for the exact solution was mapped to the constant pressure simplifications. The absolute and the relative difference between the different pressure simplifications were investigated using:

$$Relative\ difference\ = \frac{N_{CP} - N_{ES}}{N_{ES}} \tag{0.3}$$

$$Absolute\ difference\ = N_{CP} - N_{ES} \tag{0.4}$$

Where N_{CP} and N_{ES} are the fluxes observed from the constant pressure simplifications (averaged constant and surface constant) and the exact solution, respectively. From Table 4.2, the three transport terms in the BFM that govern the overall transport through the porous support were introduced. The visualization of the 3 different transport terms of the BFM and the outcome of their variations in a 2-dimensional plot is not possible. Therefore, the transport terms (Table 4.2) were then combined to represent all effects. The ratio of the viscous flow transport to the binary diffusion transport of the BFM was shown as the vertical axis, while the ratio of the Knudsen diffusion to the binary diffusion transport was the horizontal axis. As a result, by varying the viscous flow, the Knudsen diffusion and the binary diffusion, the effect of the variation will be observed in the horizontal, vertical and diagonal axes, respectively. The binary diffusion transport term was used as common denominator since it is less dependent on the microstructure of the porous structure, and as such its effect can be observed/changed diagonally. The axes were combined in this way so that we have all the transport governing terms of the BFM in the map. For each map of the exact solution and the constant pressure simplifications, the dots show the trend of varying the pore diameter ranging from 10 nm to 50 µm with the present operating parameter. Also, for each pore diameter considered, the effect of temperature (the slightly diagonal lines) and tortuosity factor was evaluated. The tortuosity factor did not show any different effect on the maps when it was varied, because, all three transport terms are equally dependent on the tortuosity factor ($\propto \frac{1}{\kappa}$). Thus, its effect cancels out considering the ratios of the term used in the axes.

5.9.2.1 Support at the feed side

From Figure 5.50, no significant relative or absolute difference between the exact solution and the averaged constant pressure simplification was observed within typical operating conditions (pore diameter ≥ 1 µm and temperature ≥ 900°C). Within the temperature range considered for pore diameter above 1 µm, the averaged constant pressure simplification can be used in place of the exact solution. However, below 1 µm at reduced temperature, it shifts towards the undesired zone with deviations. The deviation is less than 0.06 ml/min cm² for explicitly given pore diameters even at room temperature. The zone with the highest deviation for the averaged constant pressure simplification cannot be reached under relevant physical parameters.

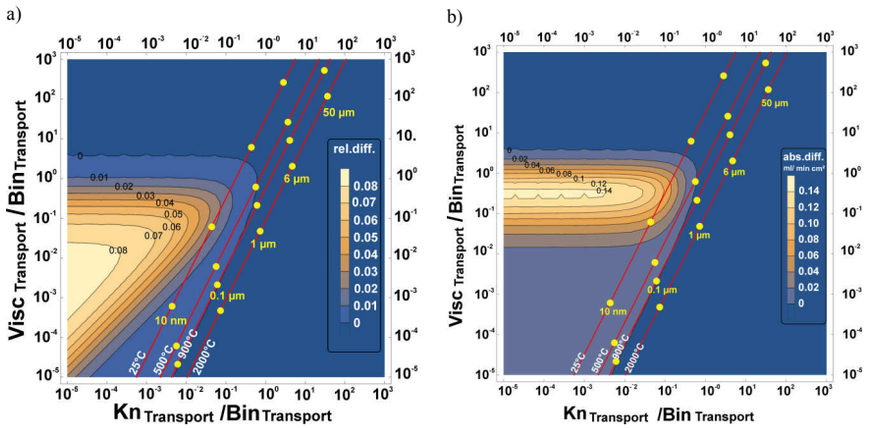

Figure 5.50: The a) relative and b) absolute difference between averaged constant pressure simplification and the exact solution for the 3-end mode and 4-end mode transport processes with the support at the feed side using air as feed gas. $Visc_{Transport}$, $Bin_{Transport}$, and $Kn_{Transport}$ represent viscous flow, binary diffusion and Knudsen diffusion transport, respectively. The red lines are the temperature increase from left to right, while the pore diameter increases upwards.

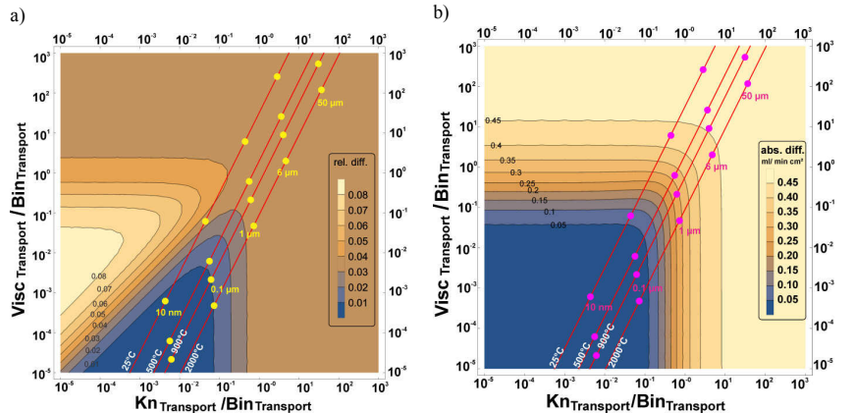

Figure 5.51: The a) relative and b) absolute difference between the surface constant pressure simplification and the exact solution for the 3-end mode and 4-end mode transport processes with the support at the feed side using air as feed gas. $Visc_{Transport}$, $Bin_{Transport}$, and $Kn_{Transport}$ represent viscous flow, binary diffusion and Knudsen diffusion transport, respectively. The red lines are the temperature increase from left to right, while the pore diameter increases going upwards.

The comparison between the exact solution and the surface constant pressure simplification shows a higher deviation than the averaged constant pressure simplification. The relative and absolute difference compared between the exact solution and surface constant pressure simplification (Figure 5.51) shows that the small pore diameters (10 nm – 0.1 µm) have the least deviations, although, they are not feasible for the microstructure of the porous structure needed. From Figure 5.51.a, Pore diameters between 0.1 µm and 1 µm have a dependence on temperature, while the rest of the pore diameter ranges considered are not dependent on temperature.

For pore diameters greater than 6.5 µm (Figure 5.51.b), the deviation in flux observed for the range of temperatures considered was 0.45 ml/min cm² but reduced to zero for 10 nm sized pores.

5.9.2.2 Support at the permeate side

Since only the mixed gas permeation was considered for the mapping of the different pressure simplifications, the map of the 3-end mode with the support at the permeate side will not be presented.

When the support is at the permeate side for the 4-end mode, the relative and the absolute difference between the averaged constant pressure simplification and the exact solution (Figure 5.52) shows that pore diameters smaller than 1 µm were the zones with least deviation for the operating conditions considered. This was found to be the case for temperatures greater than 900°C, but reducing the temperature below 900°C, introduces a deviation of 1%. The same deviation was observed for pore diameters greater than 6.5 µm pore diameter (as received microstructure) which is not more than 1%.

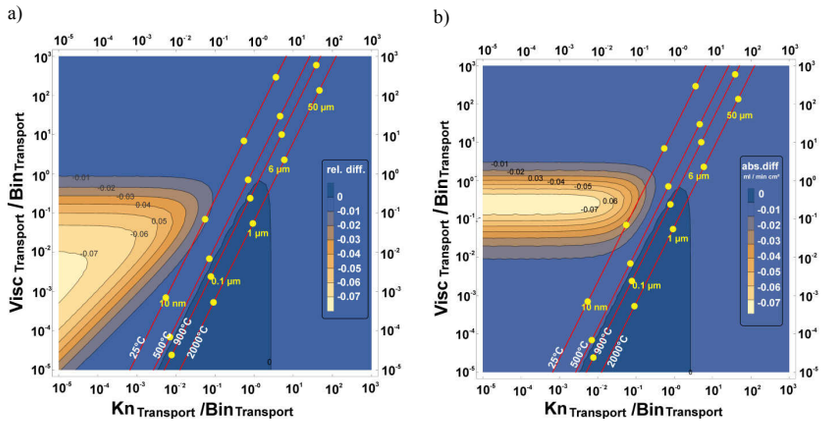

Figure 5.52: The a) relative and b) absolute difference between averaged constant pressure simplification and the exact solution for the 4-end mode transport process with the support at the permeate side using air as feed gas. $Visc_{Transport}$, $Bin_{Transport}$, and $Kn_{Transport}$ represent viscous flow, binary diffusion and Knudsen diffusion transport, respectively. The red lines are the temperature increase from left to right, while the pore diameter increases upwards.

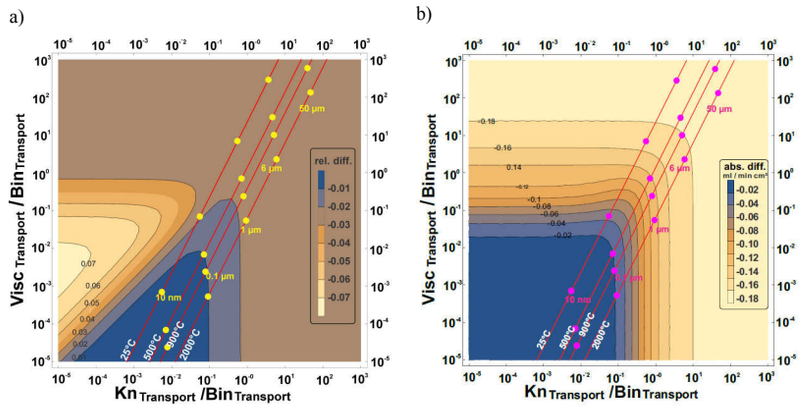

Figure 5.53: The a) relative and b) absolute difference between surface constant pressure simplification and the exact solution for the 4-end mode transport process with the support at the permeate side using air as feed gas. $Visc_{Transport}$, $Bin_{Transport}$, and $Kn_{Transport}$ represent viscous flow, binary diffusion and Knudsen diffusion transport, respectively. The red lines are the temperature increase from left to right, while the pore diameter increases upwards.

The relative difference between the exact solution and the surface constant pressure simplification (Figure 5.53) for the 4-end mode with the support on the permeate side, was observed to be less than ~ 2% for pore diameters less than 1 µm, but increases up to 3% for pore diameters greater than 1 µm. The absolute difference was observed to be ~0.18 ml/min cm² for pore diameters larger than 6.5 µm and reduced to 0.02 ml/min cm² for pore diameters less than 0.1 µm.

The large deviations observed for the surface constant pressure simplification when compared to the deviations observed for the averaged constant pressure, makes the latter a better replacement for the implementation of the binary friction model in 3D computational fluid dynamics calculations.

5.9.3 Conclusion

The optimization of the porous support for different technological applications to improve the overall flux has been an important topic of research. For example, the advancement in membrane technology will further be improved if the limitation introduced by the porous support of an asymmetric membrane is brought to the lowest minimal. The exact solution of the BFM gives a realistic description of the transport through the porous structure, but because of the pressure profiles it is complicated to be implemented in 3D. As a result, the BFM which is used for the description of the transport through the porous structure was simplified with respect to the pressure profiles. Surface constant and averaged constant pressure simplifications of the pressure profile through the porous support were presented and studied. Comparison between the exact and the simplified solutions was shown.

5.9. One dimensional exact solution of BFM

The surface constant and average constant pressure simplifications took 0.72 and 0.9 seconds for the 1D analytical evaluation of the flux through the membrane. This is more than one order of magnitude less computing time compared to the exact solution. In 3D CFD simulation, only the partial pressure at the membrane-support interface is evaluated for the constant pressure simplifications, as opposed to the exact solution where the partial pressure will be evaluated for every cell in the structure. For the pressure considered, the absolute difference between surface constant simplification and exact solution for the 3-end mode with the support on the feed side and 4-end mode with the support at the permeate side was 0.45 ml/min cm² and 0.18 ml/min cm², respectively, for a pore size diameter typical of porous support. This reduced with reduced pore diameter, but the small pore sizes are not feasible for the microstructure of the porous support. The relative difference for all transport modes did not increase more than 5%. For the averaged constant pressure simplification, a deviation of less than 1% from the exact solution for all transport modes and operating assembly, for a pore size diameter typical of porous support was observed. With the support on the feed side, the deviation reduced to zero for pore diameters above 1 μm and temperatures above 900°C. This makes the averaged pressure simplification more suitable and it is suggested instead of the exact solution for 3D implementation of the binary friction model.

6. Summary

The optimization of the porous support of an asymmetric membrane for different technological applications to improve the overall flux has been an important topic for researchers. The advancement in membrane technology will further be improved if the limitation introduced by the porous support of an asymmetric membrane is brought to the lowest minimal. This was the main goal of this work to optimize the porous support with respect to permeability to understand the underlying mechanism. In the present work, the transport through an asymmetric oxygen gas separation membrane was simulated in one dimension by applying the binary friction model (BFM) for the support together with a modified Wagner equation for the dense membrane. The developed model considers the transport through an asymmetric oxygen transport membrane using relevant parameters obtained from micro computed tomography and experimental data. Oxygen and air were used as feed gases. The 3-end mode and 4-end mode transport processes and different membrane orientations were considered in this study.

Anisotropic tailored support microstructure (elongated pores) will be favourable for mixed gas permeation through the support (e.g. membrane reactors). Whereas for single gas transport through the porous support, both isotropic and anisotropic scaled supports have comparable effects on flux.

In agreement with the Hagen Poiseuille law and the pore density, a relationship between the pore diameter and the permeability ($B_0 \propto d^2_{Pore}$) was found while varying the pore diameter of a tape cast support from 1-50 µm. Considering the two modes of transport processes (3-end and 4-end), increasing the pore diameter of the 0.9 mm thick porous support, while maintaining the operating conditions, increases the Knudsen diffusion and the permeability through the porous support and therefore the overall flux. At small pore diameters (< 10 µm), the tape cast support is rate-limiting, irrespective of the transport mode, the position or the thickness of the porous support. Increasing the pore diameter above 10 µm for the mixed gas transport through the porous support resulted in a negligible increase in flux under the conditions of the investigation. Reason is that the binary diffusion term of the BFM rate limits the transport. For the single gas transport through the porous support, the increase in flux was negligible, when the pore diameter was increased above 35 µm. The resistance or the rate-limiting effect of the porous support with a pore diameter above 35 µm for the 3-end mode (except when the support was at the feed side and using air as feed gas), is very small. As such, amongst the resistances in series (surface reaction, bulk transport, and porous support) that affect the flux through an asymmetric membrane, the support effect contributes to less than 10% limitation with respect to the relative flux. For mixed gas transport (3-end/4-end mode with the support on the feed side, using air as feed gas, the 4-end mode with the support on the permeate side using oxygen as feed gas) through the porous support, irrespective of the support position and using air as feed gas, the rate-limiting effect of the support was most pronounced. This shows that, for the 3-end mode, the dense membrane and the surface reactions display the dominant rate-limiting effect, while, for the 4-end mode, the rate limiting effect of the support is evident. Under same operat-

ing conditions, thinner supports with small pore diameter showed same flux as thicker supports with larger pore diameter. The found relationship can be used to optimize support's microstructure with regards to mechanical strength and permeability.

However, the one-dimensional numerical model is not sufficient for describing the transport through the porous support for large pores. The reason is that the model describes the transport as being dominated by binary diffusion, which is no longer the case at very large pore diameters where convection processes should occur. Therefore, a computational fluid dynamics simulation was carried out using a micro computed tomography data of an inverse tape cast structure. From the CFD simulation of the effect of gas flow through the support microstructure, it was observed that the freeze cast support had a higher flow velocity within the pores than the others (tape cast and inverse tape cast). This could be attributed to the alignment of the pores (slanted or inclined pores). The limiting part of the flux for the freeze cast is the nucleation zone, which constricts transport thereby limiting the observed flux. U-shaped pores were observed to be more favourable with respect to increase in permeated flux. This is because, two openings can provide a pressure difference which allows a continuous flow through the channel without eddy formation or stalling. Therefore, if samples with u-shaped pores or at least laterally connected with each other can be experimentally processed, it is assumed to be more favourable with respect to increase permeated flux. Freeze cast channel orientation should be adapted to the macroscopic flow field around the membrane. Channels should be aligned in the flow direction of the macroscopic flow field in order to take advantage of the conservation of momentum.

The comparison of the effect of support microstructures on flux was further studied by comparing asymmetric membranes manufactured from different processing routes; namely a sequential tape cast and the freeze cast sample. $Ba_{0.5}Sr_{0.5}(Co_{0.8}Fe_{0.2})_{0.97}Zr_{0.03}O_{3-\delta}$ (BSCF3Zr) ceramic powder was used for manufacturing these samples. The asymmetric membranes were manufactured with comparable support porosities, and the µXCT data acquired from these samples was used for the simulation studies. As the microstructure of the freeze cast sample appears very inhomogeneous, it was sliced into twelve sections across the support thickness, to have a better description of the graded nature of the structure. The tape cast structure was sectioned into four layers, since it is very uniform. In principle the hierarchical microstructure of the freeze cast support provides an enhanced gas transport capability. The nucleation side of the freeze cast support is normally used as the surface for screen-printing of the dense membrane, owing to ease of coating the porous layer with the thin dense membrane. However, particularly the transition zone near to the membrane, originated by the freezing process, strongly constrains the diffusivity by insufficient porosity and pore opening diameters. This made the flux from the tape cast to be similar to the flux from the freeze cast. Removal of three layers (~250 µm) from the constricting zone (the area with the onset of ice crystal nucleation) showed more than 10% improvement in flux. However, the surface area at the membrane-support interface should also be considered. The reason is that it is essential for sufficient oxygen exchange at the membrane-support interface.

In other to design an optimized support for an asymmetric membrane, a two-layer support system comprising of a thick (layer A) and a thin (layer B) support layer combined as the porous

substrate was proposed. The flux observed by varying the geometry of the single layered TC porous support for the 90% relative flow performance of the membrane is comparably similar to that observed with this two-layer system. Based on the simulation results, suggestion on the design of an optimized porous support was good.

The exact solution of the BFM gives a realistic description of the transport through the porous structure, but because of the pressure profiles it is complicated to be implemented in 3D. Reason is that a real microstructure has millions of cells, and each of these cells will have a partial pressure if the exact solution of the BFM would be employed for the description of the transport through it. The one-dimensional analytical simulation of the transport through the porous support using the exact solution in Mathematica takes approximately 30 seconds. This will increase greatly if one intends to make the same simulation in 3D using real microstructures. As a result, the BFM which is used for the description of the transport through the porous structure was simplified with respect to the pressure profiles. Surface constant and averaged constant pressure simplifications of the pressure profile through the porous support were presented and studied. Comparison between the exact and the simplified solutions was shown.

The 1D analytical evaluation of the flux through the membrane for the surface constant and average constant pressure simplifications took about the same time, which is more than one order of magnitude less computing time compared to the exact solution. For the pressure considered, the absolute difference between surface constant simplification and exact solution for the 3-end mode with the support on the feed side and 4-end mode with the support at the permeate side for a pore size diameter typical of porous support was large compare to the average constant pressure configuration. This reduced with reduced pore diameter, but the small pore sizes are not feasible for the microstructure of the porous support. The relative difference for all transport modes was almost 5%. For the averaged constant pressure simplification, a deviation of less than 1% from the exact solution for all transport modes and operating assembly, for a pore size diameter typical of porous support was observed. With the support on the feed side, the deviation reduced to zero for pore diameters above 1 µm and temperatures above 900°C. This makes the averaged pressure simplification more suitable and it is suggested instead of the exact solution for 3D implementation of the binary friction model.

7. Outlook

The pore size, porosity, and tortuosity of the porous support of an asymmetric membrane have a crucial impact on the overall performance which depends largely on the mode (3-end mode and 4-end mode) of operation and can limit the flux significantly. It is essential that the overall flow configuration in the experimental test stands are considered in the modelling, as the partial pressures significantly vary over the feed and permeate surface of the membrane assembly which cannot be taken into account by a simple 1D model. In addition, the surface diffusion processes / reactions need to be considered during the simulation of mesoporous interlayers. When all these factors are included in a multiscale simulation, it will be a valuable tool for the design of an optimal porous structure.

Therefore, the development of a Computational Fluid Dynamics (CFD) model for the overall macroscopic flow configuration including the Binary Friction model and the modified Wagner equation as a user defined function (UDF) in ANSYS Fluent is a future goal. This will entail writing a UDF for the Binary Friction Model in C for the implementation of a 3D macroscopic flow model, and for the implementation of a 3D microstructural flow model of the various diffusion contributions (which shall include not only viscous flow, but also binary, Knudsen and surface diffusion).

Finally, experimental validation of the simulated transport flow through the supported membranes should be performed using an existing test rig under various operational conditions.

8. Reference

[1] J.C. Boivin, C. Pirovano, G. Nowogrocki, G. Mairesse, P. Labrune, G. Lagrange, Electrode-electrolyte BIMEVOX system for moderate temperature oxygen separation, Solid State Ionics, 113 (1998) 639-651.

[2] P.N. Dyer, R.E. Richards, S.L. Russek, D.M. Taylor, Ion transport membrane technology for oxygen separation and syngas production, Solid State Ionics, 134 (2000) 21-33.

[3] S. Gopalan, Using ceramic mixed ionic and electronic conductors for gas separation, Jom-J Min Met Mat S, 54 (2002) 26-29.

[4] J.H. Tong, W.S. Yang, B.C. Zhu, R. Cai, Investigation of ideal zirconium-doped perovskite-type ceramic membrane materials for oxygen separation, J Membrane Sci, 203 (2002) 175-189.

[5] E. Robinson, Oxygen transport membranes for ultra-clean fuel production, Fuel Chemistry Division Reprints, 48 (2003) 347-349.

[6] J. Sunarso, S. Baumann, J.M. Serra, W.A. Meulenberg, S. Liu, Y.S. Lin, J.C.D. da Costa, Mixed ionic-electronic conducting (MIEC) ceramic-based membranes for oxygen separation, J Membrane Sci, 320 (2008) 13-41.

[7] X.L. Dong, W.Q. Jin, N.P. Xu, K. Li, Dense ceramic catalytic membranes and membrane reactors for energy and environmental applications, Chem Commun, 47 (2011) 10886-10902.

[8] N.H. Othman, Z.T. Wu, K. Li, An oxygen permeable membrane microreactor with an in-situ deposited $Bi_{1.5}Y_{0.3}Sm_{0.2}O_{3-\delta}$ catalyst for oxidative coupling of methane, J Membrane Sci, 488 (2015) 182-193.

[9] J. Kniep, Y.S. Lin, Partial Oxidation of Methane and Oxygen Permeation in $SrCoFeO_x$ Membrane Reactor with Different Catalysts, Ind Eng Chem Res, 50 (2011) 7941-7948.

[10] D. van Holt, E. Forster, M.E. Ivanova, W.A. Meulenberg, M. Muller, S. Baumann, R. Vassen, Ceramic materials for H_2 transport membranes applicable for gas separation under coal-gasification-related conditions, J Eur Ceram Soc, 34 (2014) 2381-2389.

[11] M. Czyperek, P. Zapp, H.J.M. Bouwmeester, M. Modigell, K. Ebert, I. Voigt, W.A. Meulenberg, L. Singheiser, D. Stover, Gas separation membranes for zero-emission fossil power plants: MEM-BRAIN, J Membrane Sci, 359 (2010) 149-159.

[12] M. Freemantle, Membranes for gas separation (vol 83, pg 55, 2005), Chem Eng News, 83 (2005) 39-39.

[13] Z.P. Shao, W.S. Yang, Y. Cong, H. Dong, J.H. Tong, G.X. Xiong, Investigation of the permeation behavior and stability of a $Ba_{0.5}Sr_{0.5}Co_{0.8}Fe_{0.2}O_{3-\delta}$ oxygen membrane, J Membrane Sci, 172 (2000) 177-188.

[14] S. Baumann, P. Niehoff, F. Schulze-Küppers, M. Ramasamy, W.A. Meulenberg, O. Guillon, (Invited) The Role of Solid-Gas Electrochemical Interfaces for Mixed Ionic Electronic Conducting Oxygen Transport Membranes, ECS Transactions, 66 (2015) 21-33.

[15] P. Niehoff, F. Schulze-Kuppers, S. Baumann, R. Vassen, H.P. Buchkremer, W.A. Meulenberg, Manufacturing and Performance of Supported BSCF-Membranes for Oxygen Separation, Developments in Strategic Materials and Computational Design V, (2015) 325-335.

[16] S. Baumann, J.M. Serra, M.P. Lobera, S. Escolastico, F. Schulze-Kuppers, W.A. Meulenberg, Ultrahigh oxygen permeation flux through supported $Ba_{0.5}Sr_{0.5}Co_{0.8}Fe_{0.2}O_{3-\delta}$ membranes, J Membrane Sci, 377 (2011) 198-205.

[17] H.J.M. Bouwmeester, A.J. Burggraaf, H.J.M. Bouwmeester, A.J. Burggraaf, Chapter 10 Dense ceramic membranes for oxygen separation, 1996.

[18] C. Wagner, Beitrag zur Theorie des Anlaufvorgangs, in: Zeitschrift für Physikalische Chemie, 1933, pp. 25.

[19] C. Wagner, Equations for transport in solid oxides and sulfides of transition metals, Prog Solid State Ch, 10 (1975) 3-16.

[20] H. Li, U. Schygulla, J. Hoffmann, P. Niehoff, K. Haas-Santo, R. Dittmeyer, Experimental and modeling study of gas transport through composite ceramic membranes, Chem Eng Sci, 108 (2014) 94-102.

[21] F.S.-K. M. Betz, S. Baumann, W. A. Meulenberg, D. Stöver, Supported Oxygen Transport Membranes for Oxyfuel Power Plants, Advances in Science and Technology, 72 (2010) 93-98.

[22] F. Bouville, E. Maire, S. Meille, B. Van de Moortele, A.J. Stevenson, S. Deville, Strong, tough and stiff bioinspired ceramics from brittle constituents, Nat Mater, 13 (2014) 508-514.

[23] Y. Chen, Y.X. Zhang, J. Baker, P. Majumdar, Z.B. Yang, M.F. Han, F.L. Chen, Hierarchically Oriented Macroporous Anode-Supported Solid Oxide Fuel Cell with Thin Ceria Electrolyte Film, Acs Appl Mater Inter, 6 (2014) 5130-5136.

[24] S. Deville, Freeze-casting of porous ceramics: A review of current achievements and issues, Adv Eng Mater, 10 (2008) 155-169.

[25] S. Deville, Freeze-Casting of Porous Biomaterials: Structure, Properties and Opportunities, Materials, 3 (2010) 1913-1927.

[26] C. Gaudillere, J. Garcia-Fayos, J.M. Serra, Enhancing oxygen permeation through hierarchically-structured perovskite membranes elaborated by freeze-casting, J Mater Chem A, 2 (2014) 3828-3833.

[27] T. Waschkies, R. Oberacker, M.J. Hoffmann, Control of Lamellae Spacing During Freeze Casting of Ceramics Using Double-Side Cooling as a Novel Processing Route, J Am Ceram Soc, 92 (2009) S79-S84.

[28] S.Y. Cheng, H. Huang, S. Ovtar, S.B. Simonsen, M. Chen, W. Zhang, M. Sogaard, A. Kaiser, P.V. Hendriksen, C.S. Chen, High-Performance Microchanneled Asymmetric $Gd_{0.1}Ce_{0.9}O_{1.95-\delta}$ –$La_{0.6}Sr_{0.4}FeO_{3-\delta}$ -Based Membranes for Oxygen Separation, Acs Appl Mater Inter, 8 (2016) 4548-4560.

[29] H. Huang, S.Y. Cheng, J.F. Gao, C.S. Chen, J.X. Yi, Phase-inversion tape-casting preparation and significant performance enhancement of $Ce_{0.9}Gd_{0.1}O_{1.95}$-$La_{0.6}Sr_{0.4}Co_{0.2}Fe_{0.8}O_{3-\delta}$ dual-phase asymmetric membrane for oxygen separation, Mater Lett, 137 (2014) 245-248.

[30] F. Schulze-Küppers, S. Baumann, W.A. Meulenberg, D. Stover, H.P. Buchkremer, Manufacturing and performance of advanced supported $Ba_{0.5}Sr_{0.5}Co_{0.8}Fe_{0.2}O_{3-\delta}$ (BSCF) oxygen transport membranes, J Membrane Sci, 433 (2013) 121-125.

[31] F. Schulze-Küppers, S. Baumann, F. Tietz, H.J.M. Bouwmeester, W.A. Meulenberg, Towards the fabrication of $La_{0.98-x}Sr_xCo_{0.2}Fe_{0.8}O_{3-\delta}$ perovskite-type oxygen transport membranes, J Eur Ceram Soc, 34 (2014) 3741-3748.

[32] P.J.A.M. Kerkhof, A modified Maxwell-Stefan model for transport through inert membranes: the binary friction model, The Chemical Engineering Journal and the Biochemical Engineering Journal, 64 (1996) 319-343.

[33] J. Emsley, Nature's building blocks: an A–Z guide to the elements, Oxford University Press UK, 2001.

[34] Y. He, X. Zhu, Q. Li, W. Yang, Perovskite oxide absorbents for oxygen separation, Aiche J, 55 (2009).

[35] Q.Y. Jiang, S. Faraji, D.A. Slade, S.M. Stagg-Williams, A Review of Mixed Ionic and Electronic Conducting Ceramic Membranes as Oxygen Sources for High-Temperature Reactors, Membr Sci Tech Ser, 14 (2011) 235-273.

[36] W. Wang, S.P. Wang, X.B. Ma, J.L. Gong, Recent advances in catalytic hydrogenation of carbon dioxide, Chem Soc Rev, 40 (2011) 3703-3727.

[37] W. Deibert, M.E. Ivanova, S. Baumann, O. Guillon, W.A. Meulenberg, Ion-conducting ceramic membrane reactors for high-temperature applications, J Membrane Sci, 543 (2017) 79-97.

[38] B. Hu, C. Guild, S.L. Suib, Thermal, electrochemical, and photochemical conversion of CO2 to fuels and value-added products, J Co2 Util, 1 (2013) 18-27.

[39] S.G. Jadhav, P.D. Vaidya, B.M. Bhanage, J.B. Joshi, Catalytic carbon dioxide hydrogenation to methanol: A review of recent studies, Chem Eng Res Des, 92 (2014) 2557-2567.

[40] O. Czuprat, H.Q. Jiang, Catalytic Membrane Reactors - Chemical Upgrading and Pollution Control, Chem-Ing-Tech, 83 (2011) 2219-2228.

[41] S.M. Hashim, A.R. Mohamed, S. Bhatia, Catalytic inorganic membrane reactors: present research and future prospects, Rev Chem Eng, 27 (2011) 157-178.

[42] H. Dong, Z.P. Shao, G.X. Xiong, J.H. Tong, S.S. Sheng, W.S. Yang, Investigation on POM reaction in a new perovskite membrane reactor, Catal Today, 67 (2001) 3-13.

[43] M.S. Fan, A.Z. Abdullah, S. Bhatia, Catalytic Technology for Carbon Dioxide Reforming of Methane to Synthesis Gas, Chemcatchem, 1 (2009) 192-208.

[44] S. Faraji, K.J. Nordheden, S.M. Stagg-Williams, The Interaction Between $SrFeCo_{0.5}O_x$ Ceramic Membranes and $Pt/CeZrO_2$ During Syngas Production from Methane, Catal Lett, 131 (2009) 114-121.

[45] M. Ikeguchi, T. Mimura, Y. Sekine, E. Kikuchi, M. Matsukata, Reaction and oxygen permeation studies in $Sm_{0.4}Ba_{0.6}Fe_{0.8}Co_{0.2}O_{3-\delta}$ membrane reactor for partial oxidation of methane to syngas, Appl Catal a-Gen, 290 (2005) 212-220.

[46] J.M. Kim, G.J. Hwang, S.H. Lee, C.S. Park, J.W. Kim, Y.H. Kim, Properties of oxygen permeation and partial oxidation of methane in $La_{0.6}Sr_{0.4}CoO_{3-\delta}$ (LSC)-$La_{0.7}Sr_{0.3}Ga_{0.6}Fe_{0.4}O_{3-\delta}$ (LSGF) membrane, J Membrane Sci, 250 (2005) 11-16.

[47] Q.M. Li, X.F. Zhu, Y.F. He, W.S. Yang, Partial oxidation of methane in $BaCe_{0.1}Co_{0.4}Fe_{0.5}O_{3-\delta}$ membrane reactor, Catal Today, 149 (2010) 185-190.

[48] D.A. Slade, A.M. Duncan, K.J. Nordheden, S.M. Stagg-Williams, Mixed-conducting oxygen permeable ceramic membranes for the carbon dioxide reforming of methane, Green Chem, 9 (2007) 577-581.

[49] H.H. Wang, Y. Cong, W.S. Yang, Partial oxidation of ethane to syngas in an oxygen-permeable membrane reactor, J Membrane Sci, 209 (2002) 143-152.

[50] H.H. Wang, Y. Cong, W.S. Yang, Investigation on the partial oxidation of methane to syngas in a tubular $Ba_{0.5}Sr_{0.5}Co_{0.8}Fe_{0.2}O_{3-\delta}$ membrane reactor, Catal Today, 82 (2003) 157-166.

[51] Y.W. Zhang, Q. Li, P.J. Shen, Y. Liu, Z.B. Yang, W.Z. Ding, X.G. Lu, Hydrogen amplification of coke oven gas by reforming of methane in a ceramic membrane reactor, Int J Hydrogen Energ, 33 (2008) 3311-3319.

[52] Z.P. Shao, H. Dong, G.X. Xiong, Y. Gong, W.S. Yang, Performance of a mixed-conducting ceramic membrane reactor with high oxygen permeability for methane conversion, J Membrane Sci, 183 (2001) 181-192.

[53] C.Y. Tsai, A.G. Dixon, W.R. Moser, Y.H. Ma, Dense perovskite membrane reactors for partial oxidation of methane to syngas, Aiche J, 43 (1997) 2741-2750.

[54] X. Yin, L. Hong, Z.L. Liu, Asymmetric tubular oxygen-permeable ceramic membrane reactor for partial oxidation of methane, J Phys Chem C, 111 (2007) 9194-9202.

[55] P.Y. Zeng, Z.H. Chen, W. Zhou, H.X. Gu, Z.P. Shao, S.M. Liu, Re-evaluation of $Ba_{0.5}Sr_{0.5}Co_{0.8}Fe_{0.2}O_{3-\delta}$ perovskite as oxygen semi-permeable membrane, J Membrane Sci, 291 (2007) 148-156.

[56] B. Cales, J.F. Baumard, Mixed Conduction and Defect Structure of ZrO_2-CeO_2-Y_2O_3 Solid-Solutions, J Electrochem Soc, 131 (1984) 2407-2413.

[57] Y. Teraoka, H.M. Zhang, S. Furukawa, N. Yamazoe, Oxygen Permeation through Perovskite-Type Oxides, Chem Lett, (1985) 1743-1746.

[58] T. Armstrong, F. Prado, A. Manthiram, Synthesis, crystal chemistry, and oxygen permeation properties of $LaSr_3Fe_{3-x}Co_xO_{10}$ ($0 <= x <= 1.5$), Solid State Ionics, 140 (2001) 89-96.

[59] U. Balachandran, J.T. Dusek, P.S. Maiya, B. Ma, R.L. Mieville, M.S. Kleefisch, C.A. Udovich, Ceramic membrane reactor for converting methane to syngas, Catal Today, 36 (1997) 265-272.

[60] D.M. Bochkov, V.V. Kharton, A.V. Kovalevsky, A.P. Viskup, E.N. Naumovich, Oxygen permeability of $La_2Cu(Co)O_{4+\delta}$ solid solutions, Solid State Ionics, 120 (1999) 281-288.

[61] M.A. Green, A. Ho-Baillie, H.J. Snaith, The emergence of perovskite solar cells, Nat Photonics, 8 (2014) 506-514.

[62] Y.Y. Liu, X.Y. Tan, K. Li, Mixed conducting ceramics for catalytic membrane processing, Catal Rev, 48 (2006) 145-198.

[63] B.C.H. Steele, Ceramic ion conducting membranes, Curr Opin Solid St M, 1 (1996) 684-691.

[64] W.S. Yang, H.H. Wang, X.F. Zhu, L.W. Lin, Development and application of oxygen permeable membrane in selective oxidation of light alkanes, Top Catal, 35 (2005) 155-167.

[65] A.S. Bhalla, R. Guo, R. Roy, The perovskite structure – a review of its role in ceramic science and technology, Material Research Innovations, 4 (2000) 3-26.

[66] E.P. Setyaningsih, M. Machfudzoh, W.P. Utomo, H. Fansuri, Preparation of $CaTiO_3$ Asymmetric Membranes Using Polyetherimide as Binder Polymer, Indones J Chem, 16 (2016) 20-24.

[67] F.S. Galasso, Structures, properties and Preparations of Perovskite-type Compounds, First edition ed., Pergamon Press Inc., Oxford, 1969.

[68] H.D. Megaw, Crystal Structure of Double Oxides of the Perovskite Type, P Phys Soc Lond, 58 (1946) 133-&.

[69] T.F.W.B. V. M. Goldschmidt, G. Lunde, and W. Zachariasen, Geochemische Verteilungsgesetze der Elemente – VII. Die Gesetze der Krystallochemie, Skr. Nor. Vidensk.-Akad., [Kl.] I. Mat.-Naturvidensk. Kl; Oslo, 2 (1926) 1-117.

[70] J.W. Stevenson, T.R. Armstrong, D.E. McCready, I.R. Pederson, W.J. Weber, Processing and electrical properties of alkaline earth-doped lanthanum gallate, J Electrochem Soc, 144 (1997) 3613-3620.

[71] F. Schulze-Küppers, Entwicklung Geträgerter $Ba_{0.5}S_{r0.5}Co_{0.8}Fe_{0.2}O_{3-\delta}$ Sauerstoff-Permeationsmembranen, in: Forschungszentrum, Zentralbibliothek, University of Bochum, Jülich.

[72] A.J. Jacobson, S. Kim, A. Medina, Y.L. Yang, B. Abeles, Dense oxide membranes for oxygen separation and methane conversion, Recent Advances in Catalytic Materials, 497 (1998) 29-34.

[73] A. Leo, S.M. Liu, J.C.D. da Costa, Development of mixed conducting membranes for clean coal energy delivery, Int J Greenh Gas Con, 3 (2009) 357-367.

[74] W. Zhou, R. Ran, Z.P. Shao, Progress in understanding and development of $Ba_{0.5}Sr_{0.5}Co_{0.8}Fe_{0.2}O_{3-\delta}$ -based cathodes for intermediate-temperature solid-oxide fuel cells: A review, J Power Sources, 192 (2009) 231-246.

[75] R.L. Cook, R.C. Macduff, A.F. Sammells, Perovskite Solid Electrolytes for Intermediate Temperature Solid Oxide Fuel-Cells, J Electrochem Soc, 137 (1990) 3309-3310.

[76] R.L. Cook, A.F. Sammells, On the Systematic Selection of Perovskite Solid Electrolytes for Intermediate Temperature Fuel-Cells, Solid State Ionics, 45 (1991) 311-321.

[77] W.Y. J. Dong, Methods for selection perovskite-type oxides used as mixed-conducting membranes for oxygen separation, Membrane Science Technology 23 (2003) 33-42.

[78] F.A. Kroger, H.J. Vink, Relations between the Concentrations of Imperfections in Crystalline Solids, Solid State Phys, 3 (1956) 307-435.

[79] S.J. Xu, W.J. Thomson, Oxygen permeation rates through ion-conducting perovskite membranes, Chem Eng Sci, 54 (1999) 3839-3850.

[80] H.J.M. Bouwmeester, H. Kruidhof, A.J. Burggraaf, Importance of the Surface Exchange Kinetics as rate-limiting Step in Oxygen Permeation through Mixed-Conducting Oxides, Solid State Ionics, 72 (1994) 185-194.

[81] L. Onsager, Reciprocal Relations in Irreversible Processes. I, Phys Rev, 37 (1931) 405-426.

[82] R.A. Mckee, A Generalization of the Nernst-Einstein Equation for Self-Diffusion in High Defect Concentration Solids, Solid State Ionics, 5 (1981) 133-136.

[83] T. Kida, S. Ninomiya, K. Watanabe, N. Yamazoe, K. Shimanoe, High Oxygen Permeation in $Ba_{0.95}La_{0.05}FeO_{3-\delta}$ Membranes with Surface Modification, Acs Appl Mater Inter, 2 (2010) 2849-2853.

[84] H. Kusaba, Y. Shibata, K. Sasaki, Y. Teraoka, Surface effect on oxygen permeation through dense membrane of mixed-conductive LSCF perovskite-type oxide, Solid State Ionics, 177 (2006) 2249-2253.

[85] S. Baumann, W.A. Meulenberg, H.P. Buchkremer, Manufacturing strategies for asymmetric ceramic membranes for efficient separation of oxygen from air, J Eur Ceram Soc, 33 (2013) 1251-1261.

[86] W. Ito, T. Nagai, T. Sakon, Oxygen separation from compressed air using a mixed conducting perovskite-type oxide membrane, Solid State Ionics, 178 (2007) 809-816.

[87] X.J. Liu, H. Wu, Z.Y. He, J. Gao, X. Meng, T. Luo, C.S. Chen, Z.L. Zhan, Hebb-Wagner polarization assessment of enhanced oxygen permeability for surface modified oxygen transport membranes, Int J Hydrogen Energ, 42 (2017) 18410-18416.

[88] S.M. Murphy, D.A. Slade, K.J. Nordheden, S.M. Stagg-Williams, Increasing oxygen flux through a dense oxygen permeable membrane by photolithographic patterning of platinum, J Membrane Sci, 277 (2006) 94-98.

[89] Y. Qiang, Z. Qiang, L. Rong, Preparation and Oxygen Permeability of $BaCo_{0.7}Fe_{0.2}Nb_{0.1}O_{3-\delta}$ Membrane Modified by $Ce_{0.8}Y_{0.2}O_{2-\delta}$ Porous Layer on the Air Side, J Nanomater, (2013).

[90] X.Y. Tan, Z.G. Wang, H. Liu, S.M. Liu, Enhancement of oxygen permeation through $La_{0.6}Sr_{0.4}Co_{0.2}Fe_{0.8}O_{3-\delta}$ hollow fibre membranes by surface modifications, J Membrane Sci, 324 (2008) 128-135.

[91] Y. Teraoka, Y. Honbe, J. Ishii, H. Furukawa, I. Moriguchi, Catalytic effects in oxygen permeation through mixed-conductive LSCF perovskite membranes, Solid State Ionics, 152 (2002) 681-687.

[92] K. Gerdes, D. Luss, Oxygen flux increases through MIEC membranes by enhanced surface exchange, Aiche J, 53 (2007) 1389-1391.

[93] V.V. Kharton, A.V. Kovalevsky, A.P. Viskup, F.M. Figueiredo, J.R. Frade, A.A. Yaremchenko, E.N. Naumovich, Faradaic efficiency and oxygen permeability of $S_{r0.97}Ti_{0.60}Fe_{0.40}O_{3-\delta}$ perovskite, Solid State Ionics, 128 (2000) 117-130.

[94] A. Leo, S. Smart, S. Liu, J.C.D. da Costa, High performance perovskite hollow fibres for oxygen separation, J Membrane Sci, 368 (2011) 64-68.

[95] P. Niehoff, S. Baumann, F. Schulze-Kuppers, R.S. Bradley, I. Shapiro, W.A. Meulenberg, P.J. Withers, R. Vassen, Oxygen transport through supported $Ba_{0.5}Sr_{0.5}Co_{0.8}Fe_{0.2}O_{3-\delta}$ membranes, Sep Purif Technol, 121 (2014) 60-67.

[96] C.H. Chen, H.J.M. Bouwmeester, H. Kruidhof, J.E. tenElshof, A.J. Burggraaf, Fabrication of $La_{1-x}Sr_xCoO_{3-\delta}$ thin layers on porous supports by a polymeric sol-gel process, J Mater Chem, 6 (1996) 815-819.

[97] W.Q. Jin, S.G. Li, P. Huang, N.P. Xu, J. Shi, Preparation of an asymmetric perovskite-type membrane and its oxygen permeability, J Membrane Sci, 185 (2001) 237-243.

[98] A.V. Kovalevsky, A.A. Yaremchenko, V.A. Kolotygin, A.L. Shaula, V.V. Kharton, F.M.M. Snijkers, A. Buekenhoudt, J.R. Frade, E.N. Naumovich, Processing and oxygen permeation studies of asymmetric multilayer $Ba_{0.5}Sr_{0.5}Co_{0.8}Fe_{0.2}O_{3-\delta}$ membranes, J Membrane Sci, 380 (2011) 68-80.

[99] U.V. Unije, R. Mucke, S. Baumann, O. Guillon, Comparison of the Simplification of the Pressure Profiles Solving the Binary Friction Model for Asymmetric Membranes, Membranes, 7 (2017).

[100] Y. Ohzawa, K. Nomura, K. Sugiyama, Relation between porosity and pore size or pressure drop of fibrous SiC filter prepared from carbonized cellulose-powder preforms, Mat Sci Eng a-Struct, 255 (1998) 33-38.

[101] R.L. Coble, W.D. Kingery, Effect of Porosity on Physical Properties of Sintered Alumina, J Am Ceram Soc, 39 (1956) 377-385.

[102] F. Schulze-Küppers, U.V. Unije, H. Blank, M. Balaguer, S. Baumann, R. Mücke, W.A. Meulenberg, Comparison of freeze-dried and tape-cast support microstructure on high-flux oxygen transport membrane performance, J Membrane Sci, 564 (2018) 218-226.

[103] O. Levenspiel, Engineering Flow and Heat Exchange, 1 ed., Springer US, 1984.

[104] D.D. Do, Adsoprtion Analysis: Equilibria and kinetics, Imperial College Press, 1998.

[105] L.M. Abriola, C.S. Fen, H.W. Reeves, Numerical-Simulation of Unsteady Organic Vapor Transport in Porous-Media Using the Dusty Gas-Model, Subsurface Contamination by Immiscible Fluids, (1992) 195-202.

[106] A.L. Baehr, C.J. Bruell, Application of the Stefan-Maxwell equations to determine limitations of Fick's law when modelling organic vapor transport in sand colums, Water Resour Res, 26 (1990) 1155-1163.

[107] D.C. Thorstenson, D.W. Pollock, Gas-Transport in Unsaturated Zones - Multicomponent Systems and the Adequacy of Fick Laws, Water Resour Res, 25 (1989) 477-507.

[108] R.B. Bird, W.E. Stewart, and E.N. Lightfoot, Transport Phenomena, John Wiley and Sons, Inc., New York, NY, 1960.

[109] D.B. Jaynes, A.S. Rogowski, Applicability of Ficks Law to Gas-Diffusion, Soil Sci Soc Am J, 47 (1983) 425-430.

[110] K. Pruess, TOUGH2 - A General-Purpose Numerical Simulator for Mult4phase Fluid and Heat Flow, Lawrence Berkeley Lab., CA LBL-29400 (1991).

[111] I. Evans, R. B., GM. Watson, and EA. Mason, Gas Diffusion in Porous Media II, Effect of pressure gradients, J Chem Phys, 36 (1962a) 1894- 1902.

[112] I.R.B. Evans, G.M Watson and EA. Mason, Gas Diffusion in Porous media at Uniform pressure, J Chem Phys, 35 (1961) 2076 - 2083.

[113] E.A. Mason, R.B. Evans, III, and G.M. Watson, Gaseous diffusion in porous media III. Thermal Transpiration, J Chem Phys, 38 (1963) 1808-1826.

[114] E.A. Mason, and A.P. Malinauskas, Gaseous diffusion in porous media. IV. Thermal diffusion, J Chem Phys, 41 (1964) 3815.

[115] E.A. Mason, and A.P. Malinauskas, Gas Transport in Porous Media: The DustyGas model, Elsevier Science Publishers, New York, 1983.

[116] R.E. Cunningham, Diffusion in gases and porous media / R.E. Cunningham and R.J.J. Williams, Plenum Press, New York, 1980.

[117] E.N. Lightfoot, Transport phenomena and living systems : biomedical aspects of momentum and mass transport, John Wiley and Sons, New York, 1974.

[118] P.J.A.M. Kerkhof, M.A.M. Geboers, K.J. Ptasinski, On the isothermal binary mass transport in a single pore, Chem Eng J, 83 (2001) 107-121.

[119] P. Niehoff, Entwicklung planarer $Ba_{0,5}Sr_{0,5}Co_{0,8}Fe_{0,2}O_{3-\delta}$-Membranmodule zur Sauerstoffabtrennung und Analyse ihres Transportverhaltens, Forschungszentrum Jülich GmbH, Zentralbibliothek, Jülich, 2015.

[120] R.K. Ross Taylor, Multicomponent of Mass Transfer, John Wiley, Canada, 1993.

[121] J.C. Maxwell, Scientific Paper, Dover publication, New York, 1965.

[122] J.M.P. R.C. Reid, T.K. Sherwood, The properties of gases and liquids, 3rd ed., McGraw-Hill, New York, 1977.

[123] L.A. Feldkamp, L.C. Davis, J.W. Kress, Practical Cone-Beam Algorithm, J Opt Soc Am A, 1 (1984) 612-619.

[124] P.C. Carman, Flow of gases through porous media, Academic Press Inc., New York, 1956.

[125] N. Epstein, On Tortuosity and the Tortuosity Factor in Flow and Diffusion through Porous-Media, Chem Eng Sci, 44 (1989) 777-779.

[126] C. P.C, Fluid flow through a granular bed, Transactions of the Institution of Chemical Engineers, 15 (1937) 155-166.

[127] A.E. Scheidegger, The physics of flow through porous media, University of Toronto press, Toronto, 1974.

[128] E.L. Cussler, Diffusion: mass transfer in fluid systems, 3rd ed., Cambridge University Press, 2009.

[129] A. ANSYS®, Academic Research, Release 16.0, ANSYS Fluent in ANSYS Workbench User's Guide ANSYS, Inc., Canonsburg, PA.

[130] P.W.J. Glover, Petrophysique, in, Département de Géologie et de Génie Géologique Université Laval, CANADA, pp. 30, - ch33, .

[131] X.F. Chang, C. Zhang, X.L. Dong, C. Yang, W.Q. Jin, N.P. Xu, Experimental and modeling study of oxygen permeation modes for asymmetric mixed-conducting membranes, J Membrane Sci, 322 (2008) 429-435.

[132] U. Unije, R. Mücke, P. Niehoff, S. Baumann, R. Vaßen, O. Guillon, Simulation of the effect of the porous support on flux through an asymmetric oxygen transport membrane, J Membrane Sci, 524 (2017) 334-343.

[133] E.A. Mason, L.F. del Castillo, The role of viscous flow in theories of membrane transport, J Membrane Sci, 23 (1985) 199-220.

[134] M. Coroneo, G. Montante, M.G. Baschetti, A. Paglianti, CFD modelling of inorganic membrane modules for gas mixture separation, Chem Eng Sci, 64 (2009) 1085-1094.

[135] R. Ghidossi, D. Veyret, P. Moulin, Computational fluid dynamics applied to membranes: State of the art and opportunities, Chem Eng Process, 45 (2006) 437-454.

[136] H. Takaba, S. Nakao, Computational fluid dynamics study on concentration polarization in H-2/CO separation membranes, J Membrane Sci, 249 (2005) 83-88.

[137] P. Colombo, In praise of pores, Science, (2008) 381-383.

9. Acknowledgement

It still feels like yesterday when I started my doctoral research at the Institute of Energy and Climate Research (IEK-1 - Material Synthesis and Production Processes), Forschungszentrum Jülich. Over these three years, time, energy, concentration, strength, sleepless nights, etc. have been invested to make this work a success. At this point, I would like to express my gratitude to all the people who have supported me or contributed to the completion of this my research work.

Firstly, I want to appreciate the Helmholtz Interdisciplinary Doctoral Training in Energy and Climate Research (HITEC) partly funding my research work as a HITEC fellow.

My sincere thanks to my head of Institute Prof. Dr. Olivier Guillon who was also my doctoral supervisor for giving me the opportunity to apply for the HITEC fellow funding, for his excellent scientific support of my work, for helping me with his wealth of experience and knowledge and ensuring that I met the requirements for obtaining the Doctor of Engineering.

Many special thanks, to my scientific supervisor Dr. Robert Mücke for his unflagging dedication and support. I greatly appreciate the modeling skills and intelligence that God endowed you with, and I am thankful to God for giving me the opportunity to work with you, because I really learnt a lot. Thank you.

Furthermore, I thank Univ.-Prof. Dr.-Ing. Herbert Pfeifer for accepting to be my second examiner and for his timely correction of this work and Univ.-Prof. Dr. rer. Nat. Rainer Teller for accepting the chairmanship of the examination committee.

Many thanks to Prof. Dr. Wilhelm Albert Meulenberg for his great support and advice, as well as to Prof. Dr. Henny Bouwmeester for being my external mentor and for his availability for my scientific discussions. A big thanks to Dr. Stefan Baumann for willingly taking up the role of an unofficial experiment related supervisor and Dr. Falk Schulze-Küppers. Both have always had an open ear for my questions and have contributed significantly to the success of this work with their stimulating discussions. To the entire membrane group, I say a big thank you especially my former colleague Patrick Niehoff and Kai Wilkner.

I also thank the colleagues Søren Bredmose Simonsen, Shiyang Cheng, and Peter Vang Hendriksen, from Denmark Technical University (DTU) for providing me with the CT data for my simulation.

Mrs. Vicky Tirtey, Mr. Stefan Weitz, and Mrs. Yvonne Lichtenfeld for the organization and answering of all administrative questions, and Mrs. Moitroux, Hiltrud for the prompt printing. I want to thank my office mate and modelling group members Chen Cao, Dr. Panpan Wang, Dr. Joao Gustavo Pereira da Silva, Al-Jaljouli, Fadi Hassan, and Rainer Kriecher for a pleasant working atmosphere.

With a grateful heart I want to specially appreciate my mother Mrs Mma Victoria Unije for her love, and the strength of character of being both parents for my siblings and I after the death of our father, I love you Mummy. I want to thank my brother Barr. Obinna Unije, Rev. Fr. Newman Ikem Egbo, Franklin Odoemenam, and my sisters Amaka Vivian Unije, Gloria Nnenna Unije and most especially Chidimma Nuela Unije who took care of me towards the last

months of my work, notwithstanding she had my little nephew Franz to take care of. I heart you all.

David Chinonye Ukwungwu, Ines Mücke, Retti Singh, Dr. Rafael Silva, Dr. Juliane Franciele Nonemacher, Dr. Jan Bergholz, Dr. Hans Peter Buchkremer, Bukas Okey Amechi, Eno Chukwudindu, Blessing Nwosu, Bernice Dauda, Eziama Ubachukwu, Chioma Aneke, and Nkili Anammah, who were at my side for questions, support, discussions and lively exchanges. Thank you all. It was more than a pleasure.

Above all, I thank God Almighty for all always being there for me.

Schriften des Forschungszentrums Jülich
Reihe Energie & Umwelt / Energy & Environment

Band / Volume 449
Projektbericht Adelheid – aus dem Labor heraus in die Lüfte
R. Peters, J. Pasel, R. C. Samsun, A. Tschauder, C. Wiethege, F. Scharf, D. Stolten (2018), xxi, 321 pp
ISBN: 978-3-95806-378-5

Band / Volume 450
Microstructure and Thermomechanical Properties of $SrTi_{1-x}Fe_xO_{3-\delta}$ Oxygen Transport Membranes and Supports
R. Oliveira Silva (2019), vi, 148 pp
ISBN: 978-3-95806-381-5

Band / Volume 451
Sodium Ion Conducting Ceramics for Sodium Ion Batteries
S. Naqash (2019), vii, 134 pp
ISBN: 978-3-95806-382-2

Band / Volume 452
Quantitative Analyse der Trocknungsverläufe von Katalysatordispersionen
F. Scheepers (2019), VIII, 191 pp
ISBN: 978-3-95806-384-6

Band / Volume 453
Neue Optionen für einen wirtschaftlichen Betrieb von Wasserstoffzügen durch Nutzung der LOHC-Technologie?
P. Wasserscheid, T. Grube, D. Sternfeld, M. Essl, M. Robinius, D. Stolten (2019), II, 88 pp
ISBN: 978-3-95806-386-0

Band / Volume 454
Reformierung von BtL-Kraftstoffen für die HT-PEFC in luftfahrttechnischen Systemen
C. Wilbrand (2019), IV, 312 pp
ISBN: 978-3-95806-387-7

Band / Volume 455
Entwicklung von thermischen Spritzprozessen für fortschrittliche Schutz- und Funktionsschichten
G. Mauer (2019), vi, 57 pp
ISBN: 978-3-95806-388-4

Band / Volume 456
Columnar Structured Thermal Barrier Coatings Deposited by Axial Suspension Plasma Spraying
D. Zhou (2019), VI, 126 pp
ISBN: 978-3-95806-391-4

Schriften des Forschungszentrums Jülich
Reihe Energie & Umwelt / Energy & Environment

Band / Volume 457
Modellierung zeitlich aufgelöster Ladeenergienachfragen von batterie-elektrischen Fahrzeugen und deren Abbildung in einem Energiesystemmodell
J. F. Linßen (2019), VIII, 189 pp
ISBN: 978-3-95806-395-2

Band / Volume 458
Synthesis and Analysis of Spinel Cathode Materials for High Voltage Solid-State Lithium Batteries
A. Windmüller (2019), iv, 142 pp
ISBN: 978-3-95806-396-9

Band / Volume 459
Monazite-type ceramics as nuclear waste form: Crystal structure, microstructure and properties
Y. Arinicheva (2019), 194 pp
ISBN: 978-3-95806-397-6

Band / Volume 460
Coupling a Solid Oxide Fuel Cell with a Biomass Gasifier: Degradation Mechanisms and Alternative Anode Materials
H. Jeong (2019), II, 112 pp
ISBN: 978-3-95806-398-3

Band / Volume 461
Model-based Source Partitioning of Eddy Covariance Flux Measurements
A. Klosterhalfen (2019), XVI, 132 pp
ISBN: 978-3-95806-401-0

Band / Volume 462
Entwicklung von großflächigen PECVD-Prozessen zur kontrollierten, homogenen Abscheidung dünner Siliziumschichten für die Photovoltaik
B. O. Grootoonk (2019), 154 pp
ISBN: 978-3-95806-402-7

Band / Volume 463
Simulation of Transport Processes through an Asymmetric Gas Separation Membrane
U. V. Unije (2019), xiv, 101 pp
ISBN: 978-3-95806-403-4

Weitere ***Schriften des Verlags im Forschungszentrum Jülich*** unter
http://wwwzb1.fz-juelich.de/verlagextern1/index.asp

Energie & Umwelt / Energy & Environment
Band / Volume 463
ISBN 978-3-95806-403-4

Mitglied der Helmholtz-Gemeinschaft

JÜLICH
Forschungszentrum